Doctoral theses at NTNU, 2017:329

Yi Liu

Data-driven Borehole Imaging and Monitoring

NTNU
Norwegian University of
Science and Technology

Doctoral thesis

Yi Liu

ISBN 978-82-326-2726-4 (printed ver.)
ISBN 978-82-326-2727-1 (electronic ver.)
ISSN 1503-8181

NTNU
Norwegian University of Science and Technology
Thesis for the Degree of
Philosophiae Doctor
Faculty of Engineering
Department of Geoscience and Petroleum

Doctoral theses at NTNU, 2017:329

NTNU
Norwegian University of
Science and Technology

Yi Liu

Data-driven Borehole Imaging and Monitoring

Thesis for the Degree of Philosophiae Doctor

Trondheim, December 2017

Norwegian University of Science and Technology
Faculty of Engineering
Department of Geoscience and Petroleum

NTNU
Norwegian University of
Science and Technology

NTNU
Norwegian University of Science and Technology

Thesis for the Degree of Philosophiae Doctor

Faculty of Engineering
Department of Geoscience and Petroleum

ISBN 978-82-326-2726-4 (printed ver.)
ISBN 978-82-326-2727-1 (electronic ver.)
ISSN 1503-8181

Doctoral theses at NTNU, 2017:329

Printed by NTNU Grafisk senter

Preface

This thesis is submitted to the Norwegian University of Science and Technology (NTNU) for partial fulfilment of the requirements for the degree of philosophiae doctor.

This doctoral work has been performed at the Department of Geoscience and Petroleum, NTNU, Trondheim, with Professor Børge Arntsen as supervisor.

The research was funded by the DrillWell Centre, a Centre for Research Based Innovation (SFI) from the Research Council of Norway.

Acknowledgements

My first thank goes to my supervisor, Professor Børge Arntsen. He has always been supportive to me, and during the years, I have learnt a lot from him.

I thank the research center DrillWell and its sponsors, the ROSE consortium, and the Department of Geoscience and Petroleum (IGP) at NTNU for the financial support. I also thank Statoil ASA for publication travel grants.

I thank professors Martin Landrø and Alexey Stovas for their support at the department. I am thankful to Professor Kees Wapenaar and his group, including Joost van der Neut, Deyan Draganov, and Jan Thorbecke at Delft University of Technology for having me as a guest PhD student. I enjoyed the hospitality from the fellow students at Delft during the stay.

I thank the administrative staff at IGP for creating a nice working environment. It has been wonderful to know my friends and colleagues, Laleh, Anna, Lars Erik, Tore, Espen, Vegard, Wiktor, Yuriy, Toan, Ivan, Sandra, Lutz, Anders, Alena, Nur, Narjes, Dapeng, Shidong, Qi, Jon Marius, Kjetil, Martin, Lyubov, Sissel, Torbjørn, Kari, Hongyan, Yiqian and many others.

Last but not least, I thank my parents, Xiufen Zou and Jinghua Liu, for their patience and care...

Contents

Preface **i**

Acknowledgements **ii**

Contents **v**

1 Introduction **1**
1.1 Seismic data acquisition 2
1.2 Seismic interferometry and beyond 4
1.2.1 Seismic interferometry 4
1.2.2 The Marchenko method 5
1.3 Motivation 7
1.4 Thesis structure 8
1.5 Contributions 9

2 Retrieving virtual reflection responses at drill-bit positions using seismic interferometry with drill-bit noise **11**
2.1 Introduction 12
2.2 Equations of SI 13
2.2.1 Sources with the same signal 15
2.2.2 Sources with different signals 17
2.3 Numerical drill-bit examples 17
2.3.1 Same source signal 18
2.3.2 Different source signals 22
2.4 Discussion 26
2.5 Conclusion 26
2.6 Acknowledgements 27

3 Combination of surface and borehole seismic data for robust target-oriented imaging **29**
3.1 Introduction 30
3.2 Method 32
3.2.1 Up-down decomposition of the borehole data 33
3.2.2 Imaging from above 35

3.2.3 Imaging from below . . . 37
3.3 Numerical examples . . . 39
3.3.1 Example 1: local imaging below a gas cloud . . . 41
3.3.2 Example 2: a realistic model from the North Sea . . . 49
3.4 Discussion . . . 58
3.5 Conclusions . . . 58
3.6 Acknowledgments . . . 59

4 Up-down wavefield retrieval in boreholes using single-component data 61
4.1 Introduction . . . 62
4.2 Method . . . 63
4.2.1 The up-down wavefield retrieval . . . 63
4.3 Numerical results . . . 68
4.3.1 Horizontal borehole . . . 68
4.3.2 Deviated borehole . . . 72
4.3.3 Vertical borehole . . . 74
4.4 Discussion . . . 74
4.5 Conclusion . . . 76
4.6 Acknowledgements . . . 77

5 A new approach to separate seismic time-lapse time shifts in the reservoir and overburden 79
5.1 Introduction . . . 80
5.2 Method . . . 82
5.2.1 Reconstruction of the reflection responses . . . 82
5.2.2 Time shift estimation . . . 86
5.3 Numerical examples . . . 86
5.3.1 Vankeulen model . . . 86
5.3.2 Gullfaks model . . . 89
5.4 Discussion . . . 103
5.5 Conclusions . . . 104
5.6 Acknowledgements . . . 104

6 Conclusion 105

A The reflection responses 109

B The focusing functions 111
B.1 The mutual relations . . . 111
B.2 The relation with the one-way Green's functions . . . 113
B.2.1 Imaging from above . . . 113
B.2.2 Image from below . . . 115

C The iterative Marchenko scheme 117

D List of publications **119**

References **121**

Chapter 1

Introduction

In petroleum geophysics, a major goal is to obtain an accurate image of the subsurface for geological interpretation, well planning and reservoir management. Different types of geophysical data can be used for this purpose, among which seismic data is the most common. Many techniques and algorithms are developed to turn the recorded data into a depth image. However, a major paradox here is that in order to produce an accurate image, (at least) a kinematically correct velocity model is necessary, but such a model wouldn't be available if one didn't already have some good a priori information of the area (for which the image is intended to be used). Therefore, a lot of effort goes to build such an accurate velocity model. But given the intrinsic problem of velocity uncertainties, a different question is how to maximize the accuracy of an image with the data that are available.

For this, one idea is to place the sources and receivers as close to the target as possible. This is because, in the simplest case of zero-offset recordings (negligible horizontal distance between source and receiver positions), the depth of a reflector in the image is proportional to its signal's traveltime in the data. Then the smaller the traveltime is, the less effect an erroneous velocity will have on the depth image. Given that it is not physically feasible to place the sources and receivers at all image positions in the earth, the question becomes how to virtually place them as close as possible to the imaging target with the available data. In addition, this process should be velocity independent, namely, data-driven, which is to be distinguished from other velocity-dependent seismic redatuming methods.

Then, one way of doing this is by seismic interferometry (SI). It allows one to create virtual sources (or receivers) at the positions of physical receivers (or sources). For example, when there are receivers placed in the borehole, it is possible to turn these receivers into virtual sources for imaging below the borehole, therefore, skipping the effect from (a possible complex) overburden. Another related method is called the Marchenko method, which in a sense is a step beyond SI. Instead of requiring the presence of a physical receiver at the virtual source position, it allows one to create a virtual source at (almost) any chosen location in the subsurface (not at the boundary of sharp interfaces). However,

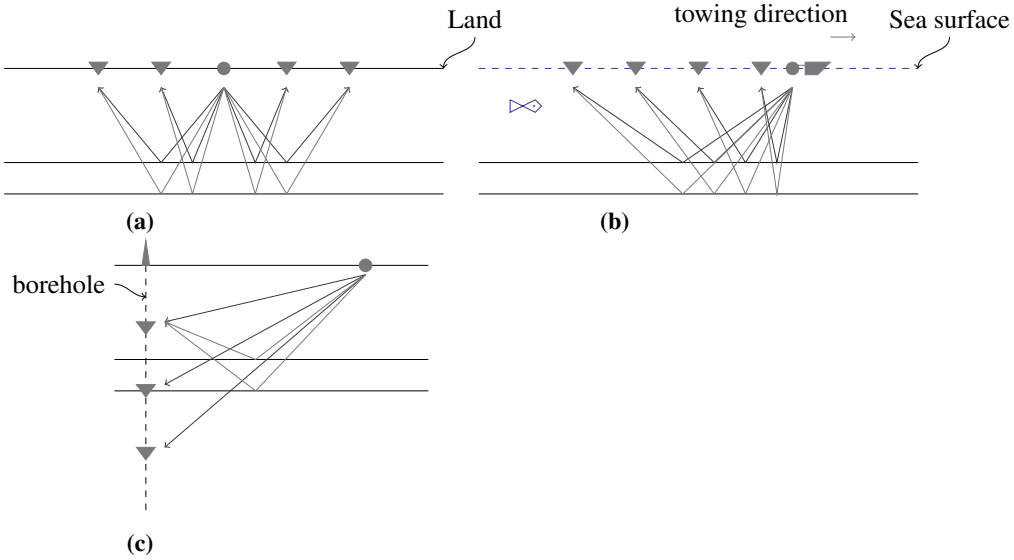

Figure 1.1: Illustration of surface seismic surveys a) on land, b) at sea and c) with receivers in a borehole. The triangles denote receivers and the circles denote sources. The solid lines with arrows indicate possible raypaths.

the requirement is that a macro-velocity model and a good surface reflection response (the clarification for 'good' is postponed for later chapters) are needed. The theme of the thesis is to develop new methods that are completely data-driven for robust imaging and characterisation near boreholes, by using borehole seismic data, together with the commonly available surface reflection data.

For an overview of the method, a brief introduction on seismic data acquisition geometry is necessary. A description of the common types of seismic data will be given in the next section, followed by an illustration of the principles behind SI, the Marchenko method. Then the motivation of the thesis is discussed in detail, and the structure of the thesis is described with a summary of each chapter. This chapter ends with a list of the contributions to each journal article.

1.1 Seismic data acquisition

Seismic data are acquired both on land and at sea. In most surveys, controlled seismic sources are used. On land, such sources are usually explosives and vibroseis (vibrator truck) and geophones are used as receivers. The geophones detect ground movement (velocity); at sea, air guns are typically used as sources, and hydrophones are used as receivers to detect pressure changes in water. For marine surveys, it is also now possible

to measure vertical and horizontal particle velocity by using, for example, dual streamers (Ikelle and Amundsen, 2005). They provide multi-component data that can be used for advanced processing. Fig. 1.1a and 1.1b illustrate the configurations of acquiring seismic data on land and at sea. The sequence of acquiring data is that for land surveys, the receiver positions are laid out beforehand, then typically one source is activated at a time. For marine surveys, the receivers are towed on streamers behind a cluster of airguns, after each source activation, both sources and receivers are towed to a new position until the desired survey area is covered.

After the seismic energy is released from the source, it generates a wavefield that propagates into the subsurface. Part of the wavefield travels directly to the receivers, and this forms the part of the data that is called direct arrivals (or direct waves); part of the energy encounters certain geological interfaces, gets reflected and then travels back to the receivers, and this forms the part of data that most imaging algorithms operate on; part of the energy gets critically refracted and then turns back to the receivers, and this forms part of the data that is called headwaves (or refractions); part of the energy encounters some sharp discontinuities and gets scattered and propagates in all directions, and this forms part of the data that is called diffractions, which is used for diffraction imaging (another subject on its own); the remaining energy turns into mode converted waves (surface waves and P-to-S waves) or eventually dissipates into the earth. After acquiring the data over an interested area, an image can be obtained by using suitable imaging and processing algorithms on the recorded reflection data.

In addition to the surface surveys described above, receivers can also be placed in boreholes, and this results in the so-called vertical seismic profile (VSP) data. The word 'vertical' is because most wells are drilled vertically. Now, deviated and horizontal wells are also common, so these data will be referred as borehole data in this thesis wherever applicable. In the marine environment, the receivers can also be placed on a seabed, and this results in the so-called ocean bottom cable (OBC) data. For these surveys, multi-component data are acquired, with particle velocities measured in three orthonormal directions, in addition to the pressure wavefield. These multi-compoenent data are suitable for more advanced processing, such as up-down wavefield decomposition, deghosting, and estimating the elastic properties of the subsurface, etc. Fig. 1.1c shows an example of the source-receiver geometry of a VSP survey.

Borehole seismic data have been used extensively for reservoir characterisation and field management for many years (Balch et al., 1982; Kennett et al., 1980). In most cases, standard VSP processing methods are used. However, considering the wide availability of surface seismic data, it is worthwhile to consider the combined use of both types of data. By exploiting the redundancy of the traveltimes from both datasets, useful information can be extracted for exploration and monitoring. Several pre-processing schemes and their applications are shown in detail in the later chapters. In short, the basic idea is simply to use the existing information from the data as much as possible. This thesis shows one way of doing that by applying SI and the Marchenko method. The following section explains the concepts of these two methods with simple examples.

1.2 Seismic interferometry and beyond

In this section, an overview of SI and the Marchenko method is given. This is to provide some intuitive understanding. The interested readers can find more details in the following chapters and the appendix.

1.2.1 Seismic interferometry

In general, SI refers to the process of cross-correlating two recordings of ambient seismic noise to obtain a seismogram that would be observed if there were an impulsive point source at one of the recording positions. In exploration, as controlled sources are usually used, an extra summation procedure is needed in order to yield a similar result because one usually only has the sources on one side of the receivers (with a limited aperture), unlike the case with ambient noise.

A typical process for SI by cross-correlation (CC) is the following. First, two recordings (traces) from one source are cross-correlated, then the same procedure is repeated for another source, and so on. After that, all the cross-correlated results are summed together, and the obtained new response can be regarded as what one would record as if there were a source at one of the original two recording positions. In the simplest form, SI by CC is described by the following equation (under certain assumptions, see Wapenaar and Fokkema (2006))

$$\hat{G}(\mathbf{x}_A, \mathbf{x}_B) + \hat{G}^*(\mathbf{x}_A, \mathbf{x}_B) \approx \oint_{\partial D} (\hat{G}^*(\mathbf{x}_A, \mathbf{x}) \hat{G}(\mathbf{x}_B, \mathbf{x})) d\mathbf{x}. \tag{1.1}$$

The Green's function $G(\mathbf{x}_A|\mathbf{x}, t)$ is defined as the causal solution at $\mathbf{x}_A$ to the acoustic wave equation with an impulsive point source of volume injection rate at $\mathbf{x}$. The $\hat{}$ above the quantities denotes the frequency domain, and ∂D denotes the source acquisition surface. This equation is of the simplest form of SI.

As indicated by the closed integral in the equation, for an ideal retrieval of the new response, a sufficient number of surrounding sources are needed, as shown in Fig. 1.2a. But in practice, in the case of receivers in a horizontal borehole, only one-sided source boundary is available, as drawn in Fig. 1.2b. As a result, the direct retrieval of the new response between $\mathbf{x}_A$ and $\mathbf{x}_B$ by this simplest approach would contain artefacts related to the source aperture problem.

However, the degree of the artefacts can be reduced by a number of factors. First, the subsurface is, generally speaking, horizontally layered, and the imaging area is below the receivers, therefore the traveltime information of reflectors underneath the receivers is contained in the path from the receiver positions to the surface sources. In other words, the method recovers the needed reflection traveltime information of horizontal layers, as long as there is an adequate coverage (and density) of sources on the surface. The more slanted the reflectors are, the bigger the source aperture needs to be on the surface. Second, the

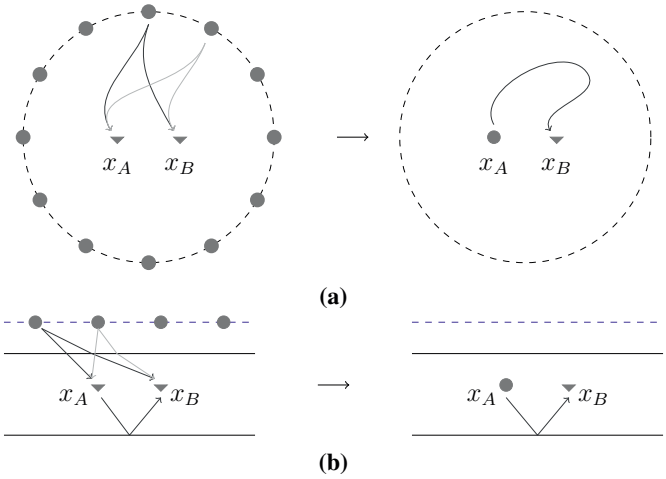

Figure 1.2: Illustration of seismic interferometry

magnitude of multiple reflections. The stronger the multiples are, the more artefacts there will be in the result by the simple cross-correlation method. Some of these artefacts can be reduced by using more sophisticated SI methods, such as SI by multi-dimensional deconvolution (MDD) (van der Neut et al., 2011) with multi-component data, or by the pre-processing schemes which are shown in the chapter 3.

The proposed method combines SI with the Marchenko method to reduce the effect from internal multiples. This is achieved essentially by an iterative use of the surface reflection data, together with the direct traveltime information measured in boreholes. In addition to the common practice of imaging from above, the proposed method also enables one to image from below, meaning to look above from boreholes. Next, a simple example explaining the key element from the Marchenko method, the focusing functions, is given.

1.2.2 The Marchenko method

The Marchenko method is relatively new in the geophysics society, but it is related to the single-sided Marchenko integral equation for 1D inverse scattering problems dated back to Marchenko (1955). It is en exact integral equation that relates the single-sided reflection response to the field inside the medium.

Its recent development in geophysics (Broggini et al., 2012; Wapenaar et al., 2013) is inspired by Rose (2002), where he showed how to focus sound to a point inside a 1D layered medium at a specific time without knowing the velocity profile. One application for the Marchenko method is to image without internal multiples because the Marchenko integral equation fully accounts for all internal multiples. These so-called multiples in the data or image are caused by the multiply reflected energy between the reflectors. They

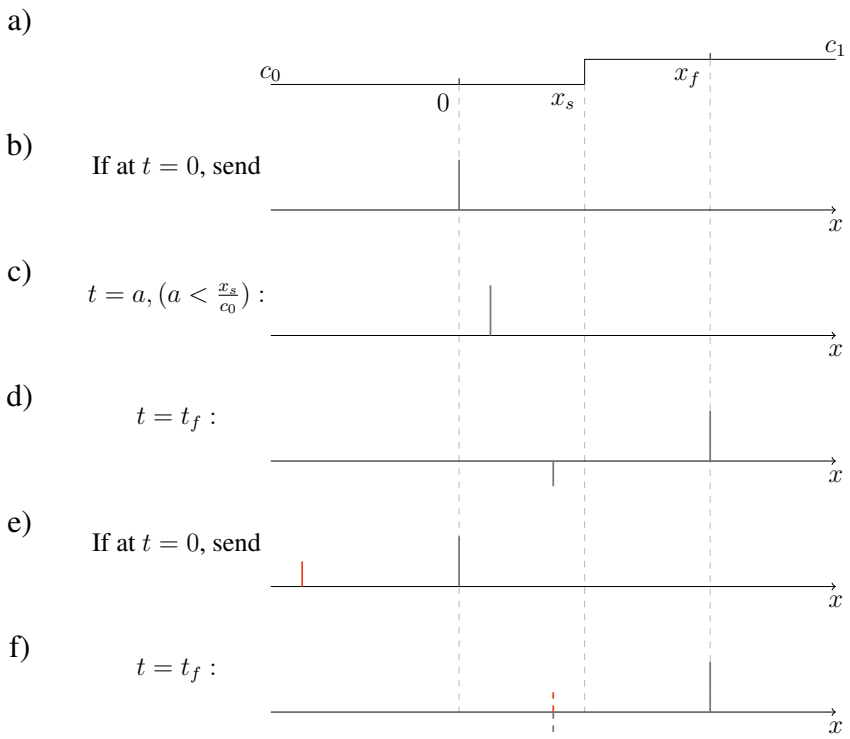

Figure 1.3: Illustration of a simple focusing function

are intrinsic in the acquired data and appear as fake reflectors in images, or obscure the imaging of the actual geological structures. A lot of research efforts have been put into either removing the multiples or utilizing the multiples in imaging (Verschuur et al., 1992; Muijs et al., 2007; Meles et al., 2015).

In the Marchenko method, a central element is called focusing functions. Mathematically speaking, for an acoustic medium, such functions are solutions to the scalar wave equation with specific boundary conditions (see Eq. B.1 - B.4).

For the purpose of an introduction, an intuitive illustration (modified from Rose (2002)) is the following. Suppose there is a 1D velocity profile, where the velocity changes from c_0 to c_1 at $x = x_s$, such as drawn in Fig. 1.3 a). The goal is to design a signal (focusing function) that after being sent from $x = 0$ at $t = 0$ focuses at $x = x_f$. Focusing means that at the time $t = t_f$, only one spike-like signal is observable along the whole 1D line.

If there is no velocity change, the task is trivial, because after sending in a signal, say a spike $\delta(t - x/c_0)$ at $t = 0$, there will be only one spike at a certain position along the line at a given time. In other words, focusing can be achieved at a specific position at any given time, such like $t = a$ in Fig. 1.3 c). But the problem complicates when the medium is not

homogeneous. In this simple example of one-step velocity change, one can already see that sending a single spike-like signal will not result in focusing after the reflection time ($\frac{x_s}{c_0}$), because there will also be a reflected signal travelling along the line in the opposite direction, in addition to the original signal as $t = t_f$ in Fig. 1.3 d). Therefore, a new signal that is capable of cancelling the reflected signal at $t = t_f$ is needed, and it is shown as in Fig. 1.3 e) at $t = 0$. This signal will result in cancelling the reflection at $t = t_f$, resulting in the desired focusing in Fig. 1.3 f). Such a signal is an example of the focusing function. Rose (2002) shows an iterative autofocusing procedure to find the focusing signal in a 1D layered medium with an unknown velocity profile.

The link between the Marchenko equation and SI is discussed in Broggini et al. (2012), where they showed that the Green's function between a given focusing position in a 1D medium and a receiver at the surface can be retrieved by the reflection response measured at the surface using the Marchenko equation. This is different from SI because no physical receiver is needed at desired the focusing position. The general Marchenko equation for a 3D inhomogeneous medium is derived in Wapenaar et al. (2013) and its solution by an iterative scheme is shown.

1.3 Motivation

Given the task of maximizing the accuracy of images near boreholes with unknown medium velocities, new data-driven redatuming schemes to create virtual sources and receivers close to the imaging targets are proposed. The schemes are developed from SI and the Marchenko method. Specifically, the following problems and limitations among the existing imaging and processing methods are taken into consideration,

- **The effect of velocity uncertainty for deep imaging** The benefit of a data-driven redatuming scheme to move the sources and receivers close to the target is multi-folded. First, the redatuming scheme is not velocity dependent, so the uncertainty of the velocity model does not affect the accuracy of the result. This is different from conventional redatuming methods that uses wavefield extrapolation related techniques. Second, as the distance to the imaging target is shortened, the mis-positioning of the reflectors near boreholes due to an erroneous velocity model is reduced. For deep reflectors, such a mispositioning error can be large, significantly degrading the quality of the image. Third, as the sources and receivers are moved into the subsurface, it means that the velocities of the overburden (the medium above the sources and receivers) are no longer needed for imaging the area below. This is an excellent setting for imaging below a complex overburden without any physical sources below the overburden. Numerical examples are shown in Chapter 3 to illustrate this effect.
- **Artefacts and spurious events** Due to the assumptions made in deriving Eq. 1.1 and the practical limitation of one-sided source illumination, the results of conventional SI by cross-correlation contain spurious events, which will appear as artefacts

in the image. These events can be due to many factors. One factor that is related to the one-sided source illumination, and this can be suppressed by combining the traveltime information from both surface reflection data and borehole data, and examples are shown in Chapter 3.

- **Single-component data** As the most common type of data today is still single-component, it is cost effective to use them as much as possible by developing new processing methods. Therefore the use of only single-component data both from the surface and the borehole for up-down wavefield decomposition is studied. Chapter 4 shows the application of the method for boreholes with a general geometry.
- **Image from below** For horizontal boreholes, the conventional imaging is to image the area below boreholes, because of the source locations at the surface. However, it has been shown by Poliannikov et al. (2012) that it is possible to image above by using a different form of SI, called source-receiver interferometry (SRI, Curtis and Halliday (2010)). In this form of SI, two acquisition surfaces are used, instead of one. However, in practice, some spurious events remain in the redatumed results due to the one-sided source coverage and multiple reflections. By using the focusing functions, an improved form of retrieve the reflection response from below is developed and tested with numerical examples in Chapter 3.
- **The utilization of drill-bit noise for imaging** As SI has been applied successfully (Shapiro et al., 2005; Yang et al., 2007; Draganov et al., 2009; Zhan et al., 2010) with passive noise sources, the potential of turning drill-bit noise into virtual receivers for imaging while drilling is studied and demonstrated with a numerical example in Chapter 2.
- **Time-lapse (4D) timeshift estimation near boreholes** After the redatuming, the distance from the virtual source and receiver positions to the reflectors near the borehole are shortened. And in addition, internal multiples are suppressed. Therefore, the method shows great potential for 4D traveltime analysis. First, the time shifts in the overburden and the underburden can be separated. Second, the enhanced signal-to-noise ratio because of the removal of multiples makes it easier to identify certain events 4D analysis. Chapter 5 presents two numerical examples from field velocity models in the North Sea and the comparison with field data results.

1.4 Thesis structure

This thesis consists of six chapters in total. The main part of the thesis comprises four papers that stand as different chapters.

The use of SI for turning drill-bit noise into virtual receivers is discussed in Chapter. 2. In this paper, the requirement of applying an inter-source type of SI using non-transient noise sources, such as drill-bit noise is investigated. Synthetic drilling noise is used in

the example, and it is observed that for the successful retrieval of the reflection responses between the drill-bit positions, a good estimate of the drill-bit signal itself is needed. Part of the work is presented at the 77th European Association of Geoscientists and Engineers (EAGE) Conference and Exhibition 2015 and the Rock Seismic (ROSE) meeting in 2015. The journal paper is published in *Geophysical Prospecting* in 2016.

Chapter. 3 introduces a series of redatuming schemes for robust imaging above and below horizontal boreholes, using a combination of surface and borehole seismic data. In the suggested schemes, the multiples and the one-sided distribution of sources are taken into account. By finding the focusing function using the surface reflection data and the direct arrival's travel time from borehole data, the spurious events due to internal multiples are removed, resulting in a clearer image around the borehole. Erroneous velocities are also tested on the retrieved data, and a better positioning of the deep reflectors is observed with the redatumed data, as compared to the original data. Part of the work is presented at the 84th Society of Exploration Geophysicists (SEG) Annual Meeting in 2015 and the Rock Seismic (ROSE) meeting in 2016. The journal paper is published in *Geophysical Journal International* in 2016.

Chapter. 4 focuses on the aspect that the up-down wavefields at the borehole depth can be retrieved with only single-component surface and borehole data. Comparisons are made between these retrievaled wavefields and those from multi-component data for three different borehole geometries (horizontal, deviated, and vertical) . Part of the work is presented at the 78th European Association of Geoscientists and Engineers (EAGE) Conference and Exhibition in 2016. The journal paper is submitted to *Journal of Applied Geophysics* in 2017.

Chapter. 5 shows the use of the redatuming schemes developed in Chapter. 3 for 4D seismic time shift analysis. It shows that the pre-processing schemes effectively separate the time shifts in the overburden and the reservoir, leading to a more direct and clearer time shift estimation, as compared to the original surface and borehole data. Two numerical examples using field velocity models are shown and comparisons are made with the time shift results from the field data. Part of the work is presented at the 85th Society of Exploration Geophysicists (SEG) Annual Meeting in 2016. The journal paper is published in *Geophysics* in 2017.

1.5 Contributions

The contributors to the papers in the thesis are as follows:

- **Paper 1, Chapter 2** Retrieving virtual reflection responses at drill-bit positions using seismic interferometry with drill-bit noise. *Geophysical Prospecting, vol. 64, 348–360.*
  This work was performed by Yi Liu as the lead author and researcher. Deyan Draganov, Kees Wapenaar and Børge Arntsen participated as advisers.

- **Paper 2, Chapter 3** Combination of surface and borehole seismic data for robust target-oriented imaging. *Geophysical Journal International, vol. 205, 758-775.*
  This work was performed by Yi Liu as the lead author and researcher. Joost van der Neut, Børge Arntsen and Kees Wapenaar participated as advisers.
- **Paper 3, Chapter 4** Up-down wavefield retrieval in boreholes using single-component data. *Submitted to Journal of Applied Geophysics*
  This work was performed by Yi Liu as the lead author and researcher. Børge Arntsen, Joost van der Neut and Kees Wapenaar participated as advisers.
- **Paper 4, Chapter 5** A new approach to separate seismic time-lapse time shifts in the reservoir and overburden. *Geophysics, vol. 82.(6): Q67-Q78.*
  This work was performed by Yi Liu as the lead author and researcher. Martin Landrø, Børge Arntsen, Joost van der Neut and Kees Wapenaar participated as advisers.

Chapter 2

Retrieving virtual reflection responses at drill-bit positions using seismic interferometry with drill-bit noise

Yi Liu[1], Deyan Draganov[2], Kees Wapenaar[2], and Børge Arntsen[1]

[1]Norwegian University of Science and Technology
[2]Delft University of Technology

Published in *Geophysical Prospecting*, 64 (2): 348-360

Abstract

In the field of seismic interferometry, researchers have retrieved surface waves and body waves by crosscorrelating recordings of uncorrelated noise sources to extract useful subsurface information. The retrieved wavefields in most applications are between receivers. When the positions of the noise sources are known, inter-source interferometry can be applied to retrieve the wavefileds between sources, thus turning sources into virtual receivers. Previous applications of this form of interferometry assume impulsive point sources or transient sources with similar signatures. We investigate the requirements of applying inter-source seismic interferometry using non-transient noise sources with known positions to retrieve reflection responses at those positions and show the results using synthetic drilling noise as source. We show that if pilot signals (estimates of the drill-bit signals) are not available, it is required that the drill-bit signals are the same and that the phases of the virtual reflections at drill-bit positions can be retrieved by deconvolution interferometry or by crosscoherence interferometry. Further for this case, classic interferometry by crosscorrelation can be used if the source power spectrum can be esti-

mated. If pilot signals are available, virtual reflection responses can be obtained by first using standard seismic-while-drill processing techniques, such as pilot crosscorrelation and pilot deconvolution to remove the drill-bit signatures in the data, and then applying crosscorrelation interferometry. Therefore, provided that pilot signals are reliable, drill-bit data can be redatumed from surface to borehole depths using this inter-source interferometry approach without any velocity information of the medium, and we show that a well-positioned image below the borehole can be obtained using interferometrically redatumed reflection responses with just a simple velocity model. We discuss some of the practical hurdles that restrict the application of the proposed method offshore.

2.1 Introduction

The crosscorrelation of two recordings of seismic noise leads to an estimate of the Green's function between these two positions, as if one of them were an impulsive source. This method has been successfully applied in seismology to retrieve surface waves using coda waves (Campillo and Paul, 2003; Snieder, 2004) or ambient-noise recordings (Shapiro and Campillo, 2004; Sabra et al., 2005a), and useful subsurface information has been derived from the retrieved surface waves by seismic tomography (Shapiro et al., 2005; Sabra et al., 2005b; Yang et al., 2007). In general, the method of retrieving the Green's function by crosscorrelation is called seismic interferometry (SI). The derivations of such retrieval using diffuse wavefields are shown in Lobkis and Weaver (2001) and Snieder (2004), and for non-diffuse wavefields in any inhomogeneous medium by Wapenaar (2004) and Wapenaar and Fokkema (2006).

Besides surface waves, body waves can also be retrieved by ambient-noise SI, although not that easily mostly because of its stronger amplitude decay with distance. In regional seismology, examples of retrieving body waves are shown by Roux et al. (2005) and Gerstoft et al. (2006) for diving P-waves, by Zhan et al. (2010) for Moho-reflected S-waves and by Ruigrok et al. (2011) for Moho-reflected P-waves.

In exploration seismics, body-wave reflections (above 1 Hz) are usually required for structural imaging. At frequencies above 1 Hz in ambient-noise recordings, the surface waves should be suppressed in order to retrieve the body waves. Night-hour ambient-noise recordings (Draganov et al., 2007), patterns of geophones (Draganov et al., 2009), and selected parts of the noise (Panea et al., 2014) are utilized for such suppression in order to retrieve reflections using ambient noise. Draganov et al. (2013) and Xu et al. (2012) show examples of extracting exploration-scale velocities and structures from ambient-noise recordings. Crosscoherence is another approach to apply SI using noise sources and Nakata et al. (2011) retrieve both surface waves and body waves from traffic noise by crosscoherence SI.

Besides passive noise, active noise with known locations, such as drill-bit noise, has long been used in seismic-while-driling (SWD) to obtain reverse vertical seismic profiles (RVSP) (Rector and Marion, 1991; Poletto and Miranda, 2004) and to provide look-ahead

information while drilling (Malusa et al., 2002; Eidsvik and Hokstad, 2006). Most methods in SWD rely on pilot signals (estimates of the seismic signature of the drill-bit) to compress the drill-bit signal to an impluse (Rector and Marion, 1991; Poletto et al., 2000, 2004, 2014). The standard SWD processing involves crosscorrelation of pilot signals and geophone recordings, reference deconvolution and pilot-delay shift. An alternative method to process SWD data that does not require pilot signals is shown by Miller et al. (1990) and Haldorsen et al. (1995) using multi-channel deconvolution. To apply SI to drill-bit data, Vasconcelos and Snieder (2008b) use deconvolution SI and show both numerical and field examples of using the retrieved reflections for imaging. In their method, pilot signals are not required because the source signature is cancelled by spectral division during deconvolution. Poletto et al. (2010) compare the method of drill-bit SI with and without pilot signals and showed field-data results from crosscorrelation and deconvolution SI.

All these applications of SI using noise sources retrieve the estimated Green's function between receivers. Inter-source interferometry is derived by source-receiver reciprocity (Curtis et al., 2009), and retrieves the estimated Green's function between sources. This form of SI can be useful for noise sources with known locations. Curtis et al. (2009) and Tonegawa and Nishida (2010) show examples of creating virtual seismometers from different types of earthquakes, assuming the source time functions of the earthquakes are similar.

To investigate the application of inter-source interferometry to non-transient noise sources with and without similar signals, we use synthetic drill-bit data from drilling noise in a horizontal well to retrieve virtual reflection responses at drill-bit positions. Practicalities of drill-string multiples and pilot delay shift are not included. We first look at the basic equations of inter-source interferometry by crosscorrelation, deconvolution and crosscoherence, and then show the results from each approach. A migration image below the well using the retrieved reflection responses is compared with a surface-seismic image to show the potential advantage of using inter-source SI with drill-bit data.

2.2 Equations of SI

It is known from SI that new seismic responses between two locations can be retrieved by crosscorrelating the observed wavefields at these locations and summing over surrounding sources. The summation is implicit when recordings from ambient noise are used because the recorded wavefield is already a superposition of simultaneously acting noise sources. Supposing a response from each individual impulsive point source is measured separately and using acoustic Green's function representations, SI by crosscorrelation can be represented in the frequency domain (Wapenaar and Fokkema, 2006) as

$$G(\mathbf{x}_A|\mathbf{x}_B) + G^*(\mathbf{x}_A|\mathbf{x}_B) \propto \oint_{\partial D} G^*(\mathbf{x}_A|\mathbf{x}) G(\mathbf{x}_B|\mathbf{x}) d\mathbf{x}. \tag{2.1}$$

Here, the Green's function $G(\mathbf{x}_A|\mathbf{x}_B)$ represents the acoustic wavefield observed at $\mathbf{x}_A$ due to an impulsive point source at $\mathbf{x}_B$. Using the Cartesian coordinate vector, spatial location is denoted by $\mathbf{x} = (x, y, z)$ with z pointing downward, representing depth. Uppercase symbols represent quantities in the frequency domain. The superscript * denotes complex conjugate. So in the time domain, the left-hand side of Eq. 2.1 represents the superposition of the causal and anti-causal response observed at $\mathbf{x}_A$ due to an impulsive point source at $\mathbf{x}_B$, and it is proportional to a surface integral of crosscorrelations of the Green's functions observed at $\mathbf{x}_A$ and $\mathbf{x}_B$, due to sources at all $\mathbf{x}$ at a boundary ∂D. Equation (2.1) is a high-frequency approximation; it is further assumed that the medium at and outside ∂D is homogeneous and that all rays leaving the source boundary are approximately normal to ∂D (Wapenaar and Fokkema, 2006).

Inter-source interferometry can be formed by source-receiver reciprocity (Curtis et al., 2009). By using $G^*(\mathbf{x}_A|\mathbf{x}) = G^*(\mathbf{x}|\mathbf{x}_A)$ and $G(\mathbf{x}_B|\mathbf{x}) = G(\mathbf{x}|\mathbf{x}_B)$, the right-hand side of Eq. 2.1 turns into

$$G(\mathbf{x}_A|\mathbf{x}_B) + G^*(\mathbf{x}_A|\mathbf{x}_B) \propto \oint_{\partial D} G^*(\mathbf{x}|\mathbf{x}_A) G(\mathbf{x}|\mathbf{x}_B) d\mathbf{x}. \tag{2.2}$$

It can be interpreted from this equation that instead of the Green's function between two receivers, the crosscorrelation of the response at $\mathbf{x}$ due to the impulsive point sources at $\mathbf{x}_A$ and at $\mathbf{x}_B$, and the subsequent summation of the correlated responses over all receiver positions, retrieves the estimated Green's function between two sources.

In reality, an impulsive point source is replaced by a source with a time function $s(t)$, which can be either transient or non-transient (e.g. noise). Because in this paper we consider drill-bit data, we will assume from here onward that $s(t)$ is a random non-transient signal. We write the observed response at $\mathbf{x}$ due to the source at $\mathbf{x}_i$ (i can be A or B) as

$$Y(\mathbf{x}|\mathbf{x}_i) = G(\mathbf{x}|\mathbf{x}_i) S(\mathbf{x}_i), \tag{2.3}$$

where $S(\mathbf{x}_i)$ is the source function at $\mathbf{x}_i$ in the frequency domain (i.e., the source spectrum). Further, we define C_{AB} as

$$C_{AB}(\mathbf{x}) = Y^*(\mathbf{x}|\mathbf{x}_A) Y(\mathbf{x}|\mathbf{x}_B). \tag{2.4}$$

Then, for an acquisition geometry with sources in the subsurface and receivers at the surface ∂D_0, the summation of C_{AB} over all available receiver positions on ∂D_0 reads

$$\int_{\partial D_0} C_{AB}(\mathbf{x}) d\mathbf{x} = S^*(\mathbf{x}_A) S(\mathbf{x}_B) \int_{\partial D_0} G^*(\mathbf{x}|\mathbf{x}_A) G(\mathbf{x}|\mathbf{x}_B) d\mathbf{x}. \tag{2.5}$$

Constructive contribution to the retrieved Green's function comes from stationary-phase positions (Snieder et al., 2006). For retrieving the reflections from below the subsurface sources, the stationary points lie along the surface where we can have our measurements. Spurious events may occur due to finite aperture available on the surface ∂D_0, but also due to the one-sided illumination of having receivers only at the surface and also due to intrinsic losses in the medium. Overall, given a wide coverage on the surface ∂D_0 and compared with Eq. 2.2, Eq. 2.5 becomes

$$\int_{\partial D_0} C_{AB}(\mathbf{x}) d\mathbf{x} \propto S^*(\mathbf{x}_A) S(\mathbf{x}_B)(G(\mathbf{x}_A|\mathbf{x}_B) + G^*(\mathbf{x}_A|\mathbf{x}_B)), \tag{2.6}$$

where $G(\mathbf{x}_A|\mathbf{x}_B)$ mainly contains reflections from one side of the sources because of the one-sided summation along ∂D_0 (Reflections from the other side of the sources would result in non-physical arrivals, because ∂D_0 is not a closed boundary (Snieder et al., 2006)). Now we have $S^*(\mathbf{x}_A)S(\mathbf{x}_B)$ on the right-hand side and when $S(\mathbf{x}_A) \neq S(\mathbf{x}_B)$, $S^*(\mathbf{x}_A)S(\mathbf{x}_B)$ has a random phase and therefore changes the phase of the retrieved Green's function on the right-hand side. This does not happen for inter-receiver SI, because the left-hand side of Eq. 2.1 is always the crosscorrelation of the responses from the same source. This can be understood more intuitively from Fig. 2.1, where the direct-wave travel path is rotated to show that complex conjugation is taken. In panel a), the recorded wavefields represented by the ray paths with opposite arrows are crosscorrelated and the traveltime on the common path can be found and subtracted, because they are from the same physical source. However, this is not the case for inter-source SI shown in Fig. 2.1 b), because the ray path with opposite arrows originate from different sources, and when the random source signals are different, crosscorrelation does not find the common travelpath, except when $\mathbf{x}_A = \mathbf{x}_B$, namely the zero-offset virtual traces [1].

2.2.1 Sources with the same signal

If we consider the special case of both sources with the same signature, e.g. $S(\mathbf{x}_A) = S(\mathbf{x}_B) = S$, Eq. 2.6 becomes

$$\int_{\partial D_0} C_{AB}(\mathbf{x}) d\mathbf{x} \propto |S|^2 (G(\mathbf{x}_A|\mathbf{x}_B) + G^*(\mathbf{x}_A|\mathbf{x}_B)). \tag{2.7}$$

The right-hand side yields, in the time domain, the Green's function between two sources $\mathbf{x}_A$ and $\mathbf{x}_B$ convolved with the autocorrelation of the source signal. If the autocorrelation does not resemble the Dirac delta function $\delta(t)$, the amplitude information in the Green's

[1] One of the reviewers pointed us to the patent: Mateeva, A., Mehta, K., and Tatanova, M., 2011, âĂIJLook Ahead Seismic While DrillingâĂİ, international publication No. WO 2011/159803 A2, in which a zero-offset version of the method is presented.

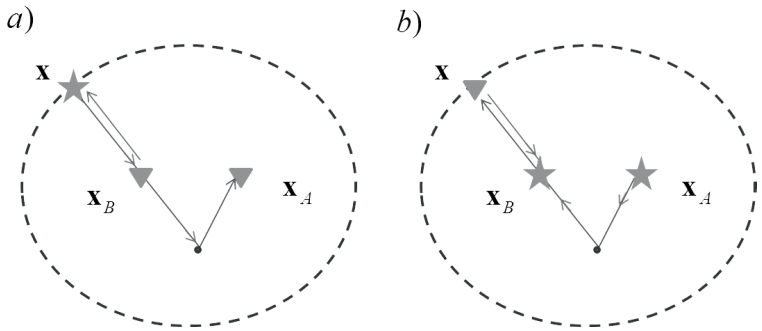

Figure 2.1: Illustration of seismic interferometry of a) inter-receiver form and b) inter-source form. Triangle denotes receiver and star denotes source. Dashed line indicates the integral surface. The direct-wave travel path is rotated to show that complex conjugation is taken.

function will be distorted, but this problem could be alleviated by deconvolving the power spectrum $|S|^2$ from C_{AB} if such information is available.

If $|S|^2$ is unknown, deconvolution SI (Vasconcelos and Snieder, 2008a) or crosscoherence SI (Nakata et al., 2011) can be used and they are defined in the frequency domain as

$$D_{AB}(\mathbf{x}) = \frac{Y(\mathbf{x}|\mathbf{x}_B)}{Y(\mathbf{x}|\mathbf{x}_A)} = \frac{Y^*(\mathbf{x}|\mathbf{x}_A)Y(\mathbf{x}|\mathbf{x}_B)}{|Y(\mathbf{x}|\mathbf{x}_A)|^2} = \frac{G^*(\mathbf{x}|\mathbf{x}_A)G(\mathbf{x}|\mathbf{x}_B)}{|G(\mathbf{x}|\mathbf{x}_A)|^2} \tag{2.8}$$

and

$$H_{AB}(\mathbf{x}) = \frac{Y^*(\mathbf{x}|\mathbf{x}_A)Y(\mathbf{x}|\mathbf{x}_B)}{|Y(\mathbf{x}|\mathbf{x}_A)||Y(\mathbf{x}|\mathbf{x}_B)|} = \frac{G^*(\mathbf{x}|\mathbf{x}_A)G(\mathbf{x}|\mathbf{x}_B)}{|G(\mathbf{x}|\mathbf{x}_A)||G(\mathbf{x}|\mathbf{x}_B)|}, \tag{2.9}$$

respectively. The source signature is cancelled by the spectral division in both equations. Although the amplitude information is discarded, the phase information is kept in both approaches, which is acceptable for structural imaging or tomography. Both D_{AB} and H_{AB} equal to 1 when $\mathbf{x}_A = \mathbf{x}_B$, which results in the Dirac delta function in time at zero-offset. This means that the retrieved responses by both approaches satisfy the so called *clamped boundary condition* (Vasconcelos and Snieder, 2008a). It can also be recognized from Eq. 2.8 that for deconvolution SI, the denominator changes when we interchange $\mathbf{x}_A$ and $\mathbf{x}_B$, while for crosscoherence SI, and the denominator does not change. Therefore, crosscoherence removes the effect from amplitude variations and gives a more balanced result. In addition, crosscoherence is also more numerically stable because when the denominator is small, the numerator is also small. Nakata et al. (2011) provides a detailed analysis of the properties of crosscoherence SI. Next, integrating both sides of Eq. 2.8 and 2.9 along ∂D_0 reads

$$\int_{\partial D_0} D_{AB}(\mathbf{x}) d\mathbf{x} = \int_{\partial D_0} \frac{G^*(\mathbf{x}|\mathbf{x}_A)G(\mathbf{x}|\mathbf{x}_B)}{|G(\mathbf{x}|\mathbf{x}_A)|^2} d\mathbf{x} \tag{2.10}$$

and

$$\int_{\partial D_0} H_{AB}(\mathbf{x})d\mathbf{x} = \int_{\partial D_0} \frac{G^*(\mathbf{x}|\mathbf{x}_A)G(\mathbf{x}|\mathbf{x}_B)}{|G(\mathbf{x}|\mathbf{x}_A)||G(\mathbf{x}|\mathbf{x}_B)|}d\mathbf{x}. \tag{2.11}$$

Comparing with Eq. 2.2, it shows that the phase of the Green's function between sources can be estimated without knowing the individual source signals.

2.2.2 Sources with different signals

For sources with different signals, it requires the estimates of the source signals to be known in order to apply inter-source interferometry. For drill-bit SI, it means applying standard seismic-while-drilling processing (Rector and Hardage, 1992; Poletto et al., 2004) using pilot signals before applying SI. We briefly describe such drill-bit signal deconvolution as

$$\widetilde{G}(\mathbf{x}|\mathbf{x}_A) = \frac{Y(\mathbf{x}|\mathbf{x}_A)\widetilde{S}^*(\mathbf{x}_A)}{|\widetilde{S}(\mathbf{x}_A)|^2}. \tag{2.12}$$

Here, $\widetilde{S}(\mathbf{x}_A)$ is the pilot signal of the drill-bit at $\mathbf{x}_A$ and $\widetilde{G}(\mathbf{x}|\mathbf{x}_A)$ represents the estimated impulse response from the drill-bit to the receiver. Related technique and discussion on drill-bit data processing can be found in Poletto et al. (2004). Then one can use the classic crosscorrelation approach shown in Eq. 2.2 to estimate the Green's function between sources.

As briefly mentioned earlier, the zero-offset virtual traces can still be recovered when the source signals are different and no pilot signal is measured. However, in this zero-offset case, when SI by autocorrelation is to be used, it follows from Eq. 2.6 that the right-hand side still contains $|S|^2$. This means that the virtual zero-offset response, even though zero-phased, is still blurred by the autocorrelation of the drill-bit signal. This is equivalent to the inter-receiver type SI by crosscorrelation using noise source signal, which is not necessarily white by itself. In practical applications, this would mean that the correlation of the drill-bit noise will not be a delta function and the zero-offset reflection response would suffer from a virtual-source wavelet with a long duration. In contrast, when pilot signals are measured, the approach described by Eqs. 2.2 and 2.12 leads to a virtual - source response with a short-duration wavelet.

2.3 Numerical drill-bit examples

Based on the analysis from the previous section, we assume two situations: one in which we use the drill-bit with the same signal (just for illustration) and one with different signals in acoustic medium. The 2D P-wave velocity model is shown in Fig. 2.2. We place 121

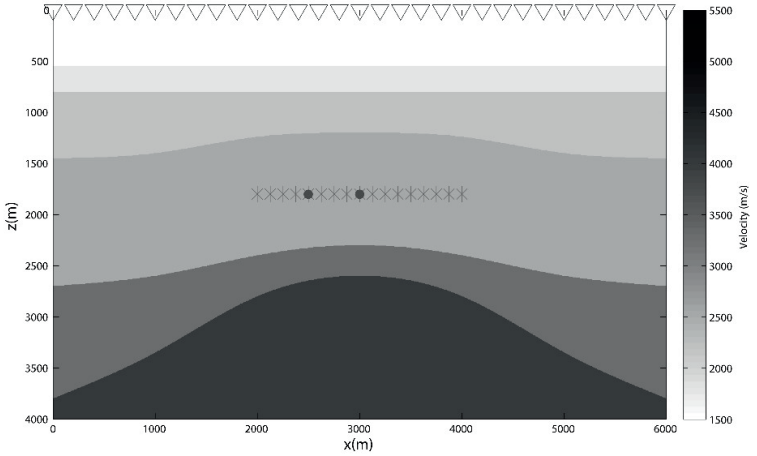

Figure 2.2: The P-wave velocity model. Triangle denotes receiver and star denotes drill-bit source position. The two solid circles indicate the reference positions. Every fifth source and receiver are plotted.

receivers (denoted by triangles) at the surface with a spacing of 50 meters. The first receiver is at $x = 0$ m and the last receiver is at $x = 6000$ m. The drill-bit is in a horizontal well at the depth $z = 1800$ m, and we model 81 common-source gathers at the drill-bit positions (denoted by stars) from $x = 2000$ m to $x = 4000$ m with a spacing of 25 meters.

2.3.1 Same source signal

Although in practice a drill-bit emits signals that are different from each other, we include this special case of them having the same signal for any general non-transient noise and to demonstrate that deconvolution or crosscoherence interferometry can be used to retrieve inter-source reflections in this case. These two approaches do not rely on the assumption that the autocorrelation of noise signal is spike-like.

The modelled drill-bit source function and its power spectrum is shown in Fig. 2.3 c) and d), respectively. The modelled drilling noise is 3 seconds long and we convolve the drill-bit signal with the sources modelled using a Ricker wavelet by an acoustic finite-difference method (Thorbecke and Draganov, 2011). Fig. 2.3 a) and b) shows the acoustic responses received at the surface from the drill-bit position at $x = 2500$ m and $x = 3000$ m (denoted by two solid circles in Fig. 2.2), respectively. Because the power spectrum of the drill-bit source function is not white, crosscorrelation interferometry is not that suitable without knowing the source power spectrum itself. So assuming no information about the source signal is available, we use deconvolution (Eq. 2.8) and crosscoherence (Eq. 2.9) and sum the results over all receiver positions (Eq. 2.10 and 2.11). Then we

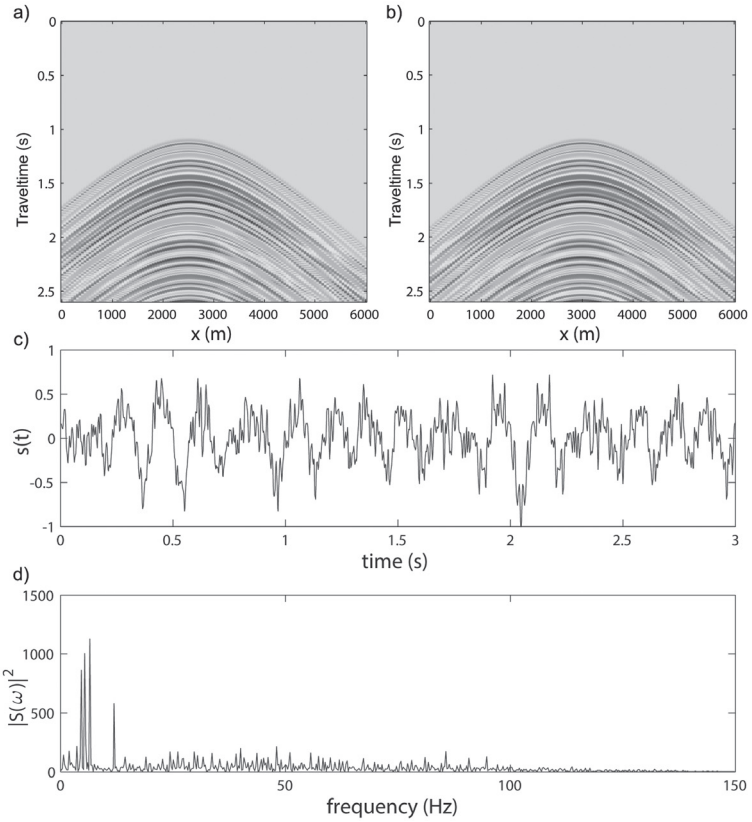

Figure 2.3: Drill-bit source function and recorded common-source gathers. a) Common-source gather at $x = 2500$ m and b) at $x = 3000$ m. c) Modelled drill-bit source function. d) Power spectrum of the modelled drill-bit function. The drill-bit source function is modelled as a three-cone roller bit with each cone composed of three teeth rows (Poletto et al., 2004), the weight on bit of 130 kN, 60 bit revolutions per minute and a normalized speed amplitude of 0.3 (Aarrestad and Kyllingstad, 1988). $s(t)$ and $|S(\omega)|^2$ denotes the source time function and its power spectrum, respectively.

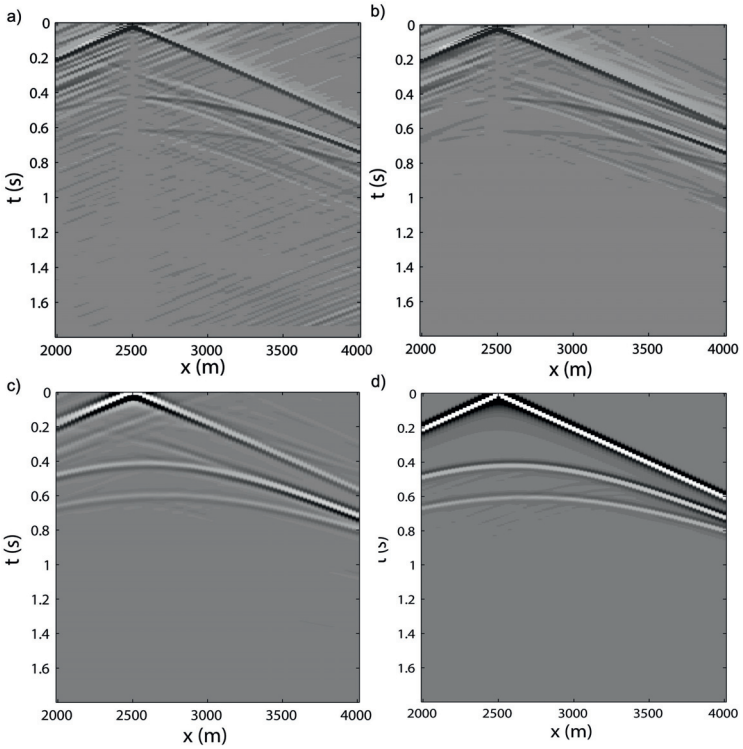

Figure 2.4: Comparison of the retrieved responses with the reference response. The virtual response of the source at $x = 2500$ m retrieved by a) deconvolution, b) crosscoherence and c) crosscorrelation. d) The reference response modelled with a homogeneous overburden. Both a) and b) do not require any knowledge of the source function $s(t)$, except that $s(t)$ does not change with changing drill-bit positions, while c) requires the power spectrum $|S(\omega)|^2$ to be known.

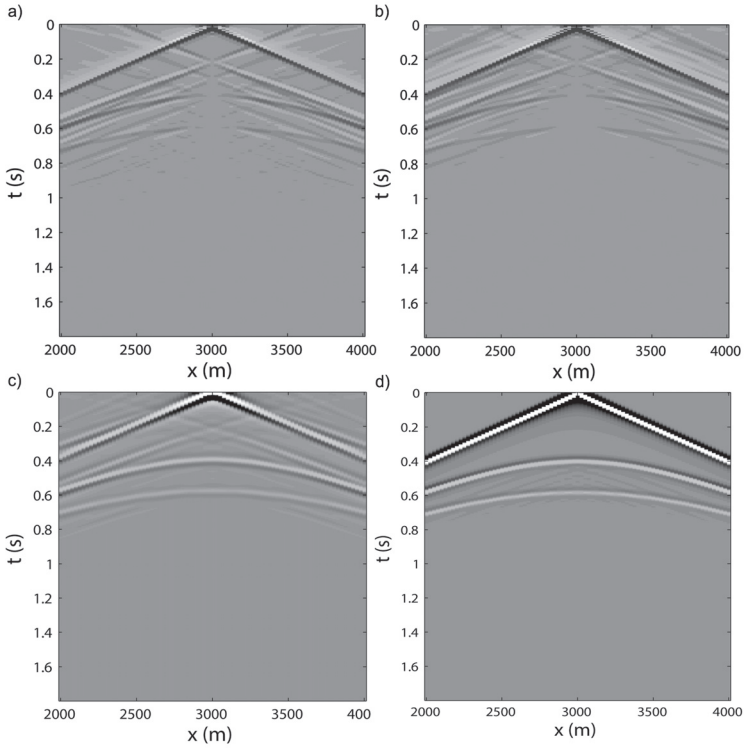

Figure 2.5: As Figure 4, but for the source at $x = 3000$ m.

apply a lowpass filter up to 40 Hz and assign a Ricker wavelet to the results. Fig. 2.4 a) and b) show the retrieved responses with the position of the reference source at $x = 2500$ m by deconvolution and crosscoherence, respectively. The retrieved responses correspond to an acquisition geometry with both borehole sources and receivers. Next, assuming the source power spectrum can be estimated, we use crosscorrelation SI and divide the power spectrum on both sides of Eq. 2.7 and the result is shown in Fig. 2.4 c). Fig. 2.4 d) shows the reference response directly modelled with a homogeneous overburden. Fig. 2.5 shows the counterpart of Fig. 2.4 but with a reference source position at $x = 3000$ m. The *clamped boundary condition* can be observed in both Fig. 2.4 a), b) and Fig. 2.5 a), b) as the wavefield vanishes at zero-offset except at time zero. And as discussed before, the retrieved response by crosscoherence in Fig. 2.4 b) and Fig. 2.5 b) also appear more balanced and stable compared to the response by deconvolution in Fig. 2.4 a) and Fig. 2.5 a).

2.3.2 Different source signals

In reality, the drill-bit signal varies at different positions, so for this example we modelled 81 different drill-bit signals at each source position indicated in Fig. 2.2. Fig. 2.6 a) shows the modelled drill-bit source function $s(t)$ at $x = 3000$ m and panel b) shows the pilot signal $\tilde{s}(t)$ with about 5% noise (due to the machinery, electricity, etc.). The noise $\tilde{s}(t) - s(t)$ is shown in panel c). Then we deconvolve the recorded surface drill-bit data using both the exact source signal $s(t)$ and the pilot signal $\tilde{s}(t)$, respectively. Fig. 2.7 a) shows a raw common-source gather at $x = 3000$ m, and panels b) and c) show the pilot-deconvolved common-source gathers using $s(t)$ and $\tilde{s}(t)$, respectively. The retrieved responses using inter-source crosscorrelation interferometry (Eq. 2.2) are shown in Fig. 2.8. Energy normalization is applied after the interferometry process for panel b) and d), which use the noise-contaminated pilot signal $\tilde{s}(t)$. No energy normalization is applied for panel a) and c), which use the exact source signal $s(t)$.

Using the above procedure, we retrieve common-source gathers for a source at each drill-bit position and virtual receivers at all other drill-bit positions. Then we migrate the retrieved responses from the $\tilde{s}(t)$ pilot-deconvolved data using one-way prestack depth migration (Thorbecke et al., 2004) with a simple homogeneous velocity of 2750 m/s (2500 m/s+10% error). The result is shown in Fig. 2.9 a). Note that the velocity in the layer where the drill-bit positions are situated is 2500 m/s and the velocities of the layers below it are 3300 m/s and 4000 m/s. Fig. 2.9 b) shows a conventional image of the sub-surface reflectors obtained from the surface seismic reflection data using the 10-percent erroneous migration velocity. We can see that the deep reflectors are mispositioned more severely in Fig. 2.9 b) than in Fig. 2.9 a).

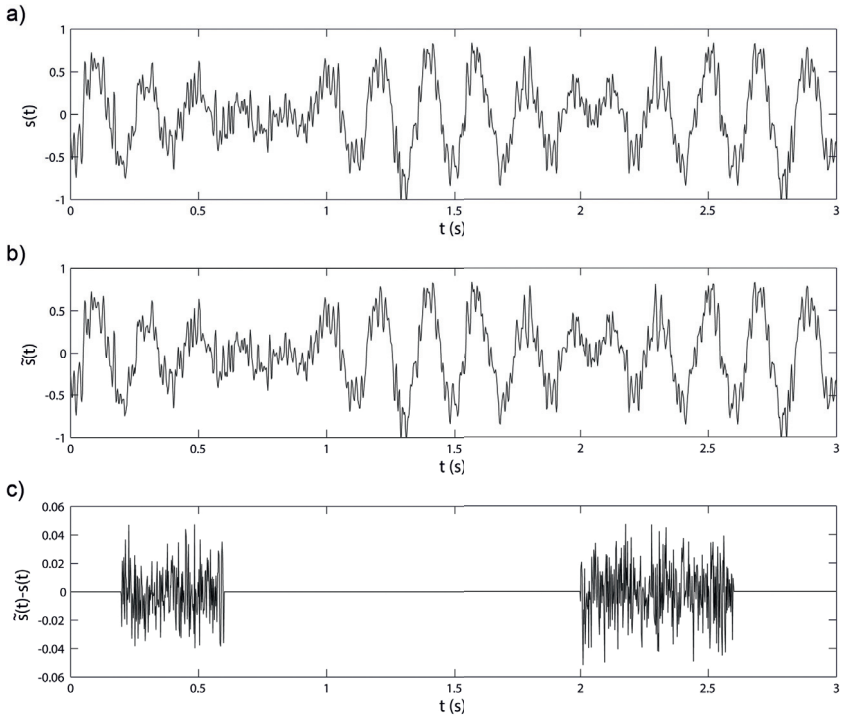

Figure 2.6: Modelled drill-bit signal. a) The exact drill-bit source function $s(t)$. b) Estimate of the signal $\tilde{s}(t)$. c) The noise added to the estimated signal, which is up to 5% of the drill-bit signal.

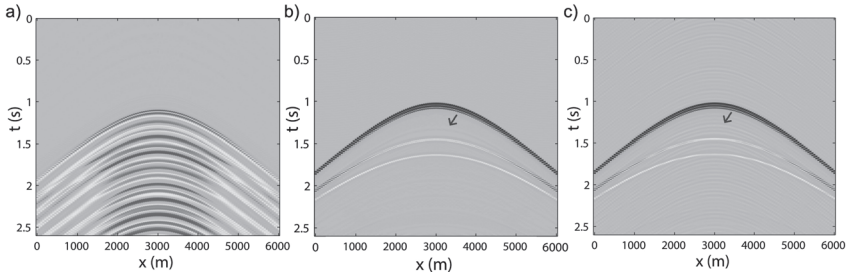

Figure 2.7: Modelled common-source gather and pilot-deconvolved results. a) Raw common-source gather from drilling noise at $x = 3000$ m. Pilot-deconvolved common-source gathers using b) the exact source signal $s(t)$ and c) the noise-contaminated pilot signal $\tilde{s}(t)$. The arrow indicates the internal multiple from the second layer, which arrives about 0.2 seconds after the direct waves.

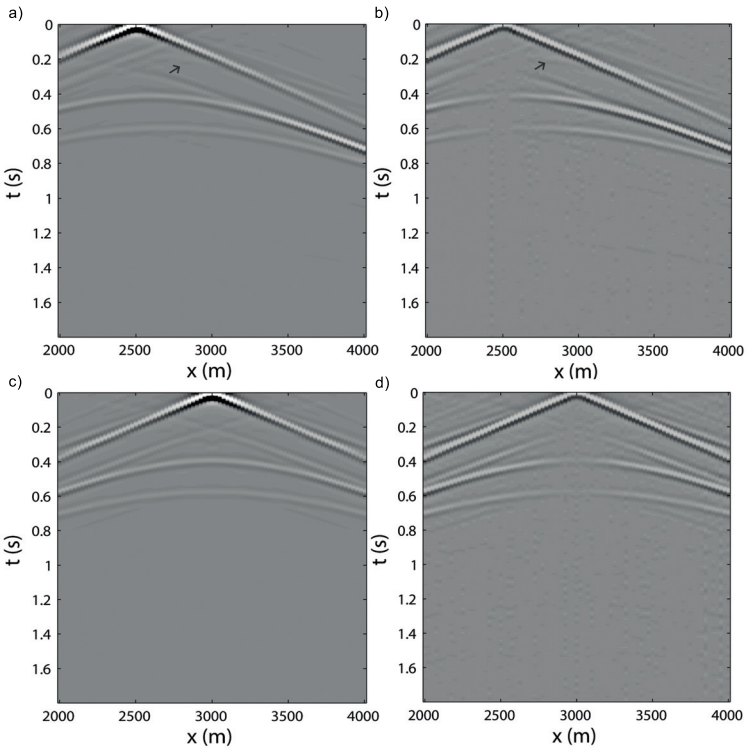

Figure 2.8: Retrieved common-source response at the drill-bit positions. The top row corresponds to the virtual drill-bit receiver data from a virtual source at $x = 2500$ m and the bottom row from a virtual source at $x = 3000$ m. a) and c) are retrieved after using the exact drill-bit source function $s(t)$ for pilot deconvolution, and b) and d) after using $\tilde{s}(t)$ for pilot deconvolution and applying energy normalization to the retrieved response. The arrow indicates the non-physical reflection identified as the crosscorrelation of the direct waves and the internal multiples.

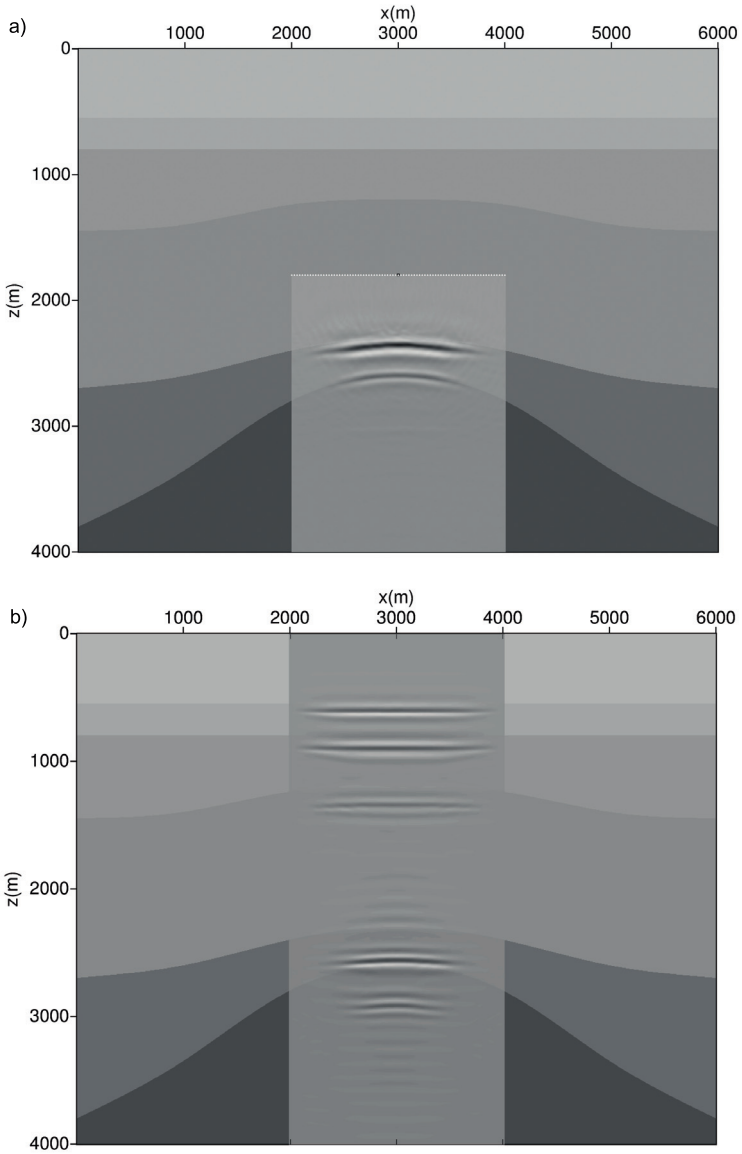

Figure 2.9: Migration images a) using retrieved virtual reflection responses at the drill-bit positions, and b) using conventional surface seismic reflection data. The background indicates the true velocity model. Image a) is obtained using a homogeneous velocity model of 2750 m/s (2500 m/s+10% error), while image b) is obtained using the 10-percent erroneous velocities of the whole model.

Because we use the total wavefields in the interferometry process and we only have one-sided illumination with a finite number of receivers at the surface, non-physical reflection appear in all retrieved responses. In Fig. 2.8, non-physical reflections (indicated by the arrows) appear before the first primary reflection. This is due to the crosscorrelation of the upgoing direct field with the upgoing internal multiple from the second layer (indicated by the arrow in Fig. 2.7). In the conventional redatuming to a horizontal well, in which receivers are used, often only the direct arrival is used for correlation (e.g. Bakulin and Calvert (2006)). This eliminates the retrieval of some possible non-physical reflections. Mehta et al. (2007) show that using wavefield separation and correlating the direct arrival in the downgoing wavefield with the upgoing arrivals further improves the retrieved results, as some more non-physical reflections are not retrieved. Further, tapering the traces that are recorded at positions far from the stationary-phase positions would reduce some of the artefacts in the retrieved response, which appear as straight lines extending out from the retrieved first primary reflections in Fig. 2.8.

2.4 Discussion

From the above results, it is clear that the information about the drill-bit noise is essential. In practical applications, the useful signal from the pilot at the drill-bit should have sufficient signal-to-noise ratio. When the level of the interfering noise (e.g. from the noise inside the borehole) is too high, the method might not work.

The method we propose will work best with receivers that can be left in the field for the time of the drilling. This means that its natural area of application would be with receiver arrays on land or with ocean-bottom stations or cables. In all three cases, the receiver spacing should not allow aliasing of the recorded wavefields.

Note that the length of the receiver array (extent of the network) would dictate the positions of the drill-bit between which a reflection response can be retrieved. The two drill-bit positions and the receiver geometry must be such that the receivers cover the stationary-phase region for retrieval of reflections between the two drill-bit positions.

2.5 Conclusion

We applied inter-source seismic interferometry to numerically simulated drill-bit signal. Contrary to Green's function retrieval between receivers using mutually uncorrelated non-transient sources with unknown signals, a successful application of inter-source seismic interferometry requires the non-transient sources to have the same signal. We show that if this condition is met, deconvolution or crosscoherence interferometry can be used to extract useful phase information of the Green's function between source positions, without knowing the source signal itself. In reality, it can be expected that most non-transient sources with known positions, such as drill-bit noise, emit different signals with changing

positions. This creates a major problem for applying inter-source SI to non-transient noise sources without knowing their signal (except for the zero-offset response). However, as pilot signals are usually acquired to recover the impulse response of the drill-bit, pilot-deconvolved drill-bit data can be utilized with inter-source crosscorrelation interferometry to retrieve virtual reflection responses at drill-bit positions. The retrieved responses are useful for imaging as they have been interferometrically redatumed to the borehole level, thus independent of the velocity accuracy of the overburden. We recommend that pilot signals be measured downhole near the drill-bit to get good results after pilot deconvolution, because there is additional noise due to drill-string reflections, rig activities and signal attenuation.

2.6 Acknowledgements

The authors acknowledge the Research Council of Norway, ConocoPhillips, Det norske oljeselskap, Statoil and Wintershall for financing the work through the research centre DrillWell - Drilling and Well Centre for Improved Recovery, a research cooperation between IRIS, NTNU, SINTEF and UiS; and the ROSE consortium at NTNU. The research of D.D is supported by the Division for Earth and Life Sciences (ALW) with financial aid from the Netherlands Organization for Scientific Research (NWO) with VIDI grant 864.11.009. We also thank Joost van der Neut (TUDelft) and the reviewers for their suggestions that helped to improve the manuscript.

Chapter 3

Combination of surface and borehole seismic data for robust target-oriented imaging

Yi Liu[1], Joost van der Neut[2], Børge Arntsen[1], Kees Wapenaar[2]

[1]Norwegian University of Science and Technology
[2]Delft University of Technology

Published in *Geophysical Journal International*, 205 (2): 758-775

Abstract

A novel application of seismic interferometry (SI) and Marchenko imaging using both surface and borehole data is presented. A series of redatuming schemes is proposed to combine both datasets for robust deep local imaging in the presence of velocity uncertainties. The redatuming schemes create a virtual acquisition geometry where both sources and receivers lie at the horizontal borehole level, thus only a local velocity model near the borehole is needed for imaging, and erroneous velocities in the shallow area have no effect on imaging around the borehole level. By joining the advantages of SI and Marchenko imaging, a macro-velocity model is no longer required and the proposed schemes use only single-component data. Furthermore, the schemes result in a set of virtual data that have fewer spurious events and internal multiples than previous virtual source redatuming methods. Two numerical examples are shown to illustrate the workflow and to demonstrate the benefits of the method. One is a synthetic model and the other is a realistic model of a field in the North Sea. In both tests, improved local images near the boreholes are obtained using the redatumed data without accurate velocities, because the redatumed

data are close to the target.

3.1 Introduction

Conventional subsurface imaging usually uses active surface seismic data (with sources and receivers at the surface), or various types of VSP data (Vertical Seismic Profile, with either sources or receivers in the subsurface). An image of the subsurface is obtained by applying a depth migration algorithm together with a suitable velocity model. Due to the acquisition geometry, the reflected waves pass through various depths in the earth to the surface. Hence, a velocity model that covers the whole depth section is needed for depth migration. The accuracy of the velocity model has a big impact on the imaging result, especially for deep areas. In practice, one usually only has limited knowledge of the subsurface, and obtaining a good velocity model of the whole area is often a difficult task itself.

On the other hand, seismic interferometry (SI, also called Green's function retrieval) is a data-driven technique that can transform the original data into a sort of virtual data, where physical receivers are turned into virtual sources (Bakulin and Calvert, 2006) or vice versa (Curtis et al., 2009; Liu et al., 2016a). This makes it an alternative processing technique for certain types of VSP data (Schuster, 2009) to image targeted areas that are difficult to image with the original acquisition geometries. Another advantage of SI is that it is completely data-driven, which is different from other redatuming techniques that rely on prior velocity information of the medium to extrapolate the wavefield downward.

The basic idea of SI is that by crosscorrelating two seismic traces from an active source and sum the result over all sources, we can construct the seismogram that would be recorded at one of the trace's recording positions as if there were a source at the other. It is first described by Claerbout (1968) for horizontally layered media, and is later rediscovered independently by helioseismologists (Duvall et al., 1993). Schuster et al. (2004) generalize Claerbout's daylight imaging concept to the theory of interferometric seismic imaging and show that it can also be used to migrate multiples in CDP (Common Depth Point) data. The exact form of SI by crosscorrelation (CC) is derived by Wapenaar (2004) for any inhomogeneous lossless medium using reciprocity theorems. Willis et al. (2006) show an example of imaging steep salt flanks by creating virtual sources from walk-away VSP data; Bakulin and Calvert (2006) apply SI to image through complex overburdens and develop its field application for sensitive reservoir monitoring. Other approaches to SI have also been proposed. Vasconcelos and Snieder (2008a,b) propose SI by deconvolution and show examples of creating virtual downhole receivers from drill-bit data to image the San Andreas fault. Wapenaar and van der Neut (2010) present SI by multidimensional deconvolution (MDD), which is valid for media with loss and they show that SI by MDD can compensate for one-sided illumination and irregularity of the sources (e.g. variations in their power spectra and unevenly distributed source locations). Minato et al. (2011) reconstruct crosswell reflection wavefields without borehole sources using SI by

MDD with singular value decomposition. However, SI by MDD requires wavefield decomposition, which means multi-component data is necessary, because the up-and downgoing wavefields can be obtained by weighted summation and subtraction of geophone and hydropphone recordings (Amundsen, 1993; Amundsen and Reitan, 1995). In general, without proper wavefield decomposition, the retrieved responses by SI in practice contain artefacts due to one-sided illumination and limited aperture (Snieder et al., 2006) at the summation surface. Comprehensive and systematic comparisons between these different approaches to SI can be found in Snieder et al. (2009), Wapenaar et al. (2011), and Galetti and Curtis (2012).

As an extension to the classic seismic interferometry, Curtis et al. (2006) and Curtis and Halliday (2010) proposed source-receiver wavefield interferometry (SRI) . It retrieves the Green's function from the observations on two closed boundaries, instead of one. Because time-reversal is involved, it holds again only in lossless media. Poliannikov (2011) shows an application using a form of SRI. In his example, the retrieved responses are the downgoing reflections coming from the reflectors above the downhole receivers, so it can be viewed as a way of imaging from below. For practical acquisition geometries with limited apertures and one-sided illumination, the retrieved responses by SRI also contain spurious events. Another approach of imaging from below is shown by van der Neut and Wapenaar (2015), where they use SI by crosscorrelation of decomposed wavefields, but this still can result in spurious events due to one-sided illumination.

Taking a step beyond SI, another redatuming technique that is generally referred to as the Marchenko method (also called Marchenko focusing) (Broggini et al., 2012; Wapenaar et al., 2013, 2014; Behura et al., 2014) no longer requires the physical presence of a receiver at the position of the virtual source. This implies that one can generate virtual data with any chosen point in the subsurface as a source. However, the method is not completely data-driven, as it requires an estimate of the traveltimes from the virtual source positions to the surface. This means that a macro-velocity model that describes the kinematics of the wavefield is necessary. Various potential applications for Marchenko imaging are suggested by Wapenaar et al. (2014). Meles et al. (2015) show how to predict and remove internal multiples using the Marchenko scheme and SI. Ravasi et al. (2016) present a marine data example using a Marchenko scheme.

In this paper, we propose a series of new redatuming schemes that use both surface and borehole seismic data for robust imaging near the borehole. It means that velocity errors, either in the shallow part or near the borehole, will not drastically affect the imaging, as they would for the original data. The virtual data have both sources and receivers at the borehole locations, and then two separate images are calculated - one below the borehole and one above the borehole. By using the direct arrivals from borehole data, this approach joins the benefits of SI and Marchenko imaging. The proposed schemes are completely velocity independent, and need only single-component data for the up-down decomposition. Furthermore, because of the up-down decomposition, the redatumed data contain fewer spurious events than previous data-driven redatuming methods that also use only single-component data.

In the next section, we first explain how to use the surface reflection response to construct the up- and downgoing wavefields at the borehole level. In essence, this is done by finding the focusing functions defined in the Marchenko method, but using the traveltimes measured in the borehole data. Then we construct various redatuming schemes for local imaging from above and from below, respectively. In total, there are four schemes for imaging from above, and two for imaging from below. In the example section, these schemes are tested on two synthetic acoustic datasets, one from a relatively simple synthetic model with a gas cloud in the overburden and the other from a realistic model of a field in the North Sea. The local images are compared with standard images from surface data using both the correct and erroneous velocity models. We then discuss the results, outline directions for further study, and summarize.

3.2 Method

The notation convention used in this paper is similar to what is used in the paper on Marchenko imaging by Wapenaar et al. (2014). This makes it easy for the readers to find the detailed derivations of the related equations in the Marchenko method. A spatial position is denoted by $\mathbf{x} = (x_1, x_2, x_3)$, with $x_3 = 0$ on the surface level ∂D_0 and x_3 increasing positively downward. Coordinates at any boundary, e.g. at the depth level ∂D_i (which indicates the horizontal borehole depth level in this paper), are denoted as $\mathbf{x}_i = (\mathbf{x}_H, x_{3,i})$, with $\mathbf{x}_H = (x_1, x_2)$. Position $\mathbf{x}_i^{'}$ represents a focusing position at lateral coordinate $\mathbf{x}_H^{'}$ at the depth level ∂D_i, and $\mathbf{x}_0^{''}$ represents a position at lateral coordinate $\mathbf{x}_H^{''}$ at the surface level ∂D_0. Quantities in the frequency domain are indicated with the $\hat{}$ above (omitting the variable ω for angular frequency).

We consider only acoustic media, and free surface multiples are not included (the half-space above the acquisition surface is considered homogeneous). To take the free surface into account, Singh et al. (2015) describe Marchenko imaging with the free surface included; for this reason, it is possible to extend the schemes presented here to include free-surface multiples. Throughout this paper, we denote by "Green's function" the response of an impulsive point source in the actual medium, not in a background medium. When referring to the recorded wavefields in the data, we assume that source deconvolution has been applied, so we can treat the data as measured band-limited Green's functions.

In order not to be confused with Marchenko imaging (which retrieves the reflection response at each depth level of interest and then applies the imaging condition to obtain the image), it is worth to clarify that we aim to retrieve the reflection response only at the borehole depth. Then a conventional depth migration algorithm is applied to obtain a local images above and below the borehole, respectively. To retrieve the reflection response (the redatuming process) for imaging, the focusing functions defined in the Marchenko method is essential for constructing the up-downgoing components in the single-component borehole data. The focusing functions themselves are found by using the direct wavefield and its traveltime from the borehole data, together with the surface reflection response

from the surface data. In this way, the proposed redatuming schemes become completely independent of any velocity estimates of the medium.

Now, we start with more details on the up-down decomposition of single-component borehole data using surface reflection data.

3.2.1 Up-down decomposition of the borehole data

In the Marchenko method, it is shown that the one-way Green's functions is found to be related to the focusing functions via the following relations. For $t \geq t_d(\mathbf{x}_i^{'}|\mathbf{x}_0^{''})$, where $t_d(\mathbf{x}_i^{'}|\mathbf{x}_0^{''})$ is the direct arrival time from $\mathbf{x}_0^{''}$ to $\mathbf{x}_i^{'}$,

$$G^{-}(\mathbf{x}_i^{'}|\mathbf{x}_0^{''},t) = \int_{\partial D_0}\int_{-\infty}^{t} \mathcal{R}^{\cup}(\mathbf{x}_0^{''}|\mathbf{x}_0,t-t^{'})f_1^{+}(\mathbf{x}_0|\mathbf{x}_i^{'},t^{'})dt^{'}d\mathbf{x}_0; \tag{3.1}$$

$$G^{+}(\mathbf{x}_i^{'}|\mathbf{x}_0^{''},t) = -\int_{\partial D_0}\int_{-\infty}^{t} \mathcal{R}^{\cup}(\mathbf{x}_0^{''}|\mathbf{x}_0,t-t^{'})f_1^{-}(\mathbf{x}_0|\mathbf{x}_i^{'},-t^{'})dt^{'}d\mathbf{x}_0 + f_{1,0}^{+}(\mathbf{x}_0^{''}|\mathbf{x}_i^{'},-t). \tag{3.2}$$

Here, $G^{-}(\mathbf{x}_i^{'}|\mathbf{x}_0^{''},t)$ and $G^{+}(\mathbf{x}_i^{'}|\mathbf{x}_0^{''},t)$ are viewed as the up- and downgoing components of the borehole data received at the horizontal depth level ∂D_i; $\mathcal{R}^{\cup}(\mathbf{x}_0^{''}|\mathbf{x}_0,t)$ is the surface reflection response from the surface data ($^{\cup}$ denotes that this is the reflection response from above, where the downgoing free-surface related multiples are removed.). The first coordinate vector stands for the receiver position and the second for the position of the source. $f_1^{+}(\mathbf{x}_0|\mathbf{x}_i^{'},t)$ and $f_1^{-}(\mathbf{x}_0|\mathbf{x}_i^{'},t)$ are the down- and upgoing components of the focusing function $f_1(\mathbf{x}_0|\mathbf{x}_i^{'},t)$. For the focusing functions the first coordinate vector stands again for the receiver position, but the second coordinate vector stands for the focal point. The subscript $_0$ indicates the initial estimate, which we will explain shortly. There are two focusing functions, $f_1(\mathbf{x}|\mathbf{x}_i^{'},t)$ and $f_2(\mathbf{x}|\mathbf{x}_0^{''},t)$, and they are a key element in the Machenko method, but in order to focus on the main idea of this subsection, we will postpone the details of the focusing functions for now. The above equations say that the up- and downgoing components of the borehole data can be calculated, given the focusing functions, the surface reflection response, and the traveltime $t_d(\mathbf{x}_i^{'}|\mathbf{x}_0^{''})$. Since $t_d(\mathbf{x}_i^{'}|\mathbf{x}_0^{''})$ can be found from the direct arrival's traveltime in the borehole data and we also have the surface reflection response, then the problem becomes to find the focusing functions.

In the Marchenko method, the focusing functions are found by iteratively solving the following equations for $t < t_d(\mathbf{x}_i^{'}|\mathbf{x}_0^{''})$,

$$f_1^{-}(\mathbf{x}_0^{''}|\mathbf{x}_i^{'},t) = \int_{\partial D_0}\int_{-\infty}^{t} \mathcal{R}^{\cup}(\mathbf{x}_0^{''}|\mathbf{x}_0,t-t^{'})f_1^{+}(\mathbf{x}_0|\mathbf{x}_i^{'},t^{'})dt^{'}d\mathbf{x}_0; \tag{3.3}$$

$$f_1^+(\mathbf{x}_0^{''}|\mathbf{x}_i^{'},-t)=\int_{\partial D_0}\int_{-\infty}^{t}\mathcal{R}^{\cup}(\mathbf{x}_0^{''}|\mathbf{x}_0,t-t^{'})f_1^-(\mathbf{x}_0|\mathbf{x}_i^{'},-t^{'})dt^{'}d\mathbf{x}_0. \tag{3.4}$$

The iterative Marchenko scheme requires an initial estimate to the solution. This estimate is generally obtained by time-reversing the direct wavefield, represented by $G_d(\mathbf{x}_i^{'}|\mathbf{x}_0^{''},-t)$, which is typically obtained from a smooth macro-velocity model that describes the kinematics of the direct wavefield in Marchenko method. But in our case with given borehole data, this means that we can directly use the direct arrivals to define $G_d(\mathbf{x}_i^{'}|\mathbf{x}_0^{''},-t)$, and this naturally makes the iterative scheme completely independent of any velocity estimates. This initial estimate of the focusing function can be written as

$$f_{1,0}^+(\mathbf{x}_0^{''}|\mathbf{x}_i^{'},t)=f_{2,0}^-(\mathbf{x}_i^{'}|\mathbf{x}_0^{''},t)=G_d(\mathbf{x}_i^{'}|\mathbf{x}_0^{''},-t). \tag{3.5}$$

We can now just replace the initial estimate of $f_1^+(\mathbf{x}_0^{''}|\mathbf{x}_i^{'},-t)$ on the right-hand side of eq. 3.6 with $G_d(\mathbf{x}_i^{'}|\mathbf{x}_0^{''},t)$, so it becomes

$$G^+(\mathbf{x}_i^{'}|\mathbf{x}_0^{''},t)=-\int_{\partial D_0}\int_{-\infty}^{t}\mathcal{R}^{\cup}(\mathbf{x}_0^{''}|\mathbf{x}_0,t-t^{'})f_1^-(\mathbf{x}_0|\mathbf{x}_i^{'},-t^{'})dt^{'}d\mathbf{x}_0+G_d(\mathbf{x}_i^{'}|\mathbf{x}_0^{''},t). \tag{3.6}$$

After the focusing functions are found by the iterative Marchenko scheme using the directly measured borehole data, eq. 3.1 and 3.6 are used to construct the up- and downgoing components in the borehole data.

Finally, we include more details of the focusing functions. In this paper, they are both defined as a superposition of pressure-normalized downgoing ($^+$) and upgoing ($^-$) components, such as

$$f_1(\mathbf{x}|\mathbf{x}_i^{'},t)=f_1^+(\mathbf{x}|\mathbf{x}_i^{'},t)+f_1^-(\mathbf{x}|\mathbf{x}_i^{'},t) \tag{3.7}$$

and

$$f_2(\mathbf{x}|\mathbf{x}_0^{''},t)=f_2^+(\mathbf{x}|\mathbf{x}_0^{''},t)+f_2^-(\mathbf{x}|\mathbf{x}_0^{''},t). \tag{3.8}$$

These focusing functions are solutions to the wave equation in a truncated medium with specific boundary conditions. The truncated medium is identical to the actual medium above ∂D_i, but it is reflection-free below ∂D_i. The focusing conditions read formally as

$$\partial_3 f_1^+(\mathbf{x}|\mathbf{x}_i^{'},t)|_{x_3=x_{3,i}}=-\frac{1}{2}\rho(\mathbf{x}_i^{'})\delta(\mathbf{x}_H-\mathbf{x}_H^{'},t)\frac{\partial\delta(t)}{\partial t} \tag{3.9}$$

and

$$\partial_3 f_2^-(\mathbf{x}|\mathbf{x}_0^{''},t)|_{x_3=x_{3,0}}=\frac{1}{2}\rho(\mathbf{x}_0^{''})\delta(\mathbf{x}_H-\mathbf{x}_H^{''},t)\frac{\partial\delta(t)}{\partial t}. \tag{3.10}$$

The difference between the two focusing functions is that $f_1(\mathbf{x}|\mathbf{x}_i^{'},t)$ focuses at $\mathbf{x}_i^{'}$ in the

subsurface and $f_2(\mathbf{x}|\mathbf{x}_0^{''},t)$ focuses at $\mathbf{x}_0^{''}$ at the surface. The two focusing functions are mutually related via

$$f_1^+(\mathbf{x}_0^{''}|\mathbf{x}_i^{'},t) = f_2^-(\mathbf{x}_i^{'}|\mathbf{x}_0^{''},t); \tag{3.11}$$

and

$$-f_1^-(\mathbf{x}_0^{''}|\mathbf{x}_i^{'},-t) = f_2^+(\mathbf{x}_i^{'}|\mathbf{x}_0^{''},t). \tag{3.12}$$

3.2.2 Imaging from above

Assuming a horizontal borehole, we define the idea of imaging from above as to retrieve the reflection response from above (of the medium below the borehole), as if the medium above the borehole is reflection-free. Then a conventional depth migration algorithm is applied to the retrieved reflection response using only a local velocity model to produce an image below the borehole. In other words, we aim to use the original borehole dataset (sources at the surface and receivers in the borehole) and the surface dataset (source and receiver at the surface) to create a virtual dataset with both sources and receivers in the borehole, above which the medium is reflection-free.

It has been shown that such virtual reflection response $\mathcal{R}^{\cup}(\mathbf{x}_i^{'}|\mathbf{x}_i,t)$ is related to the up-downgoing wavefields via (Amundsen, 2001; Wapenaar et al., 2011)

$$G^-(\mathbf{x}_i^{'}|\mathbf{x}_0^{''},t) = \int_{\partial D_i}\int_{-\infty}^{+\infty} \mathcal{R}^{\cup}(\mathbf{x}_i^{'}|\mathbf{x}_i,t^{'})G^+(\mathbf{x}_i|\mathbf{x}_0^{''},t-t^{'})dt^{'}d\mathbf{x}_i, \tag{3.13}$$

so $\mathcal{R}^{\cup}(\mathbf{x}_i^{'}|\mathbf{x}_i,t)$ can be solved if the up-down wavefields are known. This typically requires multi-component data for the up-down decomposition (Amundsen and Reitan, 1995). For single-component data, an alternative is to approximate the downgoing $G^+(\mathbf{x}_i|\mathbf{x}_0^{''},t)$ with the direct arrivals in the borehole data and use the remaining data for the upgoing $G^-(\mathbf{x}_i|\mathbf{x}_0^{''},t)$ (van der Neut et al., 2015a), such as

$$G^+(\mathbf{x}_i|\mathbf{x}_0^{''},t) \approx G_d(\mathbf{x}_i|\mathbf{x}_0^{''},t), \tag{3.14}$$

and

$$G^-(\mathbf{x}_i^{'}|\mathbf{x}_0^{''},t) \approx G(\mathbf{x}_i^{'}|\mathbf{x}_0^{''},t) - G_d(\mathbf{x}_i^{'}|\mathbf{x}_0^{''},t), \tag{3.15}$$

so eq. 3.13 becomes

$$G(\mathbf{x}_i^{'}|\mathbf{x}_0^{''},t) - G_d(\mathbf{x}_i^{'}|\mathbf{x}_0^{''},t) \approx \int_{\partial D_i}\int_{-\infty}^{+\infty} \mathcal{R}^{\cup}(\mathbf{x}_i^{'}|\mathbf{x}_i,t^{'})G_d(\mathbf{x}_i|\mathbf{x}_0^{''},t-t^{'})dt^{'}d\mathbf{x}_i. \tag{3.16}$$

This scheme only uses borehole data. The retrieved response $\mathcal{R}^{\cup}(\mathbf{x}_i^{'}|\mathbf{x}_i,t)$ contains spurious events related to the approximations made in eq. 3.14 and 3.15. But when the multiple reflections in the subsurface are not strong, the up-down wavefield approximation in

eq. 3.14 and 3.15 is sufficient for retrieving the reflection response from above to image close to the borehole. We will later see an example of this in the numerical section.

Next, we show the schemes that use both surface and borehole data. As shown in the previous subsection, namely that the up- and downgoing components in the borehole data can be computed once the focusing functions are found, we can rewrite the exact scheme in eq. 3.13 as

$$\Psi\left[\int_{\partial D_0}\hat{\mathcal{R}}^{\cup}(\mathbf{x}_0^{''}|\mathbf{x}_0)\hat{f_1^{+}}(\mathbf{x}_0|\mathbf{x}_i^{'})d\mathbf{x}_0\right] = \int_{\partial D_i}\hat{\mathcal{R}}^{\cup}(\mathbf{x}_i^{'}|\mathbf{x}_i)\left\{\Psi\left[-\int_{\partial D_0}\hat{\mathcal{R}}^{\cup}(\mathbf{x}_0^{''}|\mathbf{x}_0^{'''})\hat{f}_1^{-*}(\mathbf{x}_0^{'''}|\mathbf{x}_i)d\mathbf{x}_0^{'''}\right]+\hat{G}_d(\mathbf{x}_i|\mathbf{x}_0^{''})\right\}d\mathbf{x}_i, \tag{3.17}$$

by using eq. 3.1 and 3.6. Here, to make the equation relatively short and easier to interpret, we decide to switch to the frequency domain (indicated by the $\hat{}$ above the quantities) and introduce an operator Ψ. The operator Ψ first inverse Fourier transforms the data, then applies a time window which passes data only for $t \geq t_d(\mathbf{x}_i^{'}|\mathbf{x}_0^{''})$, and then Fourier transforms the result back to the frequency domain. In this equation, $\hat{\mathcal{R}}^{\cup}(\mathbf{x}_i^{'}|\mathbf{x}_i)$ is the unknown, $\hat{f_1^{+}}(\mathbf{x}_0|\mathbf{x}_i^{'})$ is found by iteratively solving eq. 3.3 and 3.4 using the direct wavefield in the borehole data as the initial solution as explained in the previous subsection. $\hat{\mathcal{R}}^{\cup}(\mathbf{x}_0^{''}|\mathbf{x}_0)$ is the surface reflection data, and $\hat{G}_d(\mathbf{x}_i|\mathbf{x}_0^{''})$ is the direct arrivals from the borehole data. The equation is then solved per frequency, using a least squares approach, for example. The retrieved $\mathcal{R}^{\cup}(\mathbf{x}_i^{'}|\mathbf{x}_i,t)$ under this scheme does not contain any spurious events related to the internal multiples from the overburden.

In practice, solving for the focusing functions is not always trivial. Various factors such as the accuracy of surface reflection response, wavelet deconvolution, source / receiver deghosting and attenuation all need to be taken into account (van der Neut et al., 2015b). In the light of these practical aspects, we suggest an approximate alternative. This is done by using eq. 3.1, 3.5, and the direct wave approximation for $G^{+}(\mathbf{x}_i|\mathbf{x}_0^{''},t)$ in eq. 3.14 for substitution in eq. 3.13, which gives

$$\Psi\left[\int_{\partial D_0}\hat{G}_d^{*}(\mathbf{x}_i^{'}|\mathbf{x}_0)\hat{\mathcal{R}}^{\cup}(\mathbf{x}_0^{''}|\mathbf{x}_0)d\mathbf{x}_0\right] \approx \int_{\partial D_i}\hat{\mathcal{R}}^{\cup}(\mathbf{x}_i^{'}|\mathbf{x}_i)\hat{G}_d(\mathbf{x}_i|\mathbf{x}_0^{''})d\mathbf{x}_i. \tag{3.18}$$

This scheme can be viewed as the result from the first iteration of the iterative Marchenko scheme in finding the focusing function. With this scheme, the retrieved response will contain some spurious events related to internal multiples. But this is still a good complement to the scheme based on the borehole data only (eq. 3.16), because in addition to being completely data-driven, it also incorporates information from the surface, and the approximation for the upgoing wavefield (eq. 3.15) is avoided.

Finally, one more alternative scheme is to combine eq. 3.16 and 3.18 (or analogously, eq. 3.13 and 3.17), and solve for $\mathcal{R}^{\cup}(\mathbf{x}_i'|\mathbf{x}_i,t)$, using MDD, for example. This joint system of equations reads, in matrix form:

$$\begin{bmatrix} \mathbf{U}_1 \\ \alpha\mathbf{U}_2 \end{bmatrix} = \mathbf{R} \begin{bmatrix} \mathbf{D}_1 \\ \alpha\mathbf{D}_1 \end{bmatrix}, \tag{3.19}$$

where $\mathbf{U}_1$ and $\mathbf{U}_2$ correspond to the left-hand sides of eq. 3.16 and 3.18, and $\mathbf{D}_1$ to the counterparts on the right-hand sides. Here, α is a user-defined scalar weight, which could be frequency-dependent, depending on the characteristics of both sub-problems and how much weight one wants for the surface data. Inverting this joint scheme might be better than inverting a single scheme (as eq. 3.16 or 3.18). Because in practice, there can be various hardware related issues in both datasets, such as sensor coupling, malfunctioning sensors, and etc.. In addition, the high frequency components in the borehole data can have a better signal to noise ratio than the same frequency components in the surface data (due to less attenuation), and borehole data may have higher propagation angles for imaging the structures that could not be found in the surface data. Therefore, this joint inversion approach could help to merge the datasets.

Fig.3.1 illustrates the processing flow for the schemes described in this subsection. To summarize, both eq. 3.17 remove all downgoing multiples coming from the overburden using single-component borehole and surface data with an iterative Marchenko approach; eq. 3.16, 3.18 and 3.19 do not completely remove all such downgoing multiples, but they are straightforward to implement and still sufficient for imaging near the borehole (which we will demonstrate with the numerical examples). Another benefit of these schemes is that the retrieved reflection responses are redatumed in a data-driven way to the borehole level for imaging downwards, such that one does not need any velocity information of the overburden. This is also an acknowledged aspect in the virtual source method by Bakulin and Calvert (2006), but our approach requires less information from the data (only single-component recordings).

3.2.3 Imaging from below

Again, assuming a horizontal borehole, we define imaging from below as to retrieve the reflection response from below (of the medium above the borehole), as if the medium below the borehole is reflection-free. Then an image above the borehole is obtained by applying a conventional depth migration algorithm to the retrieved response, using a local velocity model above the borehole. In other words, we aim to use borehole data and surface data to create a virtual dataset with both sources and receivers in the borehole, below which the medium is reflection-free.

This reflection response from below $\mathcal{R}^{\cap}(\mathbf{x}_i'|\mathbf{x}_i,t)$ ($^{\cap}$ denotes that this is the reflection response from below) is shown (Wapenaar et al., 2014) to be related to the focusing func-

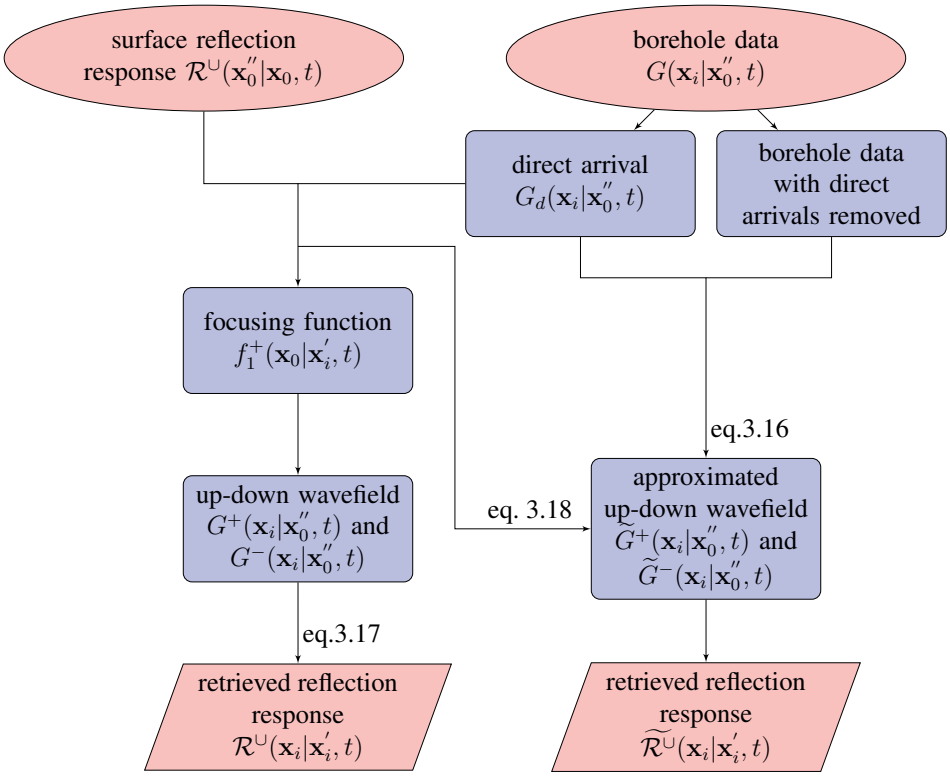

Figure 3.1: Flow chart for imaging from above. The ellipses indicate the input and the trapezia indicate the output. The intermediate steps are indicated by the boxes. The˜above the symbols indicates approximation.

tions via

$$f_2^+(\mathbf{x}_i^{'}|\mathbf{x}_0^{''},t) = \int_{\partial D_i}\int_{-\infty}^{+\infty} \mathcal{R}^{\cap}(\mathbf{x}_i^{'}|\mathbf{x}_i,t^{'}) f_2^-(\mathbf{x}_i|\mathbf{x}_0^{''},t-t^{'})dt^{'}d\mathbf{x}_i; \tag{3.20}$$

for this reason, to solve for $\mathcal{R}^{\cap}(\mathbf{x}_i^{'}|\mathbf{x}_i,t)$, we need the focusing functions $f_2^{\pm}$. But first, we can rewrite the above equation in terms of f_1^+, using the mutual relation of the focusing functions from eq. 3.12, and the relation from eq. 3.3, such as

$$-\left\{\Theta\left[\int_{\partial D_0}\hat{f_1^+}(\mathbf{x}_0|\mathbf{x}_i^{'})\hat{\mathcal{R}}^{\cup}(\mathbf{x}_0^{''}|\mathbf{x}_0)d\mathbf{x}_0\right]\right\}^* = \int_{\partial D_i}\hat{\mathcal{R}}^{\cap}(\mathbf{x}_i^{'}|\mathbf{x}_i)\hat{f_1^+}(\mathbf{x}_0^{''}|\mathbf{x}_i)d\mathbf{x}_i, \tag{3.21}$$

where the superscript * denotes conjugation. This equation gives the exact scheme for retrieving $\mathcal{R}^{\cap}(\mathbf{x}_i^{'}|\mathbf{x}_i,t)$. Again, here we switch to the frequency domain (indicated by the $\hat{}$) for previously stated reasons. Similar to Ψ, the operator Θ first inverse Fourier transforms the result, then applies a time window which passes data only for $t < t_d(\mathbf{x}_i^{'}|\mathbf{x}_0^{''})$, and then Fourier transforms the result back to the frequency domain. In this equation, $\hat{f}_1^+(\mathbf{x}_0^{''}|\mathbf{x}_i)$, is found by the same procedure as explained in the previous two subsections, and $\mathcal{R}^{\cup}(\mathbf{x}_0^{''}|\mathbf{x}_0)$ is the surface reflection response. Then the unknown $\hat{\mathcal{R}}^{\cap}(\mathbf{x}_i^{'}|\mathbf{x}_i)$ can be solved per frequency, using a least squares approach, for example. As the first iteration of the Marchenko scheme for $f_1^+(\mathbf{x}_0|\mathbf{x}_i^{'},t)$, an approximate alternative scheme is

$$-\left\{\Theta\left[\int_{\partial D_0}\hat{G}_d^*(\mathbf{x}_i^{'}|\mathbf{x}_0)\hat{\mathcal{R}}^{\cup}(\mathbf{x}_0^{''}|\mathbf{x}_0)d\mathbf{x}_0\right]\right\}^* \approx \int_{\partial D_i}\hat{\mathcal{R}}^{\cap}(\mathbf{x}_i^{'}|\mathbf{x}_i)\hat{G}_d^*(\mathbf{x}_i|\mathbf{x}_0^{''})d\mathbf{x}_i, \tag{3.22}$$

where eq. 3.5 is used. We notice that this scheme resembles the imaging from below method by Poliannikov (2011), because an approximate solution of $\mathcal{R}^{\cap}(\mathbf{x}_i^{'}|\mathbf{x}_i,t)$ by cross-correlation is equivalent to his result (which he derived from SRI). This cross-correlation solution is obtained by writing out the normal equation of eq. 3.22 and approximate the solution with the left-hand side of the normal equation. But we see now that because of the substitution of eq. 3.5, either solving eq. 3.22 by MDD or by cross-correlation results in spurious events in the retrieved $\mathcal{R}^{\cap}(\mathbf{x}_i^{'}|\mathbf{x}_i,t)$. Those spurious events related to the upgoing internal multiples can be removed by using the exact form in eq. 3.21. Nevertheless, when the internal multiples are not strong, eq. 3.22 is a simple and sufficient scheme for imaging close to the borehole. The flow chart in Fig. 3.2 illustrates the two schemes.

3.3 Numerical examples

In the numerical experiments, we use two 2-D acoustic models to test the redatumig schemes and to observe to what extent velocities errors affect the local images, as compared to conventional surface images (images obtained from surface data alone). The first

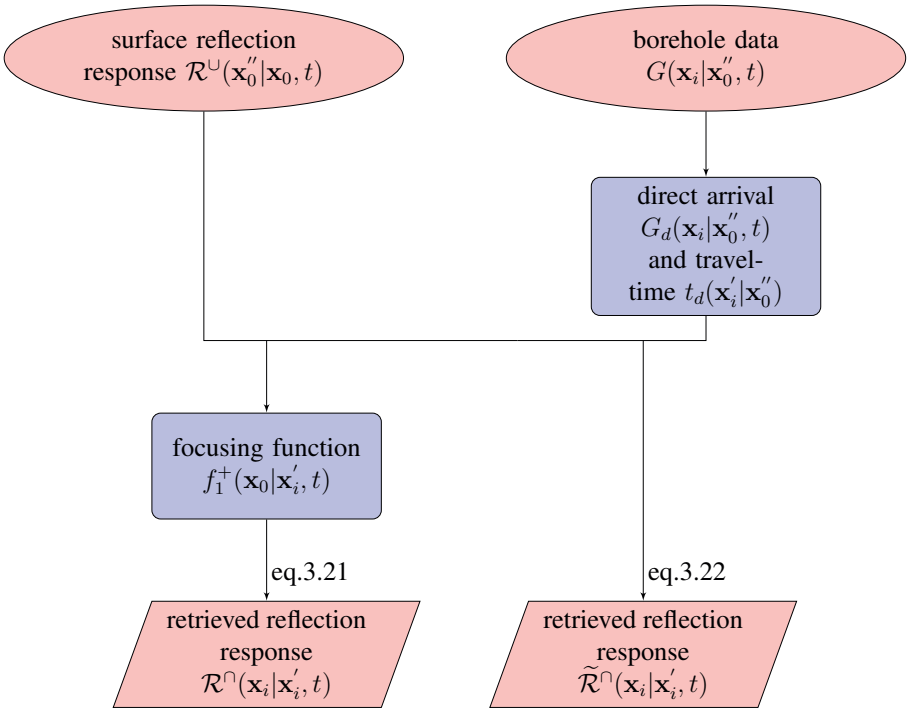

Figure 3.2: Flow chart for imaging from below. The ellipses indicate the input and the trapezia indicate the output. The intermediate steps are indicated by the boxes. The˜above the symbols indicates approximation.

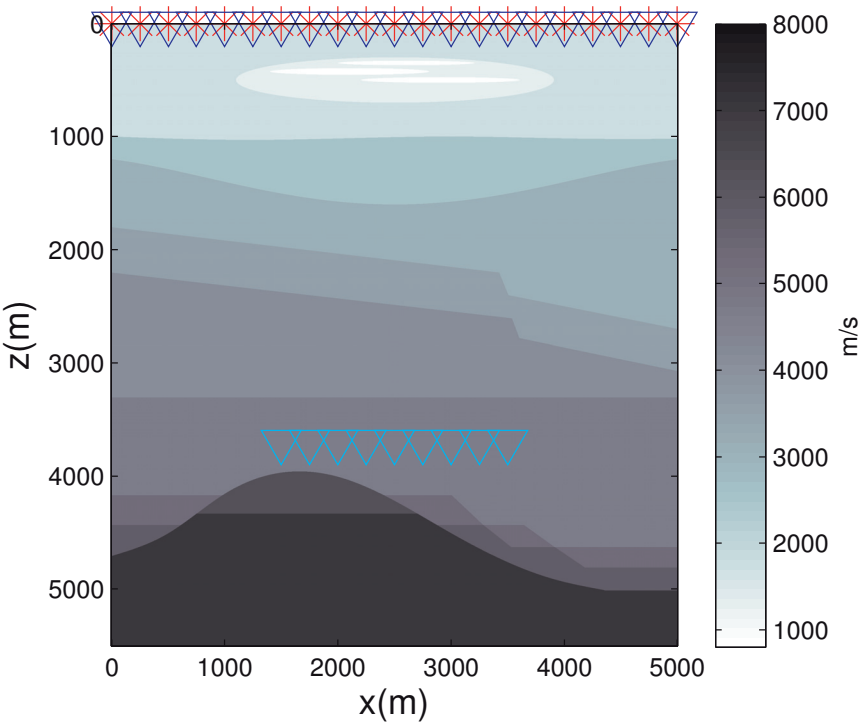

Figure 3.3: P-wave velocity model and datasets geometries. The stars denote sources and the triangles denote receivers. Every tenth source and receiver is plotted. Letters x and z represent horizontal and vertical directions, respectively.

model is a synthetic model with a gas cloud in the shallow part, and the second model is a realistic model of a field in the North Sea. A finite difference method (Thorbecke and Draganov, 2011) is used for generating the datasets. After redatuming, a prestack depth migration algorithm (Thorbecke et al., 2004) is used for imaging. For each model, we generate two datasets - a surface dataset (with sources and receivers at the surface) and a borehole dataset (with sources at the surface and receivers in the borehole). The surface data is modelled as the response to an input band-limited spike with a maximum frequency of 55 Hz, and the borehole data is modelled with a Ricker wavelet with a peak frequency of 20 Hz. The free surface is replaced by an absorbing boundary.

3.3.1 Example 1: local imaging below a gas cloud

Fig. 3.3 shows the P-wave velocity model and the input datasets geometries. The model is 5 by 5.5 km, with a grid sampling of 2.5 m. It consists of a low-velocity gas cloud in

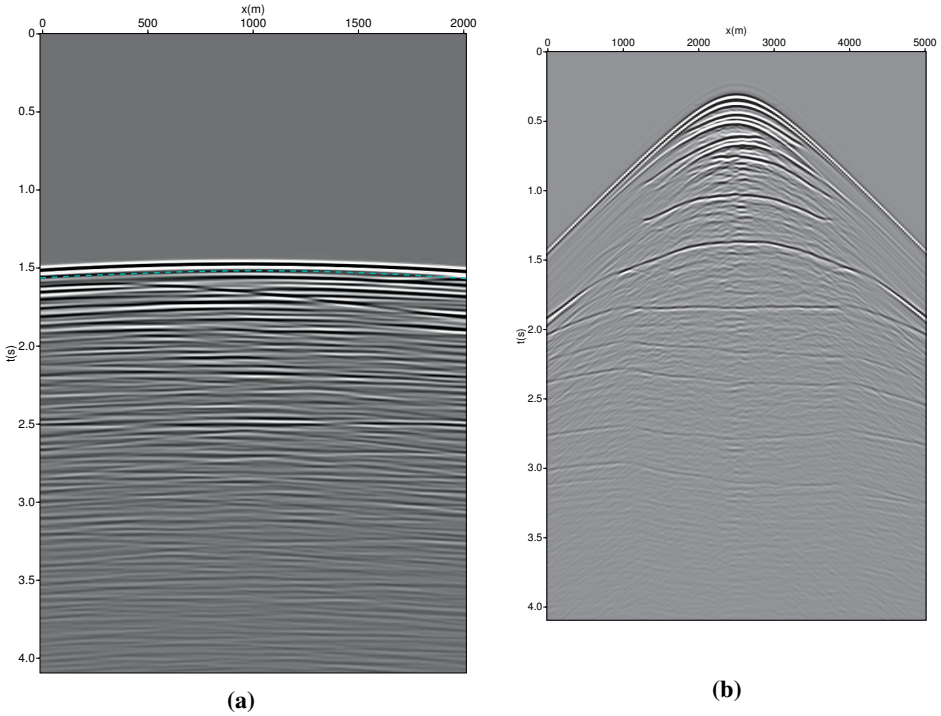

Figure 3.4: An example of the common-source gathers from a) borehole data and b) surface data (the direct arrivals are muted). The dashed line indicates the time window found by the direct arrival's traveltime in the borehole data.

the shallow part (around 0.5 km depth) and a syncline alongside some faults in the deeper part (below 4 km). The borehole dataset has 201 sources at the surface and 81 receivers at 3.7 km depth. The surface dataset has 201 sources and receivers. The source and receiver intervals are 25 meters. Examples of the common-source gathers from both datasets are shown in Fig. 3.4. The time window is found by the traveltime $t_d(\mathbf{x}_i^{'}|\mathbf{x}_0^{''})$ in the borehole data and it is indicated by the dashed line in the figure.

Redatumed reflection responses

To retrieve the reflection response from above, $\mathcal{R}^{\cup}(\mathbf{x}_i^{'}|\mathbf{x}_i, t)$, we test four schemes, namely, eq. 3.16, 3.18, 3.17, and 3.19. Fig. 3.5 shows the comparison between the redatumed reflection responses (in red) and the reference response (in blue). The reference response (direct arrivals muted) is modelled with a homogeneous overburden above the borehole. The reference source position is at $x = 2500$ m at the depth of 3.7 km. An overall scalar is applied on the retrieved responses to scale with the reference response. In addition, a local extra gain is applied both on the reference and retrieved responses for $t > 1s$ to

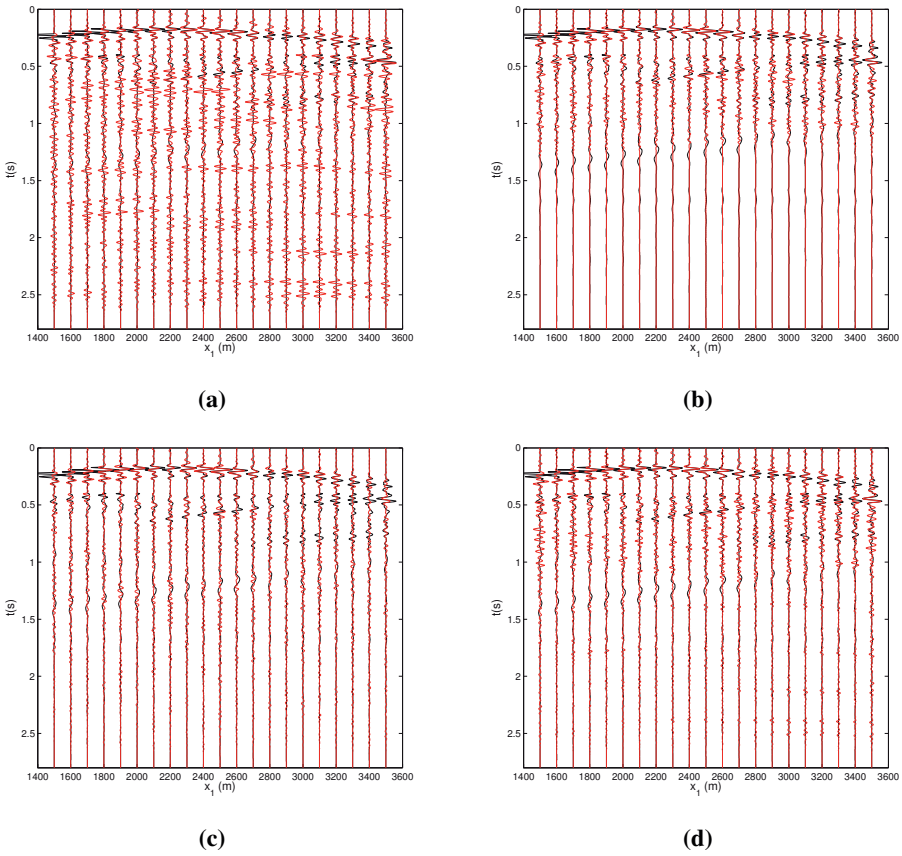

Figure 3.5: Redatumed reflection responses for imaging from above. Trace comparison between the retrieved responses and the reference responses, using a) single-component borehole data only (eq. 3.16), b) surface reflection data and the direct arrivals in the borehole data (eq. 3.18), c) the same input as b) but the focusing functions are found by an iterative Marchenko method (eq. 3.17) and d) a joint scheme of a) and b) (eq. 3.19). The color black indicates the modelled reference response and the color red indicates the redatumed response. An overall scale is applied on the retrieved responses and a local scalar gain is applied for $t > 1s$ to amplify the multiples. The low frequency events in the reference response are due to the imperfect absorbing boundary in the forward modelling. Every fourth trace is plotted.

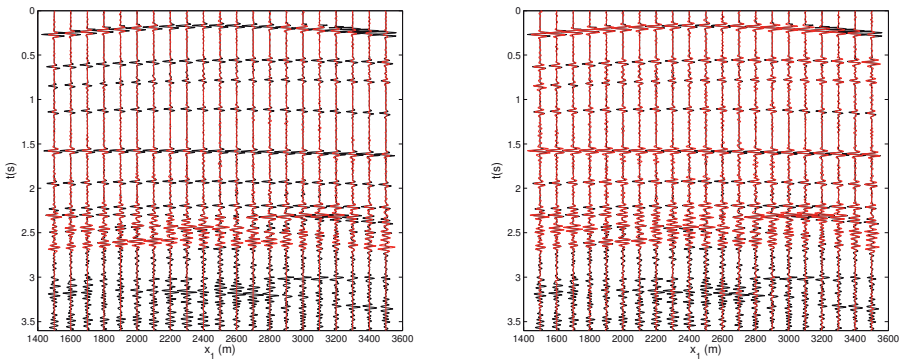

(a) **(b)**

Figure 3.6: Redatumed reflection responses for imaging from below. Trace comparison between the retrieved responses and the reference responses, using a) direct arrivals in the borehole data, together with the surface reflection response (eq. 3.22) and b) surface reflection response and the focusing functions ((eq. 3.21, using the direct arrivals in the borehole data and the surface reflection response as input to the iterative Marchenko method). An overall scale is applied on the retrieved responses and a local gain is applied for $t > 3s$ to amplify the multiples. Every fourth trace is plotted.

amplify the internal multiples.

For the first scheme (eq. 3.16), only the borehole dataset is used, and the scheme is closely related to the virtual source method by Bakulin and Calvert (2006), where their result is obtained by the crosscorrelation of the left-hand side of eq. 3.16 with the direct arrivals on the right-hand side. Here, we solve eq. 3.16 per frequency by MDD. For the second scheme (eq. 3.18), the surface dataset is included to redatum the direct arrivals in the borehole data for approximating the upgoing component in the exact scheme. For the third scheme(eq. 3.17), the input is the same as for the second scheme, but an iterative Marchenko method (Wapenaar et al., 2014) is used to find the focusing functions, with the direct traveltime $t_d(\mathbf{x}_i^{'}|\mathbf{x}_0^{''})$ from the borehole dataset. For the fourth scheme (eq. 3.19), we joined the schemes one and two with an α of 2. All equations are solved using a damped least-squares approach (Menke, 1989).

By comparing the traces in Fig. 3.5, it can be observed that panel a) has the most spurious events, but mainly in the later arrivals. This is because the approximations in eq. 3.14 and 3.15) do not account for the internal multiples. These downgoing events are almost completely removed in panel c), where the up-down wavefields are properly decomposed in the exact scheme.

To retrieve the reflection response from below, $\mathcal{R}^{\cap}(\mathbf{x}_i^{'}|\mathbf{x}_i, t)$, we test two schemes, namely (eq. 3.22 and 3.21). Fig. 3.6 shows the comparison between the redatumed result in red and the reference response in black. The reference response (direct arrivals muted) is

modelled with a homogeneous underburden below the borehole. The reference source position is $x = 2500$m at the depth of 3.7 km.

In the trace comparison, an overall scalar factor is applied on the redatumed result, and an extra gain is applied for $t > 3s$ to amplify the multiples. One can see that the second scheme which uses the focusing functions results in a better match, both in terms of the amplitude and fewer spurious events. Nevertheless, the first scheme still recovers the nearby reflectors well.

Target images

Next, the redatumed reflection responses are used for imaging from above and from below the borehole, respectively. First, the true local velocities are used for migration. The results are shown in Figs. 3.7 and 3.8. We see that the nearby reflectors are all clearly imaged in both figures, even though they are hindered by the gas cloud at the surface. Furthermore, no medium parameter of the gas cloud is needed for imaging the structures underneath. In terms of the influence of internal multiples on imaging, we see that it is the most obvious in the image from below in Fig. 3.8 b) where the correct focusing function is computed. In this case, the strong internal multiples from the underburden are removed.

To test the robustness of the target images to velocity errors and to compare with conventional surface images, we first use a smoothed true velocity model to migrate the redatumed results by the schemes in eq. 3.17 and 3.21 (corresponding to Fig. 3.5 c) and 3.6 b)). The original surface data is also migrated using the same smoothed model. The result is shown in Fig. 3.9. We can see already that surface image struggles to image the deep reflectors because of the gas cloud, while the target images position these reflectors clearly and correctly. To further demonstrate the benefit of this data-driven redatuming, a 1-D linear velocity model is used and the result is shown in Fig. 3.10. Now the deep reflectors can barely be recognized in the surface image, while, even though less focused, they remain clearly present in the target images. In addition, the reflectors near the borehole are less mispositioned than in the surface image.

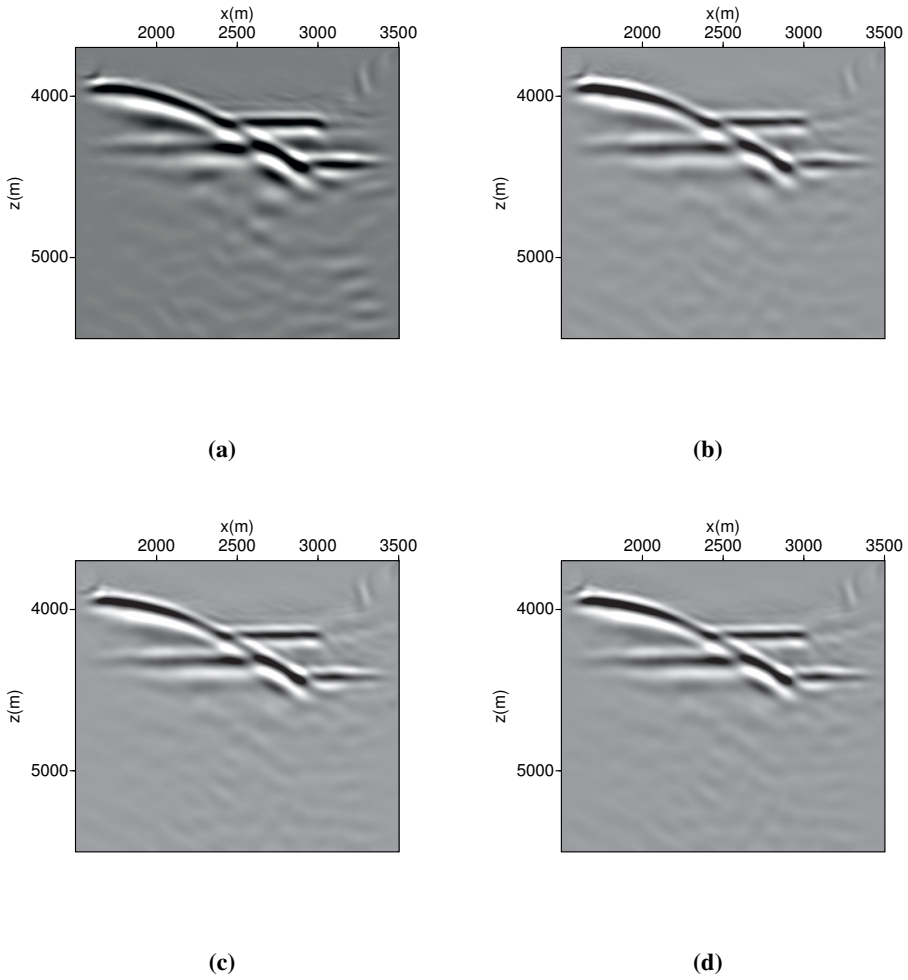

Figure 3.7: Migrated images from above with the correct local velocities. The data for migration are redatumed from a) the borehole data only scheme (eq. 3.16), b) the borehole and surface data scheme without the full focusing functions (3.18), c) as b) but with the full focusing functions (eq. 3.17) and d) the joint scheme of a) and b) (eq. 3.19).

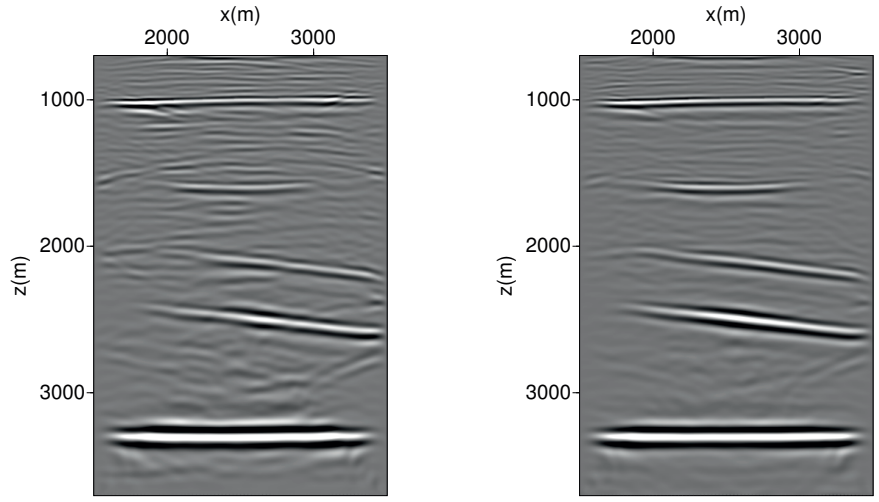

(a) **(b)**

Figure 3.8: Migrated images from below with the correct local velocities. The data for migration are redatumed from a) the borehole and surface data scheme without the full focusing functions (eq. 3.22), b) as a) but with the correct focusing functions (eq. 3.21).

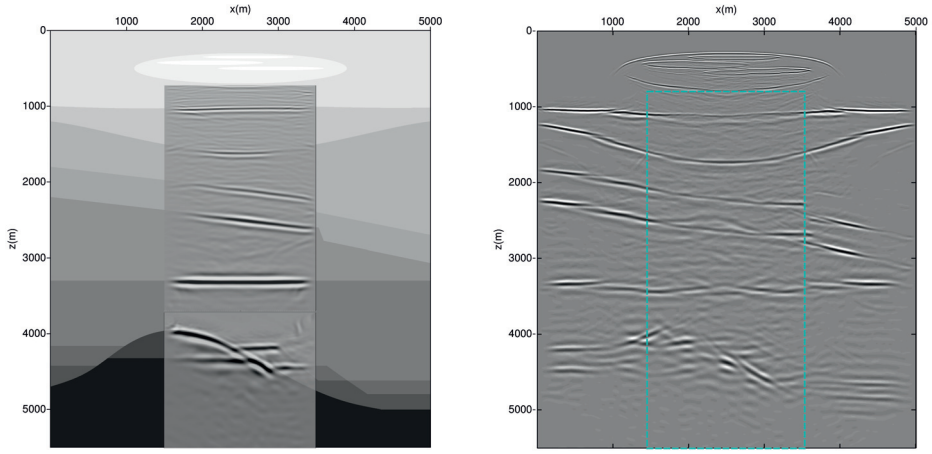

(a) **(b)**

Figure 3.9: Image comparison of a) target images from the redatumed data using the focusing functions (eq. 3.17 and 3.21) and b) surface image from original surface reflection data. The dashed box highlights the target area. The true velocity model is used for migration.

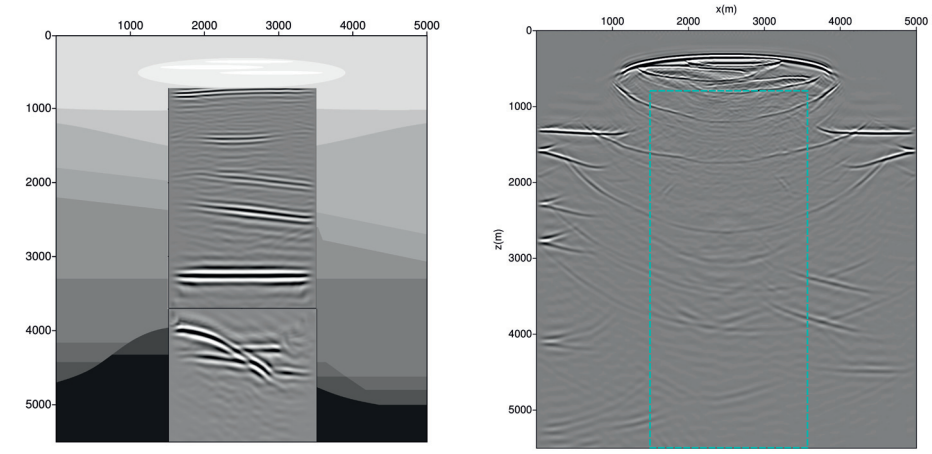

(a) **(b)**

Figure 3.10: Image comparison of a) target images from the redatumed results and b) surface image from original surface reflection data. The dashed box highlights the target area. A simple 1-D linear velocity model is used for migration.

3.3.2 Example 2: a realistic model from the North Sea

Fig. 3.11 shows the 2-D P-wave velocity model and the input datasets geometries. The model dimension is 6 by 4.2 km, with a grid sampling of 5 m. There is a seagull shaped low velocity anomaly at around 1.5 km depth. The borehole dataset has 241 sources at the surface and 81 receivers at 2.3 km depth. The surface dataset has 241 sources and receivers. The source and receiver intervals are 25 meters. Examples of the common-source gathers from both datasets are shown in Fig. 3.12.

Redatumed reflection response

Fig. 3.13 and 3.14 show the redatumed reflection responses for imaging from above and from below, respectively. An overall scalar factor is applied on the result. In addition, an extra gain is applied both on the reference and retrieved responses for $t > 1.2s$ in the figures to amplify the internal multiples. We observe that all schemes result in good kinematic matches for the reflectors near the borehole. In Fig. 3.13 a) where only the borehole data is used in the redatuming scheme, the later arrivals don't match the reference response well, but the match is already improved when the surface data is included, as seen in panel b). This is because the left-hand-side of eq. 3.16 contains downgoing multiples, which are not removed because the upgoing wavefield is approximated crudely by muting the direct wavefield in the total wavefield (eq. 3.15). With eq. 3.18, the upgoing wavefield is constructed by back propagation of the surface data, so the approximation to the upgoing wavefield is improved.

Then when the focusing function is computed, most of the spurious events related to the downgoing multiples from the overburden are removed and the match is improved even more. The amplitude mismatch in the far offset traces could be because there isn't a wide enough coverage of sources and receivers at the surface and in the borehole. In other words, only part of the surface integrals can be computed in practice because of the limited data acquisition apertures, but nevertheless, the kinematics of the reflections is retrieved as long as the stationary phase positions are covered in the input data (Snieder et al., 2006). Actually, in Fig. 3.14 b), all primaries and multiples matches well in both travel time and amplitude. These results verify the suggested redatuming schemes.

Target images

We first test the target images using the correct local velocities. The corresponding images from above and from below are shown in Fig. 3.15 and 3.16, respectively. For the images from above in Fig. 3.15, all four images show the nearby reflectors. Panel c) is the best focused and shows more details because the downgoing multiples from the overburden are removed. This is even more obvious in Fig. 3.16 b), the images from below, where all upgoing multiples from the underburden are removed, and the shallow structures can be seen clearly.

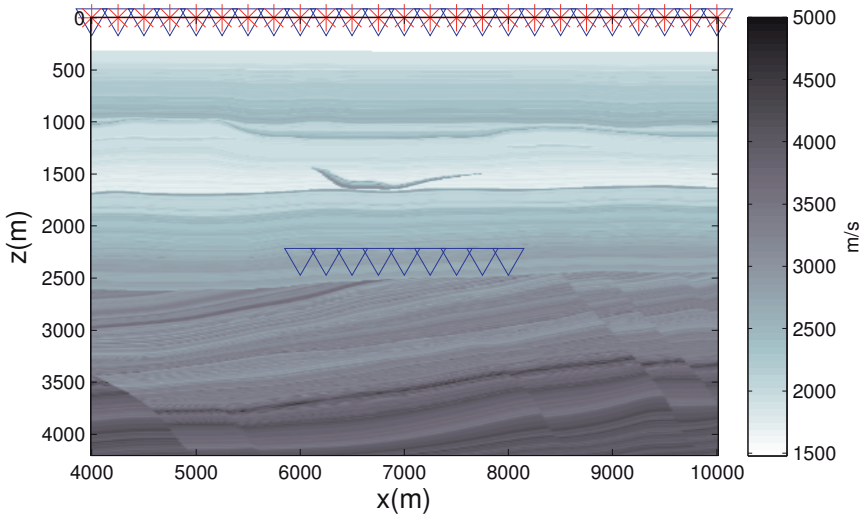

Figure 3.11: P-wave velocity model and datasets geometries. The stars denote sources and the triangles denote receivers.

Next, Fig. 3.17 a) combines the target images in Fig. 3.15 c) and Fig. 3.16 b) and plots them over the true velocity model. Panel b) shows the conventional surface image migrated with the correct velocities. Even with the correct velocities, we can see that the surface image of the area $z > 2$ km is disturbed by the internal multiples from the "seagull", while the target images show the structures in the same area more clearly and continuously.

Again, to test how the target images change when the wrong velocities are used, a linear 1-D velocity model is used to migrate both the redatumed responses and the original surface dataset. The comparison is shown in Fig. 3.18, where the arrow highlights an example of the effect from internal multiples. From these two tests with different migration velocity models, we see that the target images are robust to erroneous velocities and provide clearer reflectors near the borehole than the surface image, and that the imprint of the internal multiples are less pronounced. Another point is that one actually does not need the velocity model of the overburden at all for imaging below the borehole level, as explained in the imaging from above subsection. Nevertheless, this is not to say that a good velocity model is not important. We merely suggest that one may be able to start with a more crude model and still get some focusing near the boreholes, and then later improve the velocity model with standard techniques.

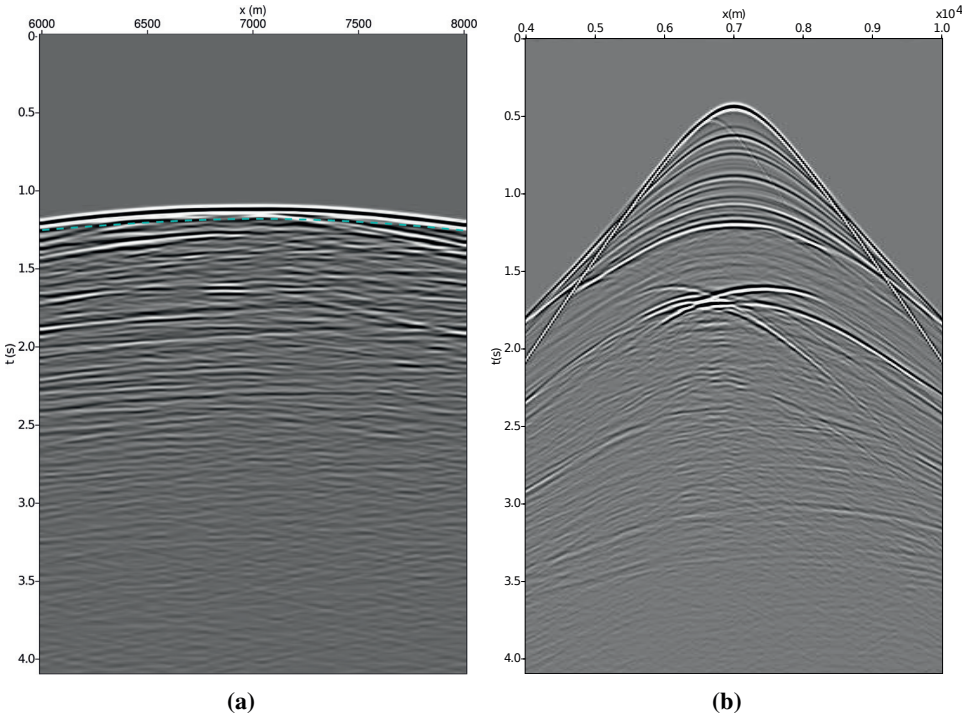

(a) **(b)**

Figure 3.12: An example of the common-source gathers from a) borehole data and b) surface data (the direct arrivals are muted). The dashed line indicates the time window found by the direct arrival's traveltime.

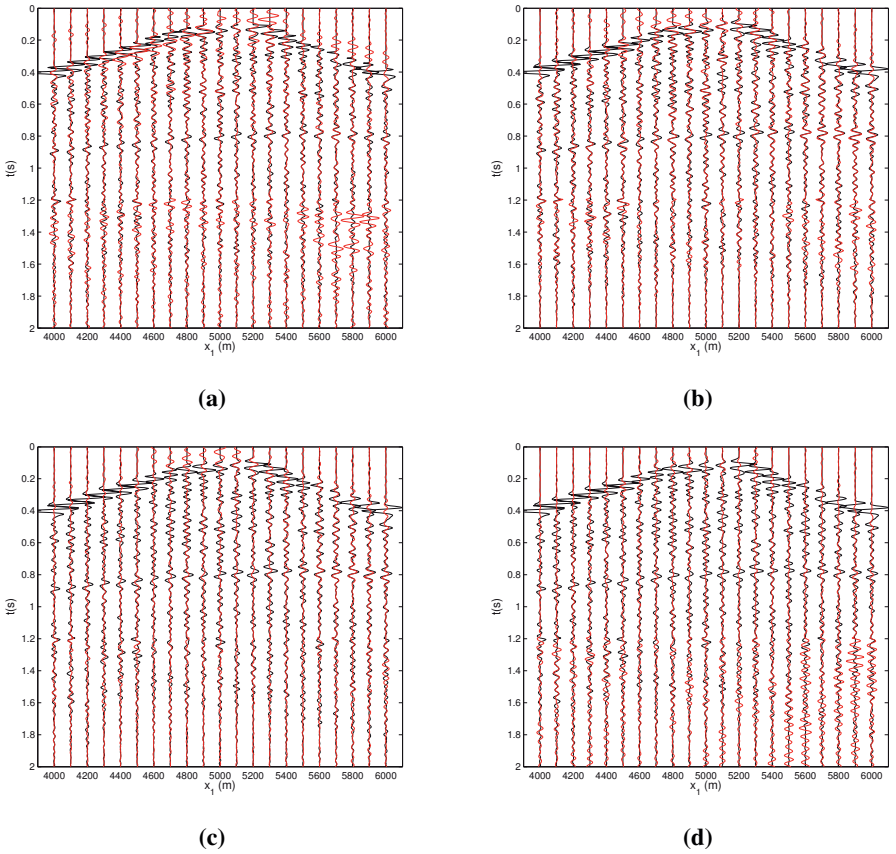

Figure 3.13: Redatumed reflection responses for imaging from above, using the same schemes as for Fig. 3.5. The reference source position is at $x = 7000$m at 2.3 km depth, and the receiver positions are from $x = 6000$m to $x = 8000$m at the same depth as the virtual source. An overall scale is applied on the retrieved responses and a local extra scalar factor is applied for $t > 1.2s$ onward to emphasize the multiples. Every fourth trace is plotted.

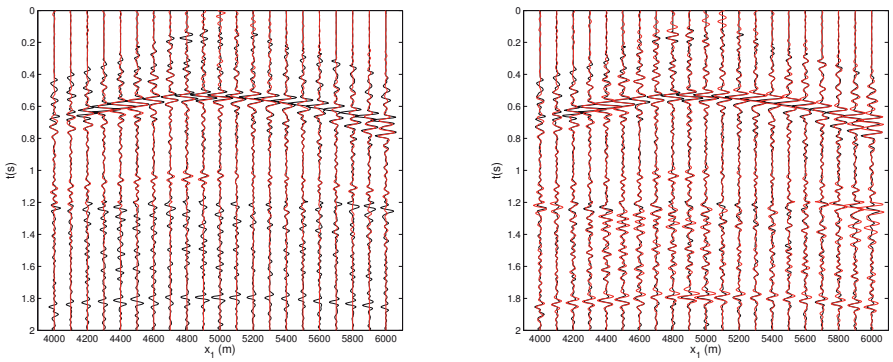

(a) **(b)**

Figure 3.14: Redatumed reflection responses for imaging from below, using the same schemes as for Fig. 3.6. The reference source and receiver positions are the same as for Fig. 3.13. An overall scale is applied on the retrieved responses and a local gain is applied for $t > 1.2s$ to amplify the multiples. Every fourth trace is plotted.

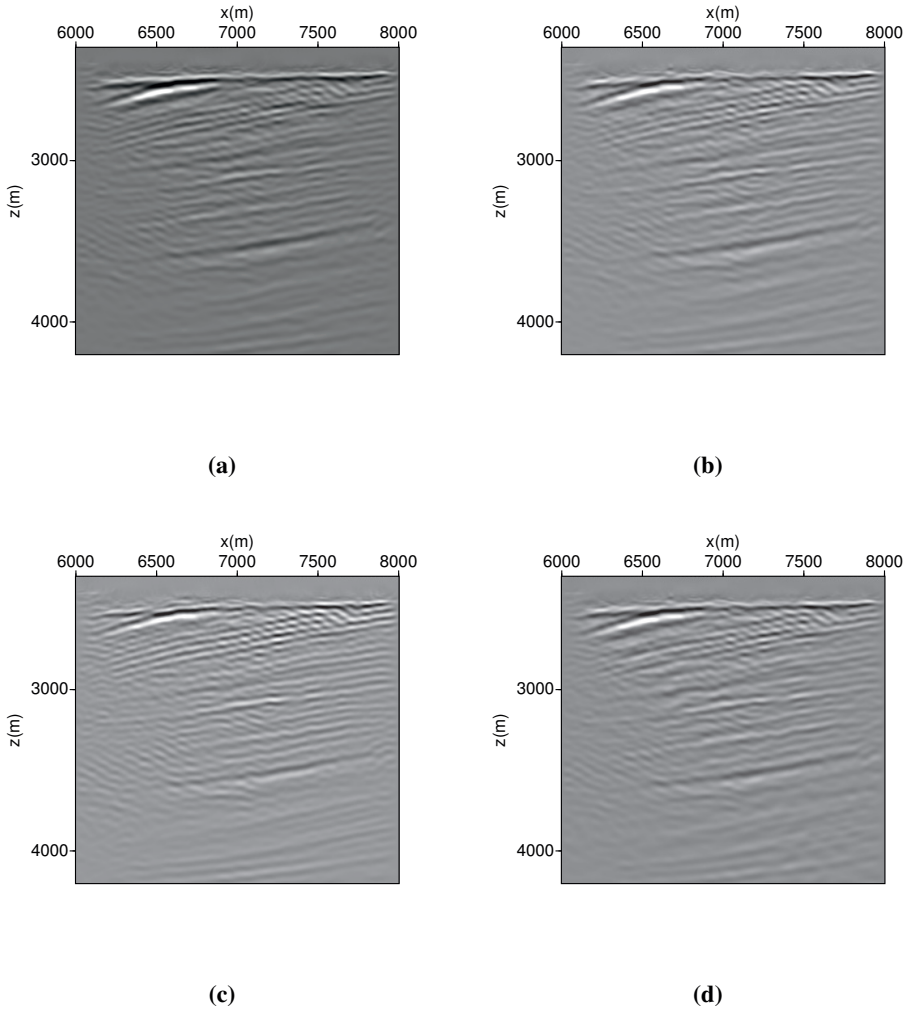

Figure 3.15: Migrated images from above with the correct local velocities. The data for migration are redatumed from a) the borehole data only scheme (eq. 3.16), b) the borehole and surface data scheme without the full focusing functions (3.18), c) as b) but with the correct focusing functions (eq. 3.17) and d) the joint scheme of a) and b) (eq. 3.19).

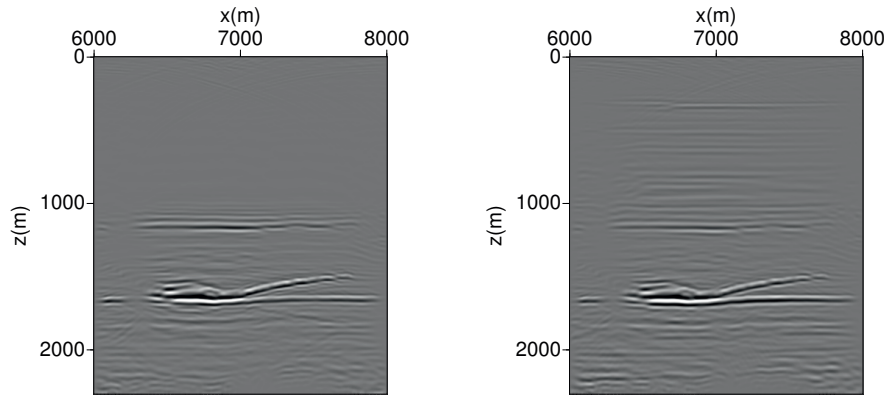

(a) **(b)**

Figure 3.16: Migrated images from below with the correct local velocities. The data for migration are redatumed from a) the borehole and surface data scheme without the full focusing functions (eq. 3.22), b) as a) but with the full focusing functions (eq. 3.21).

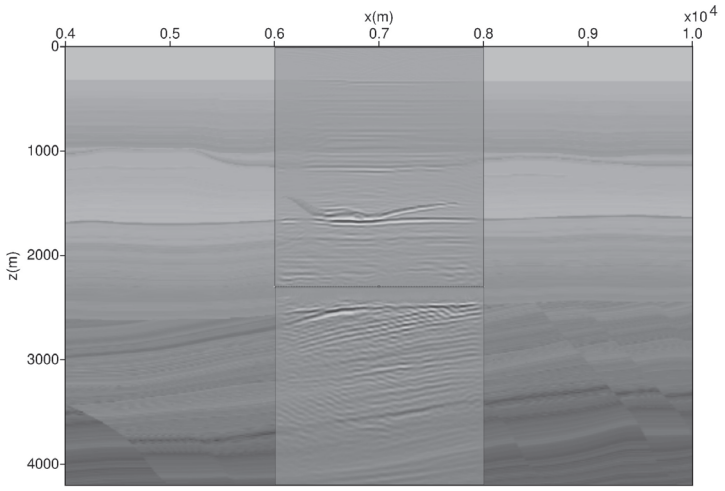

(a)

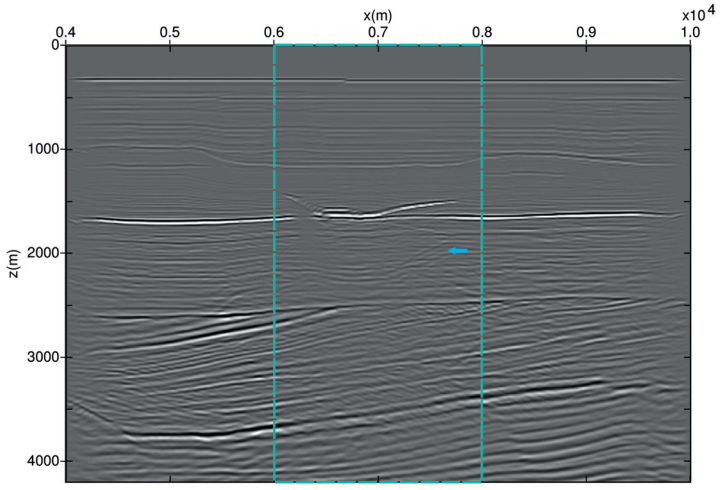

(b)

Figure 3.17: Image comparison of a) target images from the redatumed data using the focusing functions (eq. 3.17 and 3.21) and b) surface image from original surface reflection data. The dashed box highlights the target area. The arrow indicates an example of the artefacts from internal multiples. A true velocity model is used for migration.

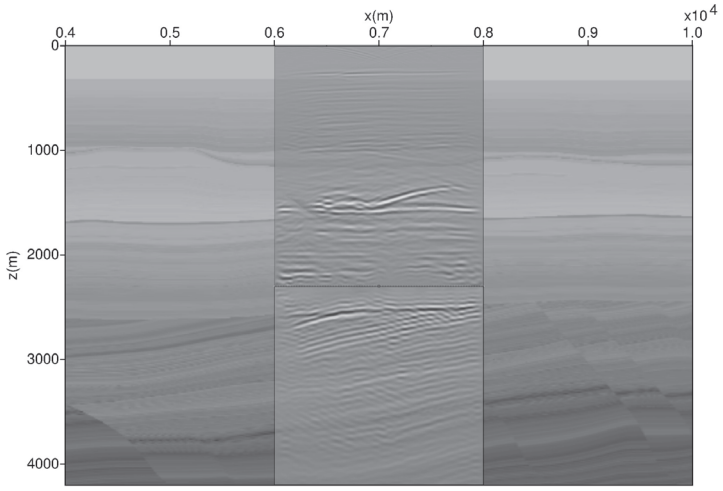

(a)

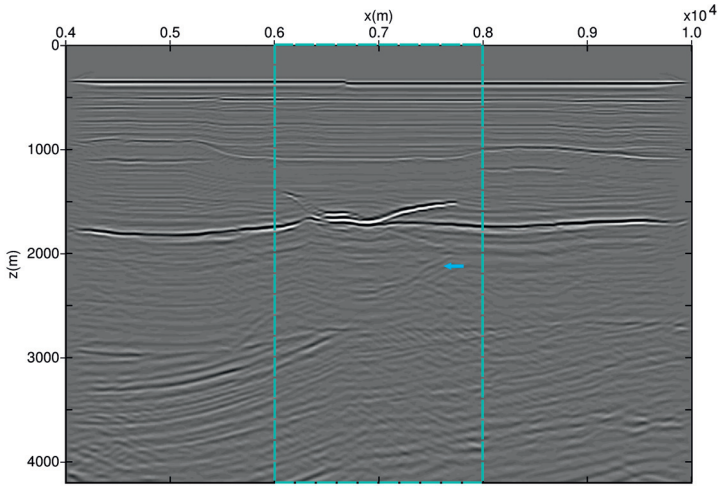

(b)

Figure 3.18: Image comparison of a) target images from the redatumed results and b) surface image from original surface reflection data. The dashed box highlights the target area. The arrow indicates an example of the artefacts from internal multiples, which become more pronounced given the wrong velocity model. These artefacts are absent in the target image in panel a). A simple 1-D linear velocity model is used for migration.

3.4 Discussion

As demonstrated in the numerical examples, the redatuming schemes remove part of the internal multiples. The multiples from the target zone still remain, since only the multiples from the opposite side of the target zone are removed. This results in an improvement in the images produced as seen in the numerical examples, especially when the velocity model is wrong. Because internal multiples tend to stack out destructively when a good velocity model is available, and when the velocities are wrong, the primaries interfere less constructively and the imprint from the internal multiples becomes more pronounced. For this reason, our redatuming schemes prior to the imaging step can be particularly beneficial for areas with strong multiples and velocity uncertainties.

A wide enough acquisition aperture in the input data is important, because all stationary phase positions for the target zone need to be covered. In our test, since only a 20 Hz Ricker wavelet is used for modelling the borehole data, the resolution of the images is limited and could be improved if higher frequencies are used. For the surface data, in order to find the correct focusing function, we model the reflection response to an input spike, but for data acquired in the field, they correspond to the Green's function convolved with the source signature. Therefore, a good source signal estimation is required in practice in order to take full advantage of the schemes presented. The proposed alternative schemes do not have this requirement and are often still sufficient solutions for imaging local geological structures in the presence of velocity errors in the model, as shown in the experiments.

The schemes as presented assume that the borehole is at a constant depth, but the method can be immediately adapted to include non-horizontal boreholes by extrapolating the direct arrivals in the borehole data to a constant depth using the forward Kirchhoff-Helmholtz integral (Wapenaar, 1993). The extension to retrieve the reflection response defined locally according to the borehole orientation, however, still needs to be investigated. The surface related multiples are not considered in the schemes, but Singh et al. (2015) show how to take them in account in the Marchenko method, so this can also be done here. Another suggestion for future study is the possibility of using more than the direct arrivals in the borehole data for finding the focusing functions, and this is currently being investigated. It is also observed that images from the surface and from the borehole (when imaging from below) inherit a different sensitivity to errors in the velocity model. Similar observations have also been made by Ravasi and Vasconcelos (2015) and might be used for updating the velocity model.

3.5 Conclusions

We present a novel application of seismic interferometry and Marchenko imaging, using both surface and borehole seismic data. A series of redatuming schemes that require only single-component data are presented to create virtual datasets with both sources and

receivers in the borehole. These virtual datasets are ideal for deep target imaging near the borehole, because the medium properties in the shallower part become irrelevant when imaging using these datasets and the virtual sources and receivers are close to the target area. Furthermore, cleaner and more accurate images are obtained because the interfering internal multiples from the overburden and underburden are removed in the redatuming schemes. Finally, the numerical experiments also show that these images are more robust to velocity errors in the model than conventional surface images. Good deep target images are obtained with simple velocity input after applying these redatuming schemes.

3.6 Acknowledgments

The authors acknowledge the Research Council of Norway, ConocoPhillips, Det norske oljeselskap, Statoil, Talisman, TOTAL and Wintershall for financing the work through the research centre DrillWell - Drilling and Well Centre for Improved Recovery. The contribution of Joost van der Neut is financially supported by the Dutch Technology Foundation (grant VENI.13078). We also like to acknowledge the ROSE consortium at NTNU, Jan Thorbecke at TU Delft, and Alexander Kritski at Statoil for the field velocity model. We appreciate the review and comments of Rene-Edouard Plessix, the Editor, and Filippo Broggini, which helped improve this paper.

Chapter 4

Up-down wavefield retrieval in boreholes using single-component data

Yi Liu[1], Børge Arntsen[1], Joost van der Neut[2], Kees Wapenaar[2]

[1]Norwegian University of Science and Technology
[2]Delft University of Technology

Submitted to *Journal of Applied Geophysics* in 2017

Abstract

A standard procedure in processing vertical seismic profile (VSP) data is the separation of up-down wavefields. We show that the up-down wavefields in boreholes can be retrieved using only single-component borehole data, given that a full set of surface reflection data is also available. No medium parameters are required. The method is wave-equation based for a general inhomogeneous lossless medium with moderately curved interfaces. It relies on a focusing wavefield from the Marchenko method, which is a wavefield that satisfies certain focusing conditions in a reference medium. The up-down wavefields are then retrieved at borehole positions using from the surface reflection response. The method is applicable to boreholes with any general orientation, and no receiver array is required. Numerical results from a field in the North Sea are presented using three different borehole geometries (horizontal, deviated and vertical), and the results agree with the standard separation methods. Practical aspects for field application are discussed.

4.1 Introduction

Seismic data acquired in boreholes have long been used in aiding the geological interpretation of the subsurface. For vertical wells, these data are called vertical seismic profiles (VSP). VSP data are useful for identification and confirmation of the events seen on surface seismic data, seismic-stratigraphic analysis, seismic velocity analysis and calibration, imaging and time-lapse reservoir monitoring, and predicting ahead of the drill bit (Hardage, 1985; Poletto et al., 2004). Overviews of conventional VSP processing techniques and successful field examples can be found in Kennett et al. (1980) and Balch et al. (1982).

Due to its acquisition geometry, an important VSP processing step is the separation of the up-down wavefields. The benefits include the removal of the effects of complex overburden, e.g. multiples, by subsequent deconvolution. Conventional VSP up-down separation methods are based on the separation of different apparent velocities (or dip) of the up-down wavefields. Velocity filters are commonly used to separate them in the frequency-wavenumber (f-k) domain (Embree et al., 1963; Treitel et al., 1967). Other f-k filters, such as median filters (Stewart, 1985; Duncan and Beresford, 1995) and optimum filters (Seeman and Horowicz, 1983) have been used. Besides the separation in the f-k domain, separation in the τ-p domain after applying Randon transform is suggested by Moon et al. (1986). In this approach, the up-down components are mapped to different τ-p quadrants according to their dips so that they can be separated. This technique is useful when the separation is difficult in the f-k domain.

With the availability of multi-component data, more sophisticated wave-equation based decomposition methods are developed. Dankbaar (1985) proposes a decomposition scheme which uses weighted summations of vertical and horizontal geophone measurements in the f-k domain. Wapenaar et al. (1990) present a scheme to decompose land surface data into up-downgoing P- and S-waves. Other separation methods that are based on eigenvalue decomposition of the equation of motion with certain boundary conditions in horizontally-layered media (Ursin, 1983) show that the up-down wavefields can be computed as an angle-dependent combination of two or more measured data components. Barr and Sanders (1989) show the use of a scalar combination of the hydrophone (pressure) and vertical geophone (particle velocity) measurements to suppress water-column reverberations. This approach is commonly referred to as PZ summation. It is simple to implement but valid for normal incidence only. The angle-dependent decomposition for multi-component sea-floor data is proposed by Amundsen (1993); Amundsen and Reitan (1995). The method requires the seabed velocity and density. Schalkwijk et al. (2003) propose a 5-step adaptive decomposition scheme that obtains the necessary information from data, and it is further extended by Muijs et al. (2004) to be applied in an efficient automated manner.

In this paper, we show another approach that is also wave-equation based, but retrieves the up-down wavefields in boreholes using only the acoustic pressure data recorded at the surface and in the borehole. The method is valid for a general lossless inhomoge-

neous medium with moderately curved interfaces. It accounts for all internal multiples and is not limited to normal incidence. No medium parameters are required, and it can be used for a single borehole receiver (no receiver array is needed). The method uses the so-called focusing wavefields from the Marchenko method (Rose, 2002; Broggini et al., 2012; Wapenaar et al., 2013; Behura et al., 2014), which are computed from the surface reflection data and the borehole data. Then the up-down wavefields at the borehole receiver positions retrieved using these focusing wavefields. We show that the method works for any general borehole orientation, and the results agree with those by other methods. This approach is tested with synthetic data from the Norwegian Sea. Three borehole geometries are included, namely, the horizontal, the deviated, and the vertical. The retrieved up-down wavefields are compared with those by conventional methods in each case. Discussion and conclusion are made based on the numerical results.

4.2 Method

It is known that the up-down wavefields in the subsurface with sources at the surface can be retrieved by the Marchenko method (Wapenaar et al., 2014). It requires surface reflection responses and the direct wavefields from each position in the model to the surface source positions, so a smooth background velocity model is needed. An inaccurate velocity model can affect the retrieved results to various degrees (Thorbecke et al., 2013; de Ridder et al., 2016). However, as these travel times are measured in borehole data, it enables an accurate and velocity-free up-down retrieval scheme. The scheme requires only the pressure dataset (P) measured in the borehole and at the surface.

4.2.1 The up-down wavefield retrieval

First, we introduce Fig. 4.1 for the notation and the data geometries in this method. A spatial position is denoted as $\mathbf{x}_i = (\mathbf{x}_H, x_{3,i})$, where $\mathbf{x}_H = (x_1, x_2)$ represents the horizontal position and $x_{3,i}$ represents the depth level. For example, $\mathbf{x}_0^{''}$ represents a position at a lateral coordinate $\mathbf{x}_H^{''}$ at the surface level ∂D_0, and similarly, $\mathbf{x}_i^{'}$ represents a position at a lateral coordinate $\mathbf{x}_H^{'}$ at a subsurface level ∂D_i. The surface level ∂D_0 is defined as a transparent boundary, indicated by the dashed line in the figure, so the free surface reflections are excluded.The green line shows a general borehole, and each borehole receiver position is denoted as $\mathbf{x}_i$, where i varies according to the depth. In other words, the borehole does not need to be horizontal. The blue color indicates the known surface reflection response $\mathcal{R}^{\cup}(\mathbf{x}_0^{''}|\mathbf{x}_0, t)$ recorded at $\mathbf{x}_0^{''}$ from a source at $\mathbf{x}_0$. The red color indicates two of the unknown quantities, the downgoing components of the focusing function $f_1^{+}(\mathbf{x}_0|\mathbf{x}_i^{'}, t)$ and of the pressure wavefield $G^{+}(\mathbf{x}_i^{'}|\mathbf{x}_0^{''}, t)$. More on the focusing functions will be explained, but first, the relation between the blue and the red quantities is discussed (Wapenaar et al., 2014).

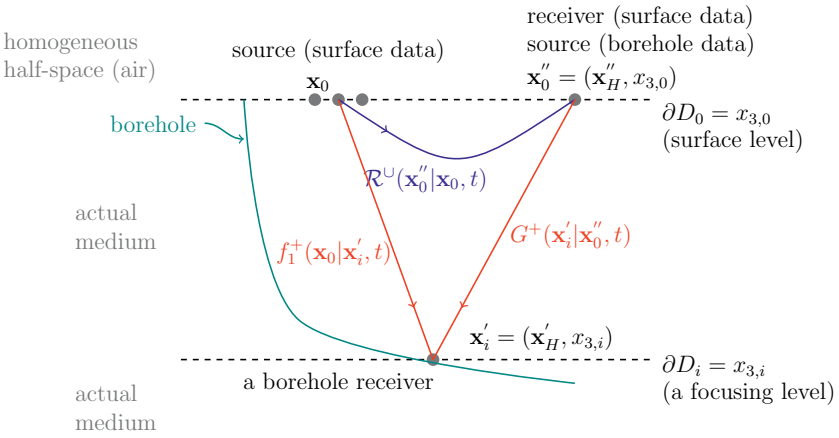

Figure 4.1: Notation convention and data acquisition overview. Each spatial position is denoted by $(\mathbf{x}_H, x_{3,i})$, with $\mathbf{x}_H = (x_1, x_2)$, and i represents a certain depth level. Here ∂D_0 denotes a transparent surface level, above which the medium is homogeneous, and ∂D_i denotes a focusing level (below which the medium is reflection-free for the focusing function, see Fig. 4.2). The blue solid line represents the known surface reflection response $\mathcal{R}^{\cup}(\mathbf{x}_0''|\mathbf{x}_0, t)$ after source deconvolution and surface multiple removal. The red solid lines represent the unknown quantities, where $f_1^+(\mathbf{x}_0|\mathbf{x}_i', t)$ is the downgoing component of the focusing function with the focus position $\mathbf{x}_i'$ and $G^+(\mathbf{x}_i'|\mathbf{x}_0'', t)$ is the retrieved downgoing wavefield from a surface source at $\mathbf{x}_0''$.

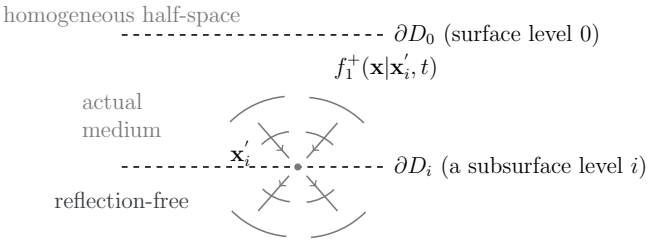

Figure 4.2: An illustration of the downgoing focusing wavefield $f_1^+(\mathbf{x}|\mathbf{x}_i', t)$. After being injected at the surface level ∂D_0 at $t = -t_d(\mathbf{x}_0|\mathbf{x}_i')$, it propagates downward and focuses at $\mathbf{x}_i'$ at $t = 0$. $t_d(\mathbf{x}|\mathbf{x}_i')$ is the direct travel time from $\mathbf{x}_0$ to $\mathbf{x}_i'$. Then the wavefield continues propagating downward from the level i. Notice that the medium below that level is defined as reflection-free, which is different from that in Fig. 4.1.

For $t \geq t_d(\mathbf{x}_0^{''}|\mathbf{x}_i^{'})$ (the direct travel time from a position $\mathbf{x}_i^{'}$ in the borehole to a position $\mathbf{x}_0^{''}$ at the surface), the up-down wavefields can be computed by

$$G^{-}(\mathbf{x}_i^{'}|\mathbf{x}_0^{''},t) = \int_{\partial D_0}\int_{-\infty}^{t} \mathcal{R}^{\cup}(\mathbf{x}_0^{''}|\mathbf{x}_0,t-t^{'})f_1^{+}(\mathbf{x}_0|\mathbf{x}_i^{'},t^{'})dt^{'}d\mathbf{x}_0 \tag{4.1}$$

and

$$G^{+}(\mathbf{x}_i^{'}|\mathbf{x}_0^{''},t) = f_{1,0}^{+}(\mathbf{x}_0^{''}|\mathbf{x}_i^{'},-t) - \int_{\partial D_0}\int_{-\infty}^{t} \mathcal{R}^{\cup}(\mathbf{x}_0^{''}|\mathbf{x}_0,t-t^{'})f_1^{-}(\mathbf{x}_0|\mathbf{x}_i^{'},-t^{'})dt^{'}d\mathbf{x}_0. \tag{4.2}$$

Here $\mathcal{R}^{\cup}(\mathbf{x}_0^{''}|\mathbf{x}_0,t)$ is the known surface reflection response, $f_1^{\pm}(\mathbf{x}_0|\mathbf{x}_i^{'},t)$ is the one-way focusing functions to be found by an iterative Marchenko scheme (which will be shown shortly), and the up-down wavefields are denoted as the band-limited Green's functions $G^{\pm}(\mathbf{x}_i^{'}|\mathbf{x}_0^{''},t)$. The notation of $f_{1,0}^{+}$ stands for the initial estimate of f_1^{+}.

In order to use these two equations, one needs to find the focusing functions $f_1^{\pm}(\mathbf{x}_0|\mathbf{x}_i^{'},t)$, of which the sum describes a pressure wavefield that satisfies the wave equation in the medium between ∂D_0 and ∂D_i and focuses at the focusing position $\mathbf{x}_i^{'}$ at $t = 0$. An illustration of its downgoing component is shown in Fig. 4.2.

These focusing functions $f_1^{\pm}(\mathbf{x}_0|\mathbf{x}_i^{'},t)$ are found by an iterative Marchenko scheme, starting with an initial estimate of $f_1^{+}(\mathbf{x}_0|\mathbf{x}_i^{'},t)$. More details on the Marchenko scheme and the focusing functions are explained in the reference literature (Rose, 2002; Broggini et al., 2012; Wapenaar et al., 2013; Slob et al., 2014). Here we summarise the scheme with Eq. 4.3 to 4.5, which read

$$f_{1,k}^{+}(\mathbf{x}_0^{''}|\mathbf{x}_i^{'},t) = f_{1,0}^{+}(\mathbf{x}_0^{''}|\mathbf{x}_i^{'},t)+\theta(t+t_d(\mathbf{x}_0^{''}|\mathbf{x}_i^{'}))\int_{\partial D_0}\int_{-\infty}^{\infty} \mathcal{R}^{\cup}(\mathbf{x}_0^{''}|\mathbf{x}_0^{'},t^{'})f_{1,k-1}^{-}(\mathbf{x}_0^{'}|\mathbf{x}_i^{'},t+t^{'})dt^{'}d\mathbf{x}_0^{'}, \tag{4.3}$$

$$f_{1,k}^{-}(\mathbf{x}_0^{''}|\mathbf{x}_i^{'},t) = \theta(t_d(\mathbf{x}_0^{''}|\mathbf{x}_i^{'})-t)\int_{\partial D_0}\int_{-\infty}^{\infty} \mathcal{R}^{\cup}(\mathbf{x}_0^{''}|\mathbf{x}_0^{'},t-t^{'})f_{1,k}^{+}(\mathbf{x}_0^{'}|\mathbf{x}_i^{'},t^{'})dt^{'}d\mathbf{x}_0^{'}, \tag{4.4}$$

with

$$f_{1,0}^{+}(\mathbf{x}_0^{''}|\mathbf{x}_i^{'},t) \approx G_d(\mathbf{x}_i^{'}|\mathbf{x}_0^{''},-t), \tag{4.5}$$

where $\theta(t)$ is the Heaviside function that passes the results for $t > 0$, and k is the number of iteration, starting from 0. First, by setting $k = 0$ in Eq. 4.5, one forms the first estimate of $f_{1,0}^{+}$ according to Eq. 4.4 by using the time-reversed direct wavefield from $\mathbf{x}_0$ to $\mathbf{x}_i^{'}$ in the borehole data as $G_d(\mathbf{x}_i^{'}|\mathbf{x}_0,-t)$. Then by setting $k = 1$, the first update $f_{1,1}^{+}$ can be computed from Eq. 4.3, and subsequently the upgoing component $f_{1,1}^{-}$ from Eq. 4.4. After repeating the procedure for a few iterations until a satisfactory $f_1^{\pm}$ is found, it can then be substituted back into Eq. 4.1 and 4.2 for the up-down wavefields. In this last step, again, only the surface reflection data and the direct wavefield travel times are needed. An overall processing flow chart is shown in Fig. 4.3.

In addition, for a more intuitive understanding of the retrieval of f_1^{+}, a simplified example of the overall data structure is shown in Fig. 4.4. In the figure, the solid grey dots denote

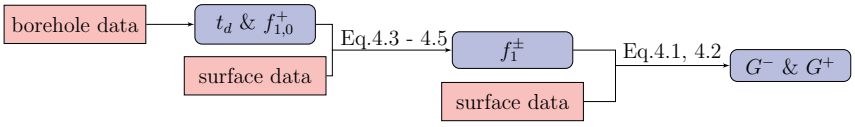

Figure 4.3: The general workflow for estimating the up-down wavefields in the horizontal borehole. The red boxes denote the input data, and the round-cornered purple boxes denote the computed results.

the three sources at the surface for both the surface and borehole data. The blue dot denotes a receiver in the borehole. Through the iterative Marchenko scheme, the focusing function that is emitted from those three surface source positions can be found. And subsequently, the downgoing wavefield G^+ (same with G^-) is retrieved. The number of sources in the retrieved up-down wavefields is the same as the number of sources in the surface reflection data.

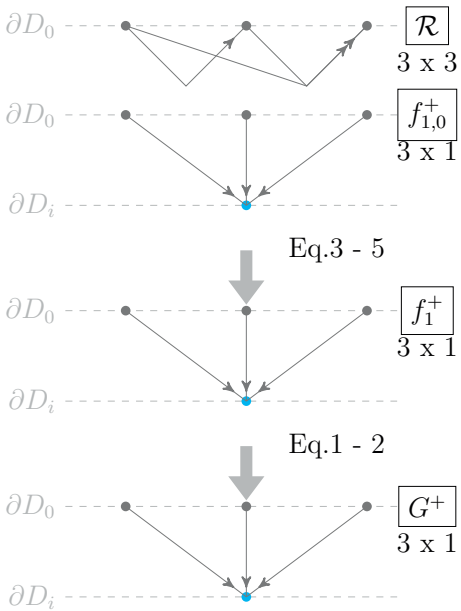

Figure 4.4: Illustration of the retrieval of f_1^+ and G^+ from the surface reflection response $\mathcal{R}$. The surface level is denoted by ∂D_0 and the focusing depth is denoted by ∂D_i. The numbers below the boxed quantities are the numbers of sources and receivers, so for example, 3 x 1 means 3 sources and 1 receiver. The configuration for the retrieved upgoing wavefield G^- is similar to the case of G^+, so it is not shown here.

4.3 Numerical results

The synthetic data are modelled using a realistic P-wave velocity model from the North Sea. To show that the method is not limited to any particular borehole orientation, three borehole geometries are tested, namely, the horizontal, the deviated and the vertical. Fig. 4.5 shows the model and the data geometries. In all three cases, there are 241 sources and receivers in the surface reflection data, with a source / receiver spacing of 25 m. A finite difference method (Thorbecke and Draganov, 2011) is used for modelling the synthetic acoustic pressure datasets (P). The source signal in the surface data is a band-limited delta function with a maximum frequency of 55 Hz. The free surface related multiples are not included in the modelling, which is an ideal scenario for the method. The source signal for the borehole data is a Ricker wavelet with a peak frequency of 15 Hz.

4.3.1 Horizontal borehole

For this horizontal borehole case, there are 129 receivers in the borehole of the depth 2.3 km, starting from $x_1 = 1000$ m to $x_1 = 4200$ m, with a spacing of 25 m, as shown in Fig. 4.5 a). The source positions for the borehole data are the same as in the surface data.

Two common-receiver gathers in the borehole are shown in Fig. 4.6. A preferable approach to form the initial estimate of the focusing wavefield is time windowing the direct wavefield, as this preserves the correct amplitude. In case the time windowing fails for far-offset data due to the head waves, etc., one can use a dip filter to remove those head waves before time windowing. Another workaround is to extract the travel time curves with the maximum amplitude and convolve it with a zero-phase wavelet. This, however, alters what should be the inverse of the direct wavefield, but the kinematic travel time is preserved, which is the most important for starting the iterative Marchenko scheme. In this horizontal borehole example, this less-than-ideal approach is tested to observe the effect on the result. Some local correction is made on the extracted maximum-amplitude curve to ensure a smooth curve. This correction is calculated based on the nearby slopes. Then together with the surface reflection data, the focusing wavefields $f^+_{1,0}$ is computed by using the iterative scheme (Eq. 4.3 - 4.5). Fig. 4.7 shows two examples of the obtained focusing wavefield f^+_1 at the surface, with the focusing position in the borehole at $x_1 = 1500$ m and $x_1 = 3000$ m. The up-down wavefields are then retrieved according to Eq. 4.1 and 4.2.

Fig. 4.8 is the common-source comparison of the retrieved up-down wavefields (in black) with those (in red) by an angle-dependent PZ summation method. In the figure, the events in the downgoing field after the direct arrivals are gained by a factor 8 for viewing. For this trace-by-trace comparison, an overall scaling factor is used, where the maximum amplitude in the retrieved downgoing wavefield is scaled with that in the measured borehole data. This does not alter the amplitude-versus-offset behaviour in the retrieved wavefields. The figure shows that the phases of the up-down wavefields are recovered by this method. The mismatch in amplitudes can be due to the following factors. One is that instead of

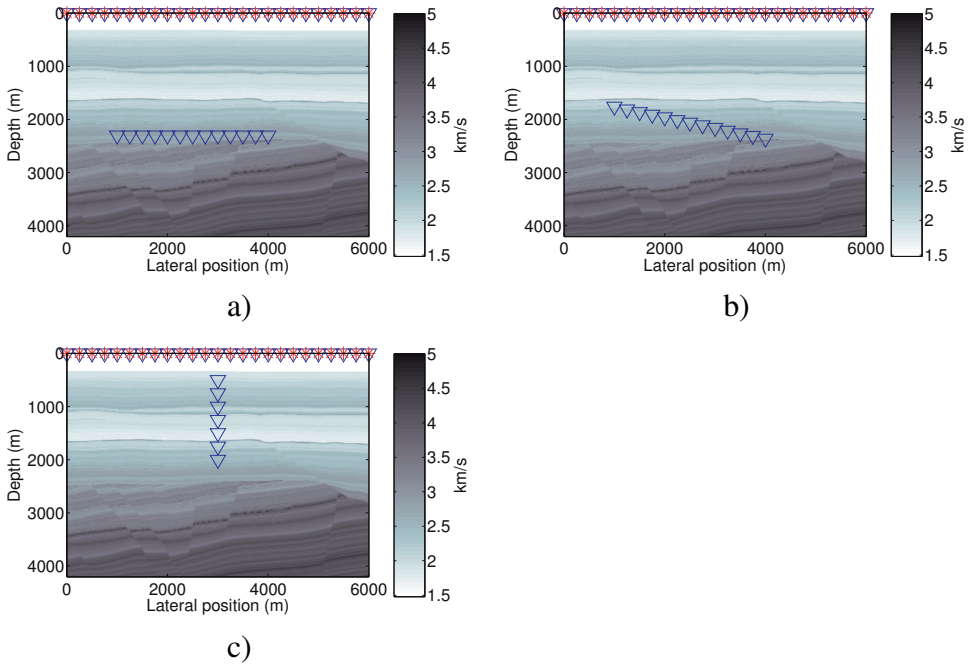

Figure 4.5: The P-wave velocity model and the acquisition geometries for the a) horizontal borehole, b) deviated borehole and c) vertical borehole. The stars denote the sources in both the surface and borehole data, and the triangles denote the receivers. The blue circles in a) denote the two receiver positions at 1.5 km and 3 km, for which the retrieved focusing wavefields are shown in Fig. 4.7.

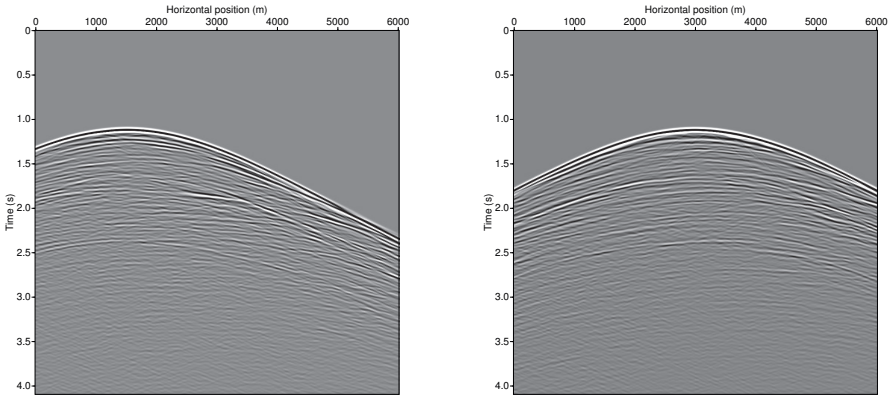

a) b)

Figure 4.6: The common-receiver data in the horizontal borehole. The receiver position is at a) 1.5 km and b) 3 km, as shown by the blue dots in Fig. 4.5 a).

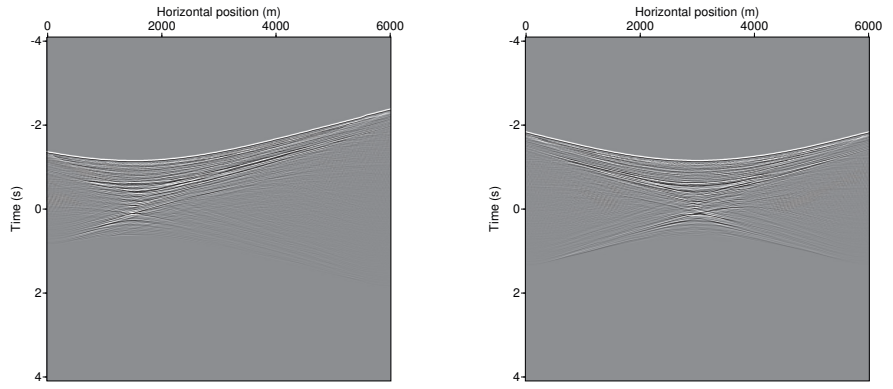

a) b)

Figure 4.7: The downgoing focusing wavefield f_1^+, found by the iterative Marchenko method. The focusing positions are at a lateral position of a) 1.5 km and b) 3 km in the borehole.

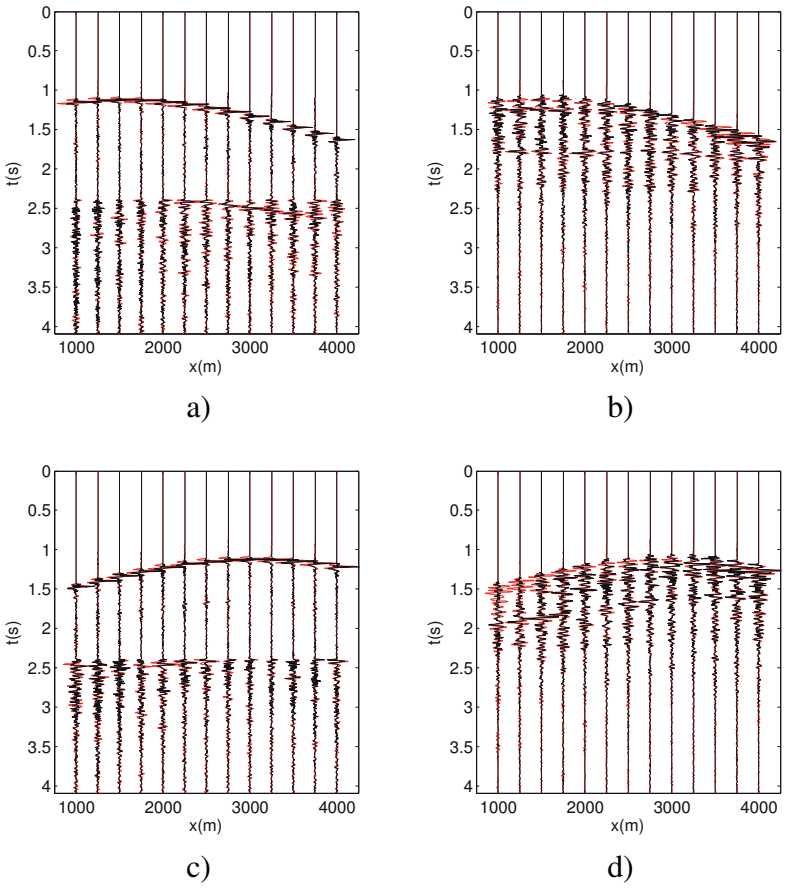

Figure 4.8: Horizontal borehole case. The common-source comparison of the retrieved up-down wavefields in the borehole in Fig. 4.5 a). The downgoing fields are shown in a) and c), and the upgoing in b) and d). The top row is for the common source (at the surface, not in the borehole) at 1.5 km and the bottom row is for the source at 3 km. The color black shows the results by this method, and the red color shows the results by an angle-dependent PZ summation method. The events after the direct arrivals in the downgoing field is scaled up by a factor of 8 for viewing. Every tenth trace is plotted.

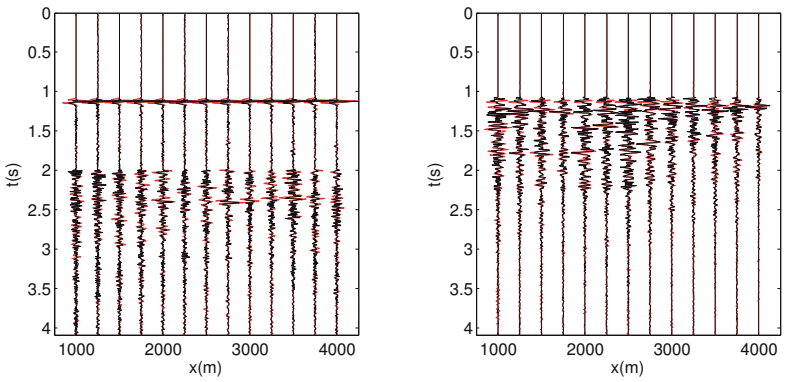

Figure 4.9: The comparison of zero-lateral-offset (the same lateral position, but vertically separated) traces of a) the downgoing and b) the upgoing wavefield. The same color scheme as Fig. 4.8 applies. The events after 2 s in the downgoing wavefield are scaled up by a factor of 8 for viewing. Every tenth trace is plotted.

time-windowing the direct arrivals in the borehole data, we used a synthetic direct wavefield, where mainly it is only the travel time that is preserved. The other factor is that there is a limited acquisition coverage on the surface compared to the largest offset in the borehole, seen in Fig. 4.5 a). For the far-offset, the source-receiver aperture in the borehole is wider for the nearby reflectors than in the surface data, therefore in order to capture some of the nearby reflectors at a far-offset in the borehole, the stationary position at the surface would be further far on the side of the model. Having a wide and complete surface reflection data is crucial for this method. Fig. 4.9 is the comparison for the zero-lateral-offset. Here the surface aperture is not the reason for the amplitude mismatch because it is a zero-lateral-offset. The reason for the amplitude mismatch should be the non-ideal initial estimate of the focusing function used for this test, as it alters what should be the inverse of the direct wavefield. For the next two examples, the time-windowed direct wavefield is used instead.

4.3.2 Deviated borehole

In the deviated borehole case, there are 129 receivers in the borehole. The lateral position of the borehole receivers is from $x_1 = 1000$ m to $x_1 = 4200$ m with a 25 m interval. The depth of the receivers is from $x_3 = 1760$ m to $x_3 = 2400$ m with a 5 m interval. The data geometry is shown in Fig. 4.5 b). Different from the previous case, the time-windowed direct arrivals in the borehole data is used to form the initial estimate of the focusing wavefield, where the amplitude of the focusing wavefield is better represented. The trace-

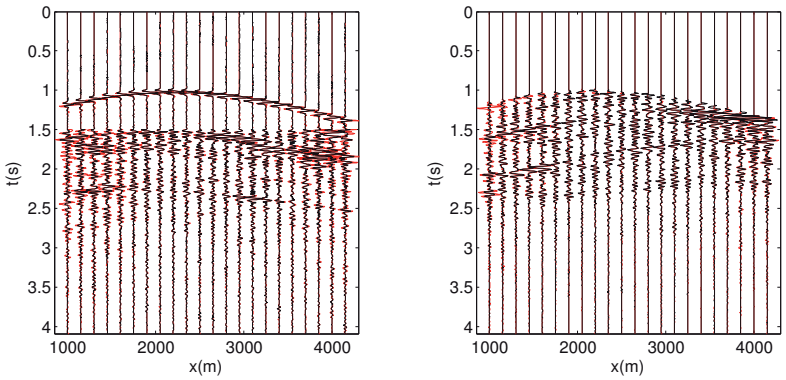

Figure 4.10: Deviated borehole case. The common-source comparison of the retrieved up-down wavefields in the borehole in Fig. 4.5 b). The source position is at 2500 m at the surface. a) The downgoing and b) the upgoing wavefields. The same color scheme as Fig. 4.8 applies. The events after 1.5 s in the downgoing waves are scaled up by a factor of 8 for viewing. Every sixth trace is plotted.

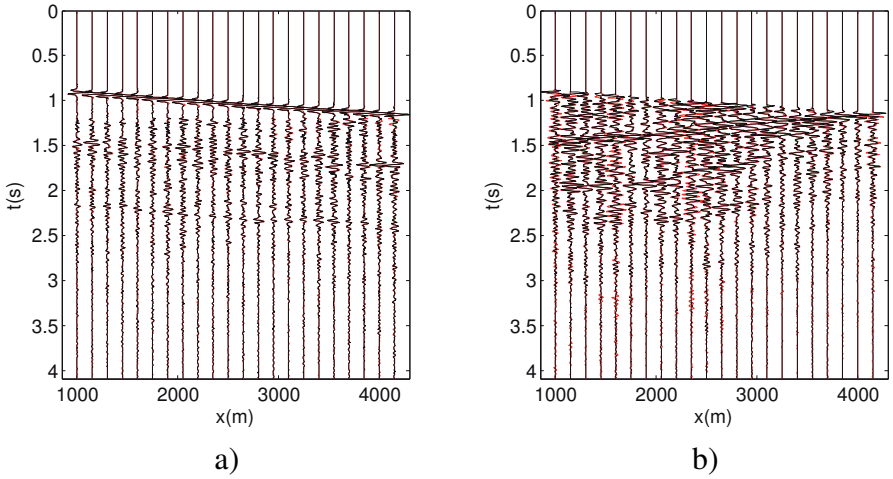

Figure 4.11: The comparison of zero-lateral-offset traces of a) the downgoing and b) the upgoing wavefields. The same color scheme as Fig. 4.8 applies. The events after 1.2 s in the downgoing waves are scaled up by a factor of 8 for viewing. Every sixth trace is plotted.

by-trace comparison with those by a standard multi-component method (angle-dependent PZ summation) is shown in Fig. 4.10. Again, the slight discrepancy is seen in terms of amplitude mismatch for the far-offset. The reason is suspected to be the limited source-receiver aperture in the surface data as mentioned for the horizontal borehole case. The zero-lateral-offset comparison (Fig. 4.11) is however improved as expected, as a more accurate initial estimate of the focusing wavefield is used.

4.3.3 Vertical borehole

The third example is a standard VSP configuration with 69 receivers in a vertical borehole at $x_1 = 3000$ m. The depth of the receivers is from $x_3 = 500$ m to $x_3 = 1200$ m with a 25 m interval, as shown in Fig. 4.5 c). The same time-windowing approach is used in forming the initial estimate of the focusing wavefield. In the trace comparison, Fig. 4.12, a common FK dip filtering method is added as it is a standard technique for VSPs and it also only requires single-component data, similar as this method. The figure shows the retrieved up-down wavefields for a common source at $x_1 = 3000$ m at the surface. The results are compared with those by the PZ summation approach (in red) in a) and b) and those by f-k dip filtering (in red) in c) and d). Overall, by taking into account the extra gain applied in the downgoing wavefield, there is no significant mismatch in phase and amplitude for the retrieved results.

4.4 Discussion

The up-down separation of borehole data is a routine process and there are many mature techniques available. Nevertheless, there are several aspects of the proposed method worth to be mentioned. First, it is a wave-equation based method and is valid for a general lossless inhomogeneous medium, not limited to a horizontally layered medium. And as it is wave-equation based, all internal multiples are taken into account. Second, no medium parameter is needed, including the velocity or density at the borehole location, so it is a completely data-driven method. The general Marchenko method requires a smooth background velocity model, but since the direct wavefield travel times are measured in the borehole data, this circumvent the need for any velocity information. Third, this method does not require a receiver array. It can be applied independently per single borehole receiver, as long as a full set of surface reflection responses is available. And as a result of that,the method works the same for any borehole orientation as shown in the numerical examples. Fourth, only single-component data from the surface and the borehole are needed, and they don't need to be acquired simultaneously, as long as no significant subsurface changes occur in the overburden in between. In that case the focusing functions do not change, but they can be used to monitor a changing reservoir below the decomposition level. This means it could be potentially used for reservoir monitoring where the surface data are already available. Reverse VSP data can also be used by reciprocity.

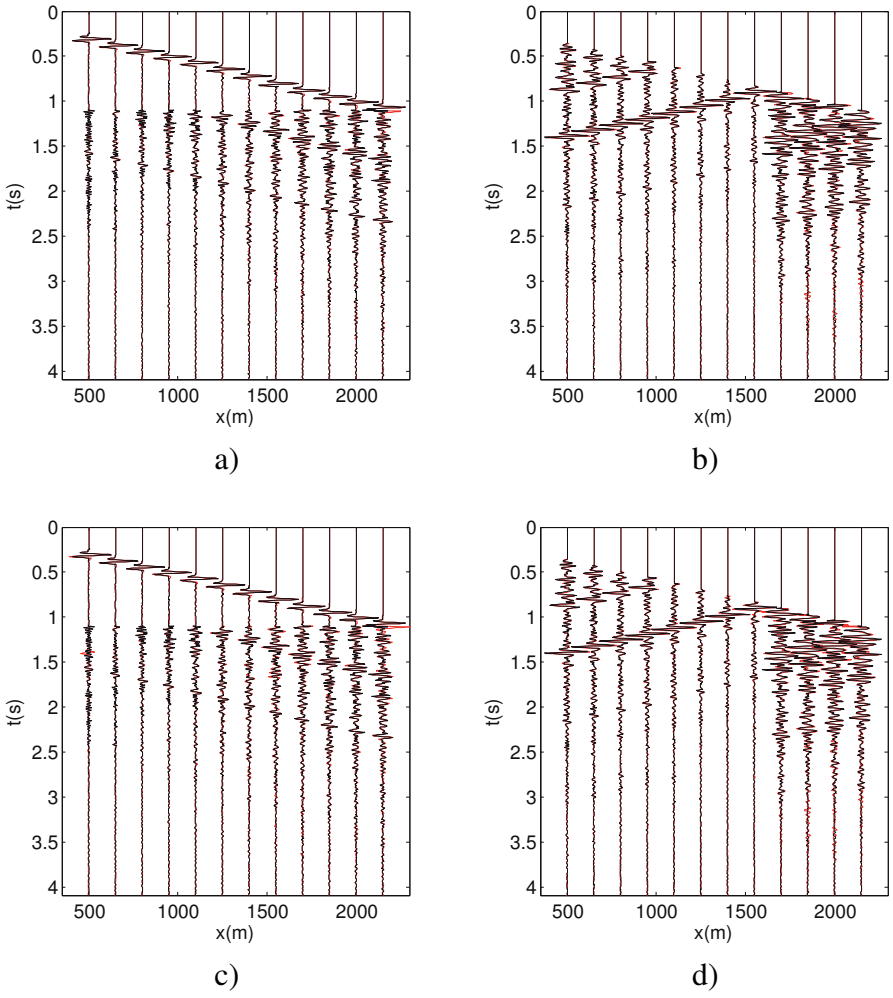

Figure 4.12: Vertical borehole case. The comparison of the retrieved up-down wavefields of a common source at $x_1 = 3000$ m in Fig. 4.5 c). a) & b) are the trace-by-trace view of the downgoing and the upgoing fields, respectively. The results by this method are in black, and those by PZ summation are in red. c) & d) are a similar comparison against those by f-k dip filtering, drawn in red. An amplitude gain of a factor of 8 is applied on the events after the direct arrivals in the downgoing wavefield. Every sixth trace is plotted.

The horizontal borehole example shows that the method retrieves the phase of the wavefield reasonably well, even when it is only the direct travel time that is used (instead of the time-windowed direct wavefield). The amplitude match improves as shown in the zero-lateral-offset comparison for the deviated (Fig. 4.11) and the vertical case (Fig. 4.12) where the time-windowed direct wavefield is used.

Nevertheless, there are a few problems to be considered for field application. First, a good surface reflection response is important, as the up-down wavefields are essentially retrieved from the surface data. For the scheme presented in this paper, this means it requires a good source signal deconvolution and surface multiple removal for the surface data. For field data, a perfect source signal deconvolution requirement is rarely met and its solution requires further research on its own. For the problem of the surface multiples, the scheme could be adapted based on the approach shown by Singh et al. (2017). Second, given a certain maximum offset in the surface data, the illumination angles to steep reflectors are limited, which is smaller than the same offset in the borehole. As a result, the retrieved up-down fields may miss certain events with steep angles, but it can be helped by acquiring surface data with large offset. When the offset is not sufficiently large, some inaccurate retrieval of the phase and amplitude in the up-down wavefields occurs. Third, attenuation is not considered in this study, but it is also possible to be included as shown by Slob et al. (2016).

The potential application range for this method could be any single-component subsurface receiver (or source in case of Reverse VSP), where a full set of surface reflection responses is available. In particular, the direct arrivals in borehole DAS (Distributed Acoustic Sensing) recording should be considered, as it is essentially single-component and low-cost for installing in a wide range of boreholes. The proposed method could potentially be an up-down separation solution for DAS data (Farhadiroushan et al., 2009; Daley et al., 2013; Madsen et al., 2013) which does not have any requirement regarding the well geometry or the subsurface information.

4.5 Conclusion

We show a new approach to retrieve the up-down wavefields in boreholes using surface reflection responses. The method requires only the acoustic pressure measured at the surface and in the borehole. No medium parameters are needed, and it is applicable to any borehole geometry even with a single receiver, as long as a full set of surface reflection response is available. The numerical experiment shows satisfactory results compared to those by standard separation methods, given both the ideal and non-ideal initial estimate of the focusing wavefield. Although practical issues remain for field application, we believe that the potential benefits and application range of this new approach is worth noticing. In particular, the future combined use with the DAS technology might be of significant interest for economical large scale monitoring projects.

4.6 Acknowledgements

We like to acknowledge the sponsors to the ROSE consortium at NTNU, Jan Thorbecke at TUD for the Open Source modelling package, and Alexander Kritski at Statoil for the velocity model. We thank the reviewers and associate editors for their constructive comments.

Chapter 5

A new approach to separate seismic time-lapse time shifts in the reservoir and overburden

Yi Liu[1], Martin Landrø[1], Børge Arntsen[1], Joost van der Neut[2], Kees Wapenaar[2]

[1]Norwegian University of Science and Technology
[2]Delft University of Technology

Published in *Geophysics*, 82 (6): Q67-Q78

Abstract

For a robust way of estimating time shifts near horizontal boreholes, we present a method for separating the reflection responses above and below a horizontal borehole. Together with the surface reflection data, the method uses the direct arrivals from borehole data in the Marchenko method. The first step is to retrieve the focusing functions and the up-down wavefields at the borehole level using an iterative Marchenko scheme. The second step is to solve two linear equations using a least squares minimizing method for the two desired reflection responses. Then the time shifts that are directly linked to the changes on either side of the borehole are calculated using a standard cross correlation technique. The method is applied with good results to synthetic 2D pressure data from the North Sea. One example uses purely artificial velocity changes (negative above the borehole and positive below), and the other uses more realistic changes based on well logs. In the 2D case with an adequate survey coverage at the surface, the method is completely data-driven. In the 3D case where there is a limited number of horizontal wells, a kinematic correct

velocity model is needed, but only for the volume between the surface and the borehole. Possible error factors related to the Marchenko scheme, such as an inaccurate source wavelet, imperfect surface multiples removal, medium with loss, etc. are not included in this study.

5.1 Introduction

Seismic time-lapse analysis has become a standard tool for subsurface monitoring in the petroleum industry. By studying the difference in the data from repeated seismic surveys, useful information of the field can be obtained, such as velocity, pressure and saturation changes. One of the first commercial successes of time-lapse seismic in the North Sea is the Gullfaks study (Landrø et al., 1999), where the evident effect of replacing oil with water in the seismic data helps the successful identification of remaining and untouched oil pockets.

The changes between the repeated surveys can be explored in many ways. One common technique is to find and analyze the time shift, and this is the main subject of this paper. Other methods such as waveform inversion that takes into account both traveltime and amplitude to estimate changes of elastic properties are also used (Raknes and Arntsen, 2014; Maharramov et al., 2015, 2016). Some issues related to survey repeatability can be addressed with those methods. Here we focus on the traveltime shift estimation as they remain a main tool for time-lapse studies and can be linked to physical strain and velocity changes (Landrø and Stammeijer, 2004), for example, reservoir compaction (Røste et al., 2015). Barkved and Kristiansen (2005) show a field example of how compaction in a reservoir can be observed in time-lapse seismic data. Røste et al. (2007) use the observed time shifts in pre-stack ocean bottom cable (OBC) data to discriminate layer thickness and velocity changes. For anisotropic media, Fuck et al. (2009) give an analytical description of stress-related traveltime shifts and show anisotropy parameters can be estimated based on the offset dependence of time shifts.

Both surface reflection data (Meunier and Huguet, 1998) and borehole data (Meunier et al., 2001; Guilbot and Smith, 2002) are used for time-lapse studies. To calculate the time shifts, the standard procedure is by crosscorrelation (Hatchell and Bourne, 2005). Other more advanced methods such as nonlinear inversion (Rickett et al., 2007) and Correlated Leakage method have also been proposed and comparisons are made (Whitcombe et al., 2010). However, as traveltime changes are cumulative along the raypaths and the sources are usually placed close to the surface, the changes in the deep area cannot be directly linked to the observed time shifts. In addition, strong multiple reflections in the data may hinder the event picking, and eventually making the time shift estimation difficult, especially for deep sections.

For the problem of the accumulative traveltime, the use of fractional change of time shift (also called time strain) (Rickett et al., 2007) has been proposed, but one disadvantage is that the differentiation tends to boost noise. An example of using time strain for es-

timation of reservoir pressure changes is shown by Hodgson et al. (2007). On the other hand, methods related to seismic interferometry (Snieder et al., 2009; Wapenaar et al., 2011; Galetti and Curtis, 2012) can be used to virtually move surface sources below a complex overburden, and therefore enable time-lapse monitoring of reservoir without any velocities of the overburden (Bakulin and Calvert, 2006). Mehta et al. (2008) improve the method by using multi-component data to remove the spurious events related to the reflections in the overburden from retrieved responses.

For the attenuation of internal multiples, a classical approach is building a multiple model and adaptively subtracting it from the data by computing shaping filters (Guitton and Verschuur, 2004). Another approach is using multi-component data for up-down separation (Amundsen, 2001). Given single-component data and a smooth background velocity model, a new focusing method that goes beyond interferometry, called the Marchenko method (Broggini et al., 2012; Wapenaar et al., 2013; Behura et al., 2014; Wapenaar et al., 2016) meets the requirement of effectively removing internal multiples. The method enables one to create virtual sources at any position inside a medium, but a macro-velocity model that describes the kinematics of the wavefield is nevertheless necessary. Examples of its application for internal multiple removal are shown by Meles et al. (2015); Ravasi et al. (2016). However, velocity errors in the model affect the method to various degrees (Thorbecke et al., 2013; de Ridder et al., 2016). For the method's application for robust imaging near horizontal boreholes, Liu et al. (2016b) propose the combination of surface reflection data and horizontal borehole data to replace the dependency on a background velocity model. Two separate reflection responses can be obtained, one for the overburden and one for the underburden (the area below a horizontal borehole, including the reservoir). All internal multiples from the other side of the borehole are removed, and imaging with good positioning of the reflectors near the borehole can be obtained with crude velocities.

In this paper we show that it is possible to address both of the above problems by combining the surface and borehole data. By repeating two of the proposed schemes in Liu et al. (2016b) on the base and monitor data, the time shifts in the overburden and the underburden can be separated and subtle time shifts near the horizontal borehole can be estimated without any event picking on the data. Then standard time shift analysis can be performed for each side of the borehole independently. It offers the same benefits as Bakulin and Calvert (2006), but also address changes above the borehole. In addition, the internal multiples can be taken into account without using multi-component data, and a velocity model is not needed.

We first explain the pre-processing sequence, followed by the numerical demonstration based on two field velocity models. A velocity change that is purely negative in the overburden and positive in the underburden is used in the first example. A more realistic velocity change model based on the Gullfaks field is used in the second example, and the results are compared with field observations. We then discuss the benefits and limitations of the method.

5.2 Method

In this section, besides the conventional surface seismic data geometry, we assume the borehole data are available at a constant depth (e.g. from a horizontal well) with sources at the surface. The word underburden is used to refer to the medium that is below the borehole (including the reservoir). Although the method is presented with a configuration of a horizontal borehole, the application can be extended to deviated wells and it will be discussed in a later section. The free-surface multiples removal and the source signal deconvolution are assumed in the surface reflection data. The data are denoted as measured band-limited Green's functions in the equations.

The aim of the pre-processing is to use a data-driven method to reconstruct the reflection responses of the overburden and the underburden, individually, at a constant (borehole) level. The notation convention used throughout the paper is that a spatial position is denoted by $\mathbf{x} = (x_1, x_2, x_3)$, with $x_3 = 0$ at the surface, ∂D_0, and x_3 is increasing positively downward. Coordinates at any boundary, e.g. at the depth level ∂D_i (which indicates the horizontal borehole depth level in this paper), are denoted as $\mathbf{x}_i = (\mathbf{x}_H, x_{3,i})$, with $\mathbf{x}_H = (x_1, x_2)$. Position $\mathbf{x}_i^{'}$ represents a focusing position at a lateral coordinate $\mathbf{x}_H^{'}$ at the depth level ∂D_i, and $\mathbf{x}_0^{''}$ represents a position at lateral coordinate $\mathbf{x}_H^{''}$ at the surface level ∂D_0. This notation convention is summarized in Fig. 5.1. In the figure, the two blue solid lines show examples of the ray paths of the two unknown reflection responses to be solved. The reflection response $\mathcal{R}^{\cap}(\mathbf{x}_i^{'}|\mathbf{x}_i, t)$ is the response of the overburden and contains no interaction with the part of the medium below the borehole, whereas $\mathcal{R}^{\cup}(\mathbf{x}_i^{'}|\mathbf{x}_i, t)$ is that of the underburden and contains no interaction with the part of the medium above the borehole. The surface reflection response $\mathcal{R}^{\cup}(\mathbf{x}_0^{''}|\mathbf{x}_0, t)$ is known from the surface data, indicated by the red solid line in the figure. Bold faced variables indicate vectors.

5.2.1 Reconstruction of the reflection responses

The two unknown reflection responses (the blue quantities in Fig. 5.1) can be found by solving the following two equations in the frequency domain (Wapenaar et al., 2014),

$$\hat{f}_2^{+}(\mathbf{x}_i^{'}|\mathbf{x}_0^{''}) = \int_{\partial D_i} \hat{\mathcal{R}}^{\cap}(\mathbf{x}_i^{'}|\mathbf{x}_i)\hat{f}_2^{-}(\mathbf{x}_i|\mathbf{x}_0^{''})d\mathbf{x}_i; \tag{5.1}$$

$$\hat{G}^{-}(\mathbf{x}_i^{'}|\mathbf{x}_0^{''}) = \int_{\partial D_i} \hat{\mathcal{R}}^{\cup}(\mathbf{x}_i^{'}|\mathbf{x}_i)\hat{G}^{+}(\mathbf{x}_i|\mathbf{x}_0^{''})d\mathbf{x}_i. \tag{5.2}$$

The symbol $\hat{}$ above quantities denotes the frequency domain, and the superscript * denotes complex conjugation. Here the first equation relates the unknown reflection response of the overburden $\hat{\mathcal{R}}^{\cap}(\mathbf{x}_i^{'}|\mathbf{x}_i)$ to pressure-normalized one-way focusing functions, $\hat{f}_2^{\pm}(\mathbf{x}_i^{'}|\mathbf{x}_0^{''})$, and the second equation relates the unknown reflection response of the underburden $\hat{\mathcal{R}}^{\cup}(\mathbf{x}_i^{'}|\mathbf{x}_i)$ to the up- and downgoing wavefields ($\hat{G}^{-}(\mathbf{x}_i^{'}|\mathbf{x}_0^{''})$ and $\hat{G}^{+}(\mathbf{x}_i^{'}|\mathbf{x}_0^{''})$) at $\mathbf{x}_i^{'}$ from a surface source at $\mathbf{x}_0^{''}$.

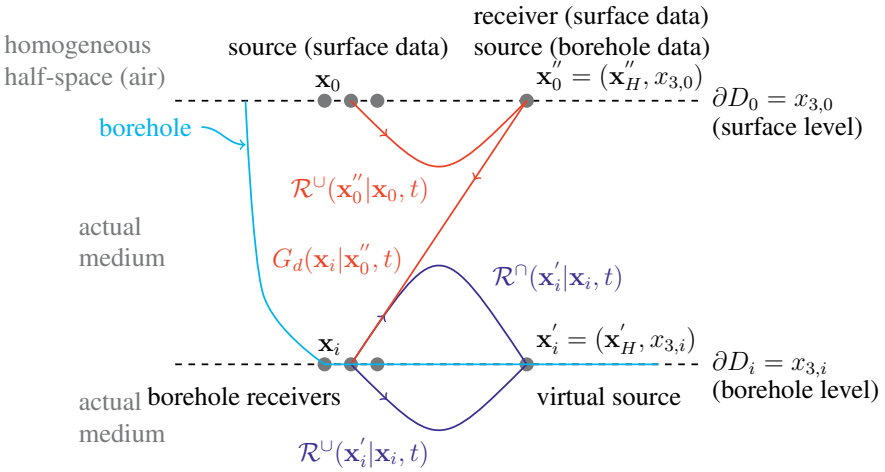

Figure 5.1: Notation convention and the coordinate definition. Each spatial position is denoted by $(\mathbf{x}_H, x_{3,i})$, with $\mathbf{x}_H = (x_1, x_2)$, and i represents a certain depth level. Here ∂D_0 denotes a transparent surface level, above which the medium is homogeneous, and ∂D_i denotes a horizontal borehole level. The blue solid lines represent the unknown reflection responses, where $\mathcal{R}^{\cup}(\mathbf{x}_i'|\mathbf{x}_i, t)$ contains *only* reflections coming from below the borehole and $\mathcal{R}^{\cap}(\mathbf{x}_i'|\mathbf{x}_i, t)$ contains *only* reflections coming from above the borehole. These two responses are the unknown responses to be solved. The red solid line represents the known surface reflection response.

A central element in the Marchenko method is formed by the focusing functions, and there are two types of them, $f_1^{\pm}(\mathbf{x}_0^{''}|\mathbf{x}_i^{'},t)$ and $f_2^{\pm}(\mathbf{x}_i^{'}|\mathbf{x}_0^{''},t)$. As the details can be found in many previous publications, we skip a complete introduction on this. Briefly speaking, the focusing functions satisfy the 3D wave equation with specific boundary conditions and are mutually related via

$$f_1^{+}(\mathbf{x}_0^{''}|\mathbf{x}_i^{'},t) = f_2^{-}(\mathbf{x}_i^{'}|\mathbf{x}_0^{''},t); \tag{5.3}$$

$$-f_1^{-}(\mathbf{x}_0^{''}|\mathbf{x}_i^{'},-t) = f_2^{+}(\mathbf{x}_i^{'}|\mathbf{x}_0^{''},t). \tag{5.4}$$

By using these mutual relations, Eq. 5.1 can be expressed using only $\hat{f}_1^{\pm}(\mathbf{x}_0^{''}|\mathbf{x}_i^{'})$. But in order to keep the clarity that the left hand side of Eq. 5.1 is a downgoing wave, both focusing functions are kept in this paper. All the necessary quantities needed to solve Eq. 5.1 and 5.2 can be found by computing the focusing function $f_1^{\pm}(\mathbf{x}_0^{''}|\mathbf{x}_i^{'},t)$.

Here we use an iterative Marchenko scheme (Wapenaar et al., 2013) to find $f_1^{+}(\mathbf{x}_0^{''}|\mathbf{x}_i^{'},t)$ and $f_1^{-}(\mathbf{x}_0^{''}|\mathbf{x}_i^{'},t)$ using the reflection response measured at the surface ∂D_0 and the direct wavefield measured in the borehole. The iterative scheme reads,

$$f_{1,k}^{+}(\mathbf{x}_0^{''}|\mathbf{x}_i^{'},t) = f_{1,0}^{+}(\mathbf{x}_0^{''}|\mathbf{x}_i^{'},t)+\theta(t+t_d(\mathbf{x}_0^{''}|\mathbf{x}_i^{'}))\int_{\partial D_0}\int_{-\infty}^{\infty}\mathcal{R}^{\cup}(\mathbf{x}_0^{''}|\mathbf{x}_0^{'},t^{'})f_{1,k-1}^{-}(\mathbf{x}_0^{'}|\mathbf{x}_i^{'},t+t^{'})dt^{'}d\mathbf{x}_0^{'}, \tag{5.5}$$

$$f_{1,k}^{-}(\mathbf{x}_0^{''}|\mathbf{x}_i^{'},t) = \theta(t_d(\mathbf{x}_0^{''}|\mathbf{x}_i^{'})-t)\int_{\partial D_0}\int_{-\infty}^{\infty}\mathcal{R}^{\cup}(\mathbf{x}_0^{''}|\mathbf{x}_0^{'},t-t^{'})f_{1,k}^{+}(\mathbf{x}_0^{'}|\mathbf{x}_i^{'},t^{'})dt^{'}d\mathbf{x}_0^{'}, \tag{5.6}$$

with

$$f_{1,0}^{+}(\mathbf{x}_0^{''}|\mathbf{x}_i^{'},t) \approx G_d(\mathbf{x}_i^{'}|\mathbf{x}_0^{''},-t), \tag{5.7}$$

where $\theta(t)$ is the Heaviside function that passes the results for $t > 0$. The subscript $_0$ indicates the initial estimate, which is approximated by the time-reversed direct wavefield $G_d(\mathbf{x}_i^{'}|\mathbf{x}_0^{''},-t)$ measured in the borehole. This is more accurate than to obtain $G_d(\mathbf{x}_i^{'}|\mathbf{x}_0^{''},-t)$ from a velocity model. As it is actually measured, subtle time shifts in the overburden are taken into account, even if they are not known. The notation here is changed to the time domain due to the time window function used. For our application, this "direct first" assumption is satisfied because the receiver spacing in the borehole data is not large and the medium varies smoothly. To extract the direct wavefield, a time gate can be used for small offsets. For large offsets, the direct arrivals intersect the refracted events, dip filtering or the picking of the traveltime curve with the maximum amplitudes can be used. Then together with the input of the surface reflection response $\mathcal{R}^{\cup}(\mathbf{x}_0^{''}|\mathbf{x}_0,t)$ and the traveltime $t_d(\mathbf{x}_i^{'}|\mathbf{x}_0^{''})$ (from the borehole data), $f_1^{\pm}(\mathbf{x}_0|\mathbf{x}_i^{'},t)$ can be computed without any velocity information.

Now with $f_1^{\pm}(\mathbf{x}_0|\mathbf{x}_i^{'},t)$ known, so are the up- and downgoing part of $f_2(\mathbf{x}_i^{'}|\mathbf{x}_0,t)$ by the mutual relation in Eq. 5.3 and 5.4. Then the reflection response of the overburden $\hat{\mathcal{R}}^{\cap}(\mathbf{x}_i^{'}|\mathbf{x}_i)$ in Eq. 5.1 can be solved for each frequency using, for instance a standard damped-least squares approach (Menke, 1989). To solve for the reflection response of the underburden $\hat{\mathcal{R}}^{\cup}(\mathbf{x}_i^{'}|\mathbf{x}_i)$ in Eq. 5.2, an extra step of computing the up- and downgoing wavefields ($G^{-}(\mathbf{x}_i^{'}|\mathbf{x}_0^{''},t)$ and $G^{+}(\mathbf{x}_i^{'}|\mathbf{x}_0^{''},t)$, respectively) is needed. They are related

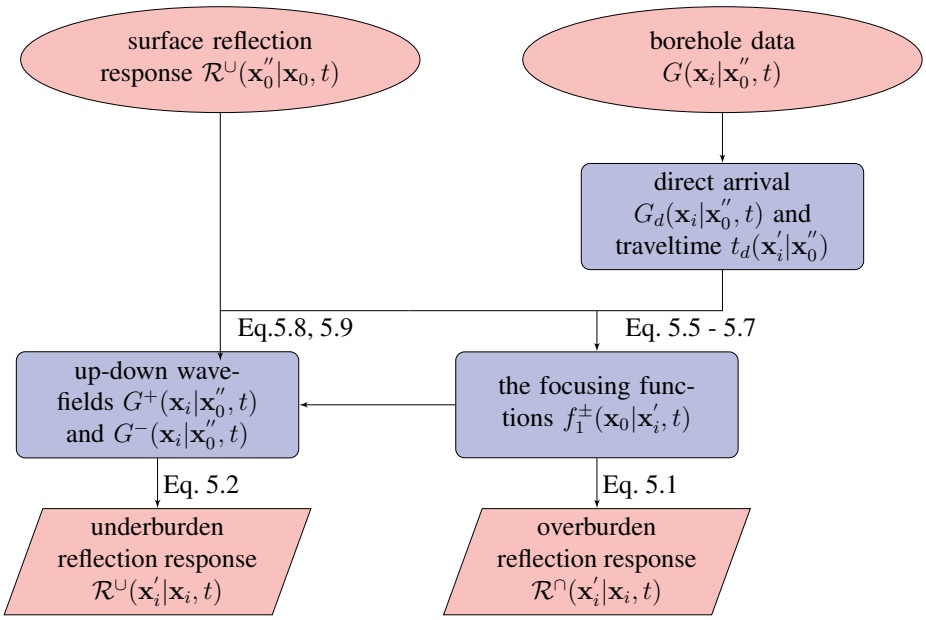

Figure 5.2: Flow chart illustration of the method. The ellipses denote the input and the trapezia denote the output. The intermediate steps are marked with the boxes.

to the focusing function and the surface reflection response via the following equations (Wapenaar et al., 2014), as long as $t \geq t_d(\mathbf{x}_i^{'}|\mathbf{x}_0^{''})$,

$$G^{-}(\mathbf{x}_i^{'}|\mathbf{x}_0^{''},t) = \int_{\partial D_0}\int_{-\infty}^{t} \mathcal{R}^{\cup}(\mathbf{x}_0^{''}|\mathbf{x}_0,t-t^{'})f_1^{+}(\mathbf{x}_0|\mathbf{x}_i^{'},t^{'})dt^{'}d\mathbf{x}_0 \tag{5.8}$$

and

$$G^{+}(\mathbf{x}_i^{'}|\mathbf{x}_0^{''},t) = f_{1,0}^{+}(\mathbf{x}_0^{''}|\mathbf{x}_i^{'},-t) - \int_{\partial D_0}\int_{-\infty}^{t} \mathcal{R}^{\cup}(\mathbf{x}_0^{''}|\mathbf{x}_0,t-t^{'})f_1^{-}(\mathbf{x}_0|\mathbf{x}_i^{'},-t^{'})dt^{'}d\mathbf{x}_0, \tag{5.9}$$

where $\mathcal{R}^{\cup}(\mathbf{x}_0^{''}|\mathbf{x}_0,t)$ (the surface reflection response), $f_1^{\pm}(\mathbf{x}_0|\mathbf{x}_i^{'},t)$ (the one-way focusing functions) and $t_d(\mathbf{x}_i^{'}|\mathbf{x}_0^{''})$ (the direct arrival's traveltime in the borehole data) are already known. After this step, $\hat{\mathcal{R}}^{\cup}(\mathbf{x}_i^{'}|\mathbf{x}_i)$ can be solved for in Eq. 5.2 in a similar manner as Eq. 5.1.

The overall workflow is summarized in Fig. 5.2. This workflow is repeated for the base and monitor data and results in two new separate datasets for time shift estimation, one for the underburden and one for the overburden.

The understanding of the method might also be helped by Fig. 5.3. The red quantities in the Fig. 5.3a indicate the input surface reflection response and the direct wavefield measured in the borehole. The method aims to find the blue quantities in Fig. 5.3b and 5.3c.

These new reflection responses are particularly useful for time-lapse traveltime analysis of the area near the borehole, complementing that from the original surface and borehole data. Both the sources and the receivers in these virtual responses are virtually moved to the borehole position, so the traveltime accumulates away from the borehole level. As the distance to the target is shorter, the observed time shifts can be more directly related to changes in the vicinity of the borehole without any prior information of the shallower section. Furthermore, there are no reflections coming from the other side of the borehole, improving the overall signal-to-noise ratio.

5.2.2 Time shift estimation

To estimate the time shift, a standard cross correlation technique is used in this paper. No event picking is performed prior to the cross correlation to show that the accurate time shift characterization near the borehole can be achieved automatically with this approach.

Depending on the magnitude of the time shift, it might be necessary to interpolate the new responses to a smaller time interval first, and a suitable time window is used for cross correlation. A certain minimum threshold value is chosen based on the cross correlation amplitude value for picking the time lag. Repeating the cross correlation for all receiver positions gives the overall time shift maps. The time strain maps can be calculated by taking the fractional difference of the time shift. The calculated time shift and the time strain maps of the overburden and the underburden are independent from each other, and more analysis linking the result to the geomechanical changes follows.

5.3 Numerical examples

5.3.1 Vankeulen model

The first example is based on the Vankeulen field in the North Sea, which is shown in Fig. 5.3a. For the surface data, there are 241 sources and receivers at the free surface. For the borehole data, there are 241 sources at the free surface and 161 receivers at a depth of 1300 m. Both the source and receiver spacings are 25 m. The source signal in the borehole data is a Ricker wavelet with a peak frequency of 15 Hz, and that in the surface data has a flat spectrum up to 48 Hz. A finite difference method (Thorbecke and Draganov, 2011) is used for modeling, and the surface related multiples are not included. For the monitor model, artificial velocity changes are made (Fig. 5.3d), where there is a maximum velocity increase of 30 m/s below the borehole and a maximum velocity decrease of 6 m/s occurs above the borehole. With these velocity changes, it is expected to observe only positive time shifts in the overburden and only negative time shifts in the underburden from the new responses.

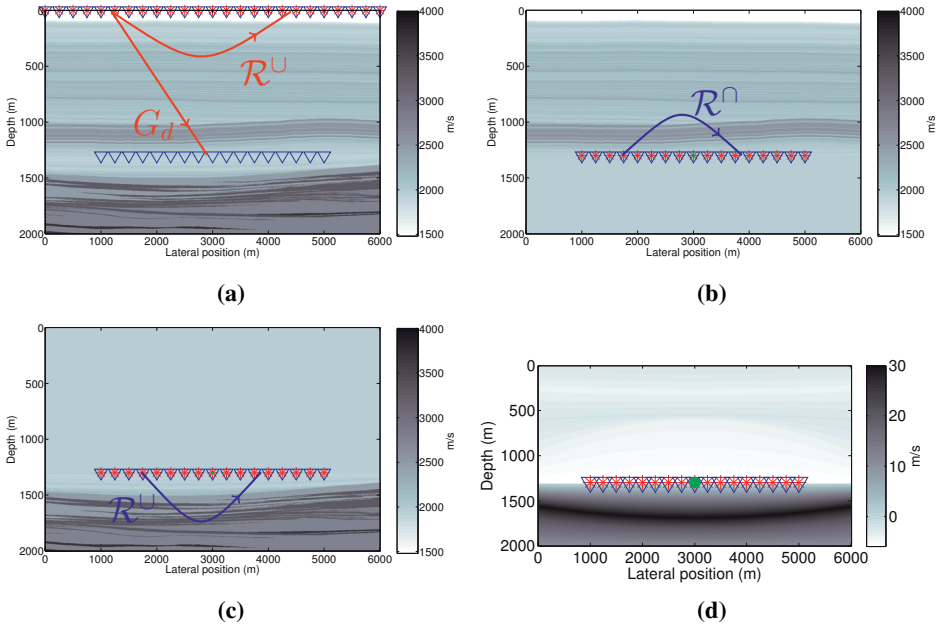

Figure 5.3: P-wave velocity model and the datasets geometries. The stars denote sources and the triangles denote receivers. The red letters denote the input data and the blue letters denote the unknown responses. a) The base velocity model. The configuration shows two survey geometries. The surface data have sources and receivers at the surface level, and the borehole data have sources at the surface and receivers in the borehole. b) The medium configuration in which the responses of the overburden are constructed. The sources are virtually moved to the borehole level, and because the underburden is homogeneous, there are no upgoing reflections in the new responses. c) Same as b) but for the underburden. d) The velocity change. The changes are artificial for the testing purpose. There is a velocity increase of up to 30 m/s below the borehole and a velocity decrease of up to 6 m/s above the borehole, such that positive time shifts (monitor − base) should be observed for the overburden and negative time shifts for the underburden. The green circle shows one reference new source location.

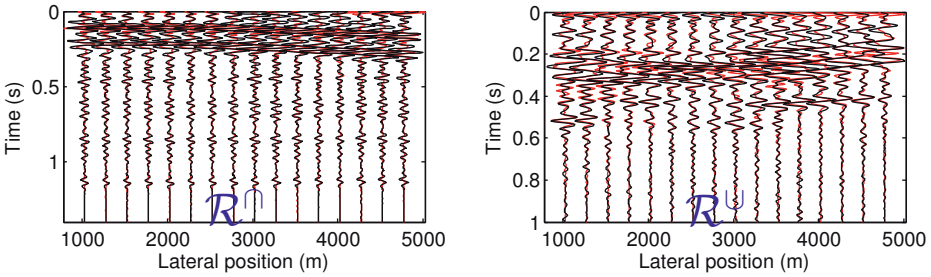

Figure 5.4: The zero-offset trace comparison with the modeled reference traces. The new response is in red and the reference in black. In these new responses, the sources are virtually moved to the borehole level and the receiver positions are the same as in the original borehole survey, as shown in Fig. 5.3b and 5.3c. The direct arrivals are removed and the trace amplitude is normalized. The reflection response of a) the overburden and b) the underburden. It shows that reflections from each side of the borehole are separated, including the internal multiples. The mismatch at the beginning of the traces in a) is most likely due to the reflectors very close to the borehole.

The goal is to transform the original datasets into what would be recorded as if they were modeled in the two reference states as shown in Fig. 5.3b and 5.3c, so that the different time shifts caused by the changes in the overburden and the underburden are separated. In these two reference states, both source and receivers are moved to the borehole depth. Furthermore, the velocity on the other side of the borehole is homogenized, meaning that the interfering reflections from the other side are removed in the new responses. This leads to a higher signal-to-noise ratio compared to the original data.

Applying the process flow (Fig. 5.2) to the base and monitor data, the new reflection responses of the overburden and the underburden are retrieved. For validation, the zero-offset gathers are checked against the directly modeled traces in Fig. 5.4. These reference traces are modeled according to Fig. 5.3b and 5.3c, and the direct arrivals are removed. The trace amplitudes are normalized in the figure. This comparison validates the correct retrieval of our new responses. The figure shows that the phases of the reflections match well, even for the later arrivals, meaning that the multiples from the other side are indeed removed.

Next, for an overview of the new responses, all zero-offset monitor traces are plotted in red against the base traces in black in Fig. 5.5. In the zoomed-in insets in Fig. 5.5b (the new response of the underburden), the shorter traveltime in the red monitor traces can be noticed, while this shorted traveltime is not directly observable in Fig. 5.5c (the original surface response) and Fig. 5.5d (the original borehole response). In addition, the clear separation of the reflections on each side of the borehole is appreciated in the new response from Fig. 5.5b and Fig. 5.5a, compared to Fig. 5.5c and Fig. 5.5d.

To check the new time shifts, Fig. 5.6 shows the detailed result for the lateral position

of 3025 m, where a standard cross correlation method (Landrø et al., 2001) is used. All the zero-offset traces are first interpolated to a sampling interval of 0.4 ms, and then a sliding cross correlation window 0.2 s is used. Fig. 5.6a and 5.6c are the velocity change (monitor − base) profiles along $x_1 = 3025$ m in the overburden and the underburden, respectively. Fig. 5.6b and Fig. 5.6d show the time shifts from the new response in blue, checked against those from the modeled response in red (dash-dot) and those directly obtained from the velocities in green (dashed). The comparison confirms that the new time shifts agree well with the given velocity model and that small time shifts from the deep part of the model can be found with this data-driven approach.

Fig. 5.7 and 5.8 show the overall time shift maps and the time strain maps, respectively. Fig. 5.7a joins the time shift maps of the overburden and the underburden, and the dashed line denotes the borehole depth. Each half is calculated independently from the new responses. It shows clearly that the opposite time shifts are separated by this method. For comparison, the time shift maps from the original surface and borehole data are shown in Fig. 5.7b and 5.7c, respectively. We see that a big difference between the new map in Fig. 5.7a and the map in Fig. 5.7b is that the time shift accumulates from different depths. One from the borehole depth, and the other from the surface. So for studying the medium changes near borehole, this new approach has its advantage. It can also be observed that in the time strain maps (Fig. 5.8), more details of the reflectors below the borehole are shown by the new approach (Fig. 5.8a) than the maps from the surface data (Fig. 5.8b) and the borehole data (Fig. 5.8c).

5.3.2 Gullfaks model

The second example is based on the Gullfaks field, where the time-lapse seismic method has been applied with great success. Different from the previous example, here the velocity changes are made more realistic according to the geological structures and field measurements. We first present the result, then we make comparison to the field observation in a separate subsection.

The base P-wave velocity model is shown in Fig. 5.9a, where the vertical dashed line ($x_1 = 3865$ m) indicates the reference position where the result will be compared with the field data. The velocity profile along this line is modified according to a well log. The two horizontal dashed lines mark the two horizons just below the synthetic well depth at 1700 m, namely Base Cretaceous Unconformity (BCU, 1830 m) and Top Statfjord (T.S., 1885 m). Fig. 5.9b and Fig. 5.9c show the medium states where the new responses are retrieved. Fig. 5.9d shows the overall time-lapse velocity change. The velocity change is zero in the layer below BCU and is positive (100 m/s) in the layer below Top Statfjord due to the pore pressure drop (which is to be explained in the field data comparison subsection). The velocity change in the layers between the seabed and BCU is made negative (2% decrease) in order to show that the detection of the velocity increase below Top Statfjord will not be affected using our method even when there is a velocity decrease above.

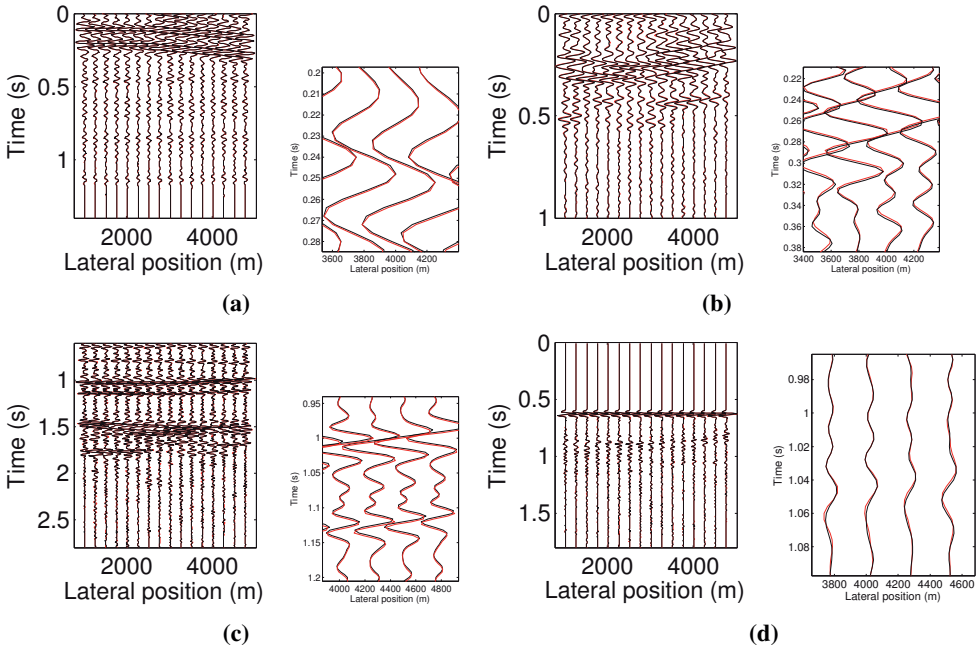

Figure 5.5: The overall zero-offset trace view of the base response (in black) and monitor data (in red). A zoomed-in view is shown on the right in each panel. The new response of a) the overburden and b) the underburden. It is observed in b) that the monitor response has a smaller traveltime than the base response, indicating a velocity increase. The original response from c) the surface data (with the direct arrivals removed) and d) the borehole data, where the direct arrivals are kept because they contain information of the changes in the overburden. In the zoomed-in windows, only the increase of traveltime is observed in both original datasets, unlike in the new response in b). Besides, the ambiguity of the primary reflections and the internal multiples are also problematic for time shift estimation near the borehole in c) and d).

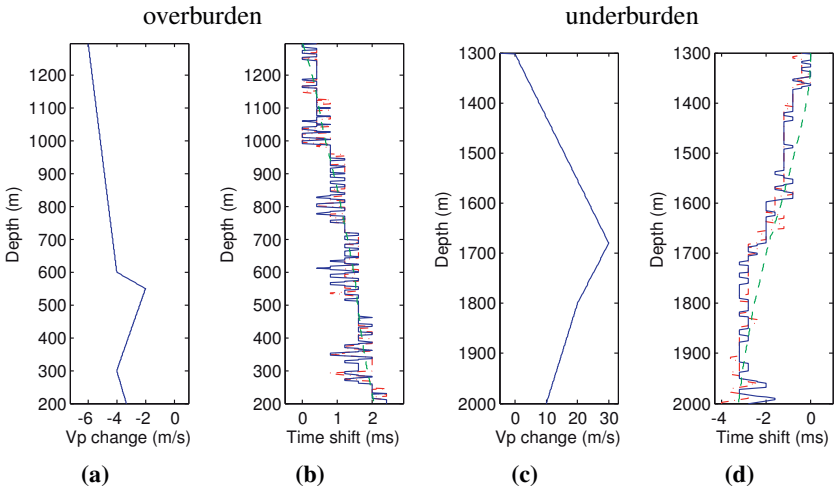

Figure 5.6: The velocity change profiles at $x_1 = 3025$ m of a) the overburden and c) the underburden. b) & d) The estimated time shifts from the new responses in Fig. 5.5a and 5.5b, respectively. The blue line is obtained from the retrieved new response using cross correlation, and the red dash-dot line is obtained from the modeled reference response. The green dashed line is obtained by directly computing the time shifts from the velocities. The cross correlation window size is 0.2 ms. The vertical axis in a) is flipped to reflect that the retrieved response here is obtained from below (as in Fig. 5.3b). For a direct comparison, the time shifts by cross correlation are converted to depth using the base velocities. It is observed that the different time shifts in the overburden and the underburden are well separated, and the new estimate in blue agree well with the ones in red and green.

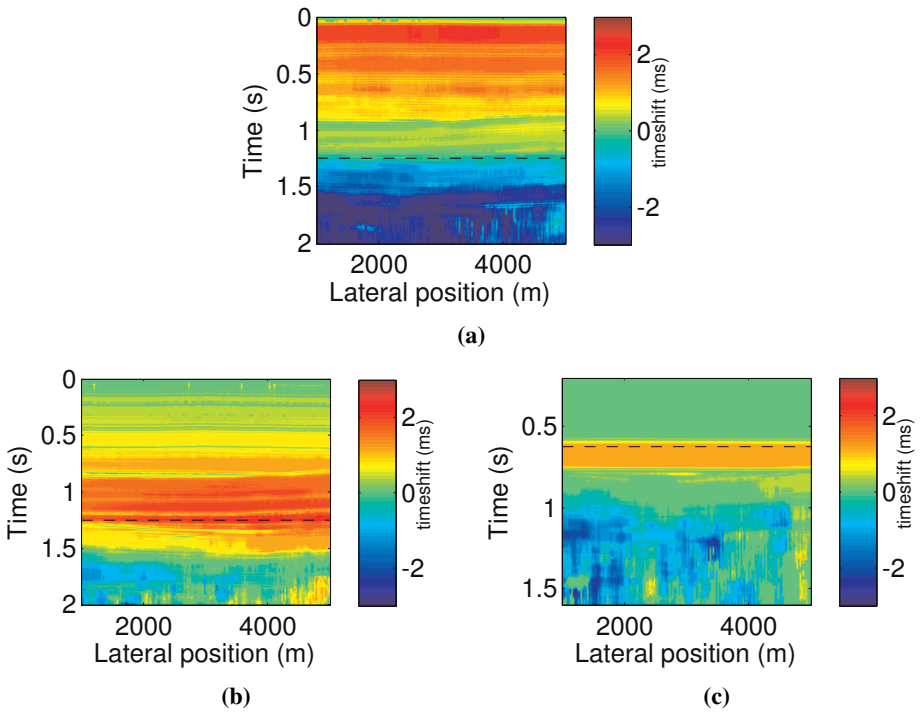

Figure 5.7: The smoothed time shift maps. a) The joined map of the overburden and the underburden, calculated separately using the new responses. b) & c) are the maps from the original surface reflection and the borehole data, respectively. The dashed line indicates the borehole depth in time, which is the two-way traveltime in a) & b), and the one-way traveltime in c). The cross correlation window is 0.2 s for all panels. The new joined map in a) shows the separated positive and negative time shifts clearly, while the accumulative nature of traveltime for deep events needs to be taken into account when interpretating the results in b) and c).

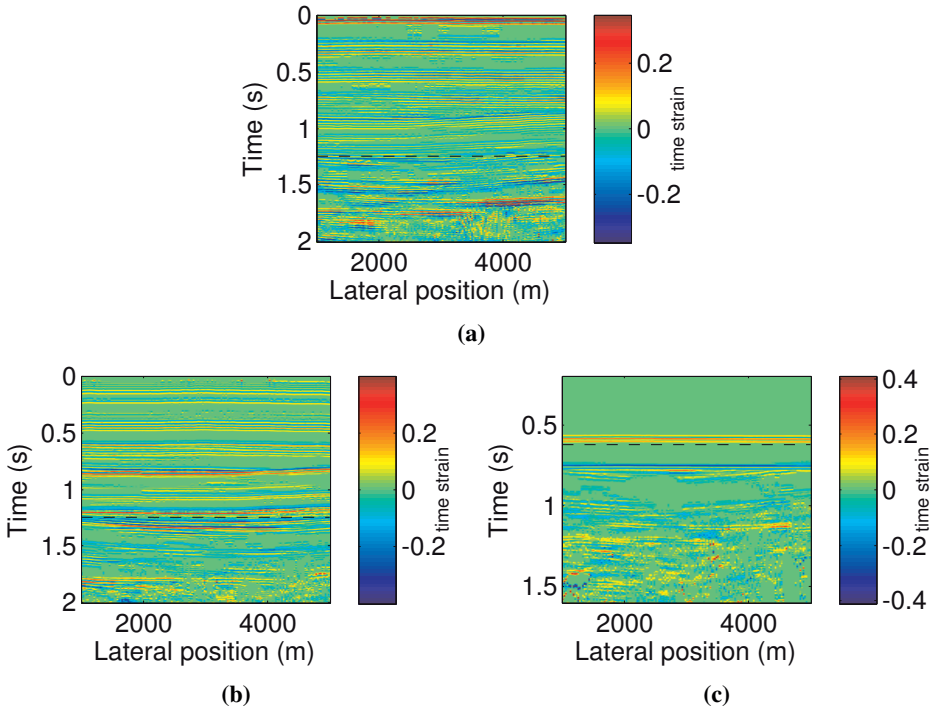

Figure 5.8: The time strain maps based on Fig. 5.7. a) The joined map of the overburden and the underburden. b) & c) are the maps from the original the surface reflection and the borehole data, respectively. The dashed line indicates the borehole depth in time. More details of the underburden are noticeable in a) than in c) or d), and they agree well with the geological model (Fig. 5.3a) and the synthetic velocity change (Fig. 5.3d).

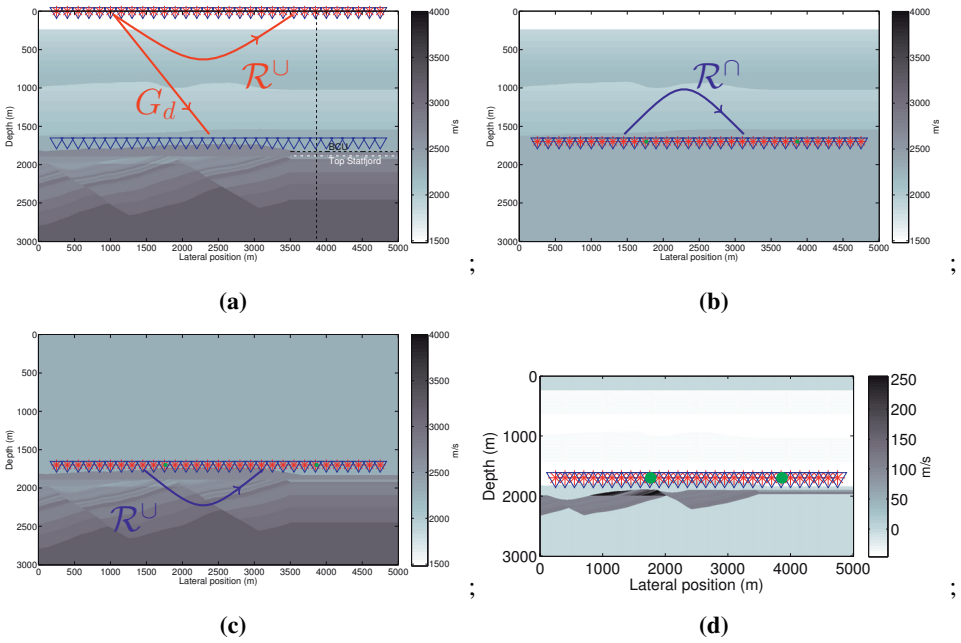

Figure 5.9: A P-wave velocity model of the Gullfaks field and the synthetic datasets geometries. The stars denote sources and the triangles denote receivers. The red letters denote the input data and the blue letters denote the unknown responses. a) The base velocity model. The vertical dashed line indicates the position where the results are compared to that from the field data. Two major horizons below the borehole depth, namely BCU and Top Statfjord, are marked with the horizontal dashed lines. b) The medium configuration where the responses of the overburden are retrieved. c) Same as b) but of the underburden. d) The overall velocity change. The green circles show the reference virtual source positions. The velocity changes are designed for comparison with the field measurement.

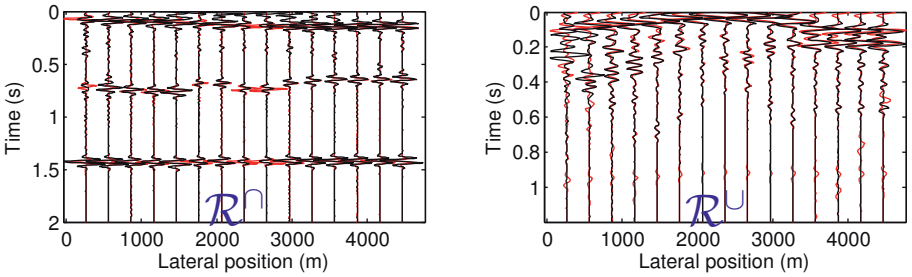

(a) **(b)**

Figure 5.10: The validation of the new zero-offset responses in black against the modeled reference traces in red. The direct arrivals removed and the trace amplitude is normalized. The reflection response of a) the overburden and b) the underburden. The mismatch on both ends of the borehole in b) is suspected to be due to the limited source aperture at the surface, as the aperture is not much wider than the receiver apertures at the borehole depth. The limited receiver aperture could also be part of the reason, because the integrals are truncated in solving Eq. 5.2. This aperture effect on the source side is less severe in a) because of the two integral surface in Eq. 5.1 rather than one in Eq. 5.2.

For validation, Fig. 5.10 shows the zero-offset comparison with the modeled responses (as in Fig. 5.9b and 5.9c). The amplitudes are normalized and the direct arrivals are removed. Fig. 5.10a is the reflection responses of the overburden, and Fig. 5.10b is that of the underburden. The first observation is that all multiples from the other side are indeed removed as seen in the match of the late events. This gives an improved signal-to-noise ratio for the events near the borehole, compared to the original data. Second, despite some mismatch, the phase of the reflections are overall well recovered. The mismatches seen at the beginning and ending sides of the lateral position axis in Fig. 5.10b are mainly due to the limited source aperture at the surface and the relatively large lateral inhomogeneity of the structures. For 4D applications, some of these phase mismatches between monitor and base surveys can be canceled out when traveltime differences are computed.

Next, for an overview of the new 4D responses, all zero-offset monitor traces are plotted in red over the base traces in black in Fig. 5.11. In Fig. 5.11b, the response of the underburden, the red signals (monitor response) arrive before those in black (base response) near the reservoir (close to the lateral position of 1500 m), and slightly after at the lateral position of 3865 m. This indicates a velocity increase in the reservoir and a slight decrease below the borehole near the lateral position of 3865 m. Such subtle difference is not directly observable either in Fig. 5.11c (the original surface data) or Fig. 5.11d (the original borehole data). Moreover, identifying the reflections near the borehole in these datasets is difficult by itself due to multiple reflections and the ambiguity of direction of the reflections, while such problems are alleviated using this approach.

For validation of the time shifts, the detailed results for the lateral position of 1765 m and

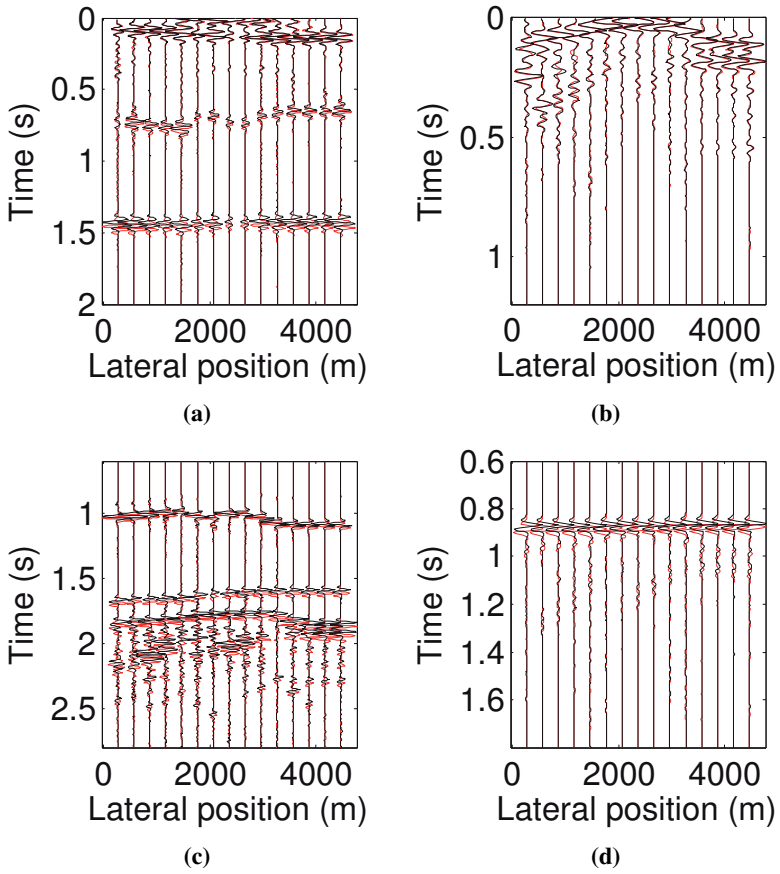

Figure 5.11: The overall zero-offset trace view of the base response (in black) and the monitor response (in red). The response of a) the overburden and b) the underburden. The increase in traveltime caused by the velocity decrease in the overburden is observable in a), and so is the decrease in traveltime caused by the velocity increase in the underburden in b). c) A selected part of the original surface data with the direct arrivals removed. d) A selected part of the borehole data with direct arrivals kept. Only the positive time shifts are observable in both c) and d). Because of the strong amplitude of the direct arrivals in d), the identification of the reflections is not as clear as in b).

3865 m are shown in Fig. 5.12 and Fig. 5.13, together with the velocity change profiles. The time shifts from the new responses are shown in blue, and those from the modeled responses are shown in red. The green line shows the time shift computed from the given velocities. The cross correlation window size is indicated in the figure captions. These two figures show that the time shifts are estimated correctly from the new responses and that the detailed small time shifts at each side of the borehole can be observed. Overall, the velocity increases below the borehole, but the velocity decreases slightly in the layer where the borehole is located, so a small positive time shift of about 1 ms is found in both Fig. 5.12d and 5.13d. For the area above the borehole, the velocity decrease in the model is also correctly matched by the positive time shifts in Fig. 5.12b and 5.13b.

The overall time shift and time strain maps are shown in Fig. 5.14 and 5.15, respectively, including those from the original surface and borehole data. Fig. 5.14a is the joined time shift map of the overburden and the underburden, separated by dashed line as the borehole depth. Each half is calculated using the corresponding new responses shown in Fig. 5.11a and 5.11b. Compared with Fig. 5.14b and 5.14c from the original data, Fig. 5.14a shows a correct separation of the time shifts above and below the borehole, and the changes in the deep part of the model is also present with correct positions. The change in the reservoir, marked by the circle, is clearly visible in Fig. 5.14a. Note that no velocity information or primary picking is used during the process. Similarly, the joined time strain map in Fig. 5.15a (the new responses) also shows more details than Fig. 5.15b (the surface data) and 5.15c (the borehole data). Overall, it appears difficult to directly use the maps from the original data (Fig. 5.14b, 5.14c, 5.15b and 5.15c) for characterization near the borehole without any prior manual event interpretation.

As this numerical experiment is designed for a comparison of the time shift of the event below Top Statfjord to that from the field data, we end this section with a brief explanation on the field data.

The base data are acquired in one well, while water is being injected in another well, a few hundred meters away. Then the monitor data are acquired after some waiting time. Fig. 5.16 shows the two picked horizons (Top Statfjord and BCU), in relation to the acquisition well position and some of the layer properties. From the field data, the average time shift for the event below Top Statfjord is -0.7 ms (+/- 0.5 ms). This corresponds to a velocity increase of about 40 m/s using the following relation (Landrø and Stammeijer, 2004), given a layer thickness of 60 m, zero layer thickness change and a velocity of 2500 m/s in the layer,

$$\frac{\triangle t}{t} \approx \frac{\triangle z}{z} - \frac{\triangle v}{v}, \tag{5.10}$$

where t is the two-way time, z the layer thickness, and v the velocity of the layer.

In this model, the estimation of the layer thickness below Top Statfjord (1885 m) ranges from 35 m to 85 m. According to a time shift of -0.7 ms from the field data, this corresponds to a velocity increase of about 70 m/s to 30 m/s. And for a time shift of 1.5 ms, the corresponding velocity change is about 130 m/s and 60 m/s. Therefore, in the numerical modeling, a velocity increase of 70 m/s is used (Fig. 5.13c), so a time shift of about -1 ms

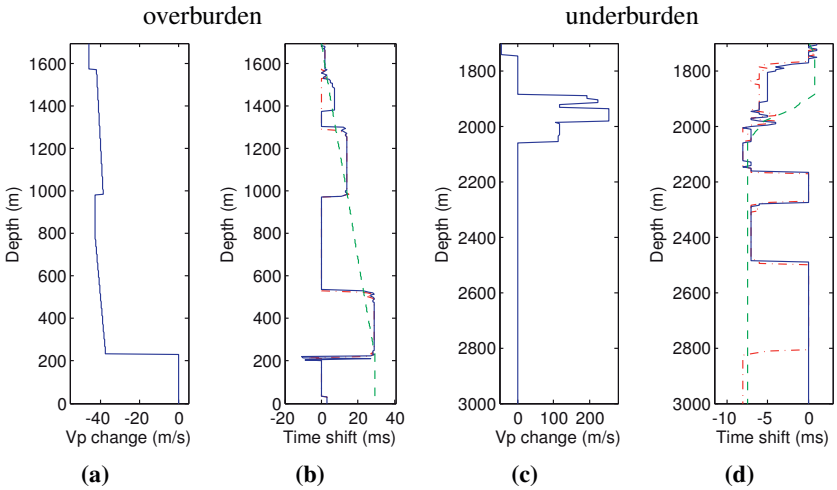

Figure 5.12: The velocity change profiles at $x_1 = 1765$ m of a) the overburden and c) the underburden. b) & d) The estimated time shifts from the new responses in Fig. 5.11a and 5.11b, respectively. The blue line is obtained from the retrieved new response using cross correlation with a window size of 0.15 s for both a) and b). The red dash-dot line is from the modeled response, and the green dashed line is computed directly from the velocities. The vertical axis in a) is flipped to reflect that the retrieved response is obtained from below (see in Fig. 5.9b). For a direct comparison, the results by cross correlation are converted to depth using the base velocities. Some of the time shifts by cross correlation go to zero because the amplitudes of late events are small and a threshold value for cross correlation is used for stability.

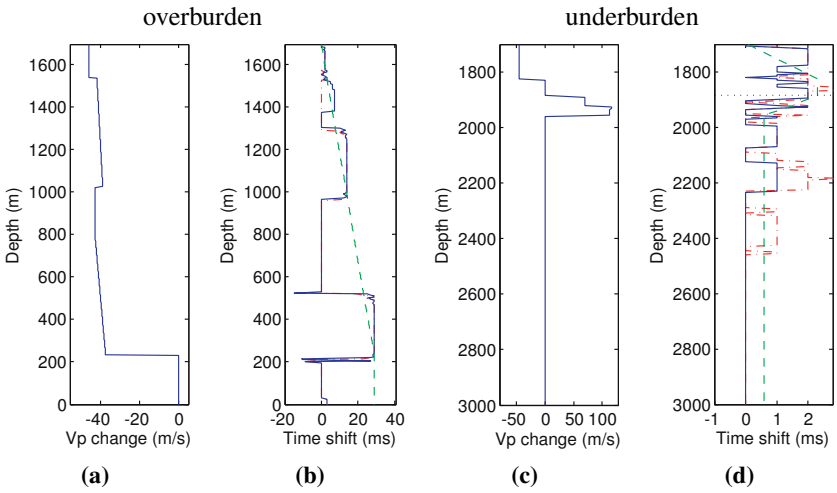

Figure 5.13: The velocity change profiles at $x_1 = 3865$ m of a) the overburden and c) the underburden. b) & d) The estimated time shifts from the new responses in Fig. 5.11a and 5.11b, respectively. The blue line is obtained from the retrieved new response using cross correlation with a window size of 0.15 s for a) and 0.1 s for b). The red dash-dot line is calculated from the modeled response, and the green dashed line is computed directly from the velocities. The black dotted line in d) indicates the layer below Top Statfjord (1885 m).

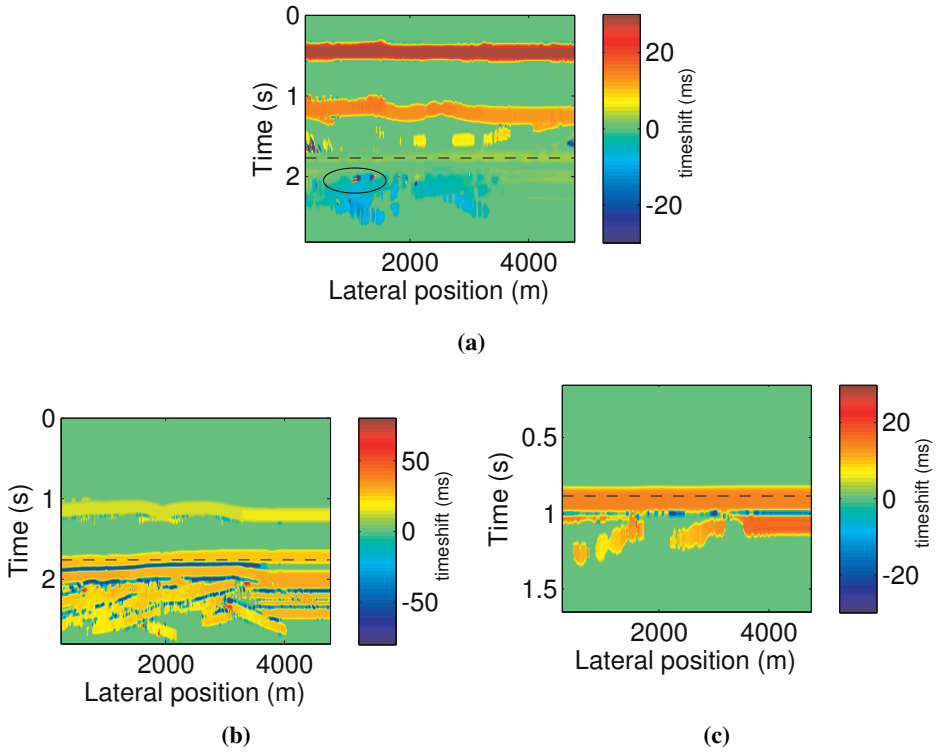

Figure 5.14: The smoothed time shift maps as in Fig. 5.7. a) The joined map of the overburden and the underburden. b) & c) The individual maps from the original surface reflection and the borehole data, respectively. The dashed line indicates the borehole depth in time. The cross correlation window is 0.15 s for all panels. The circled area indicates the location of the changes in the reservoir.

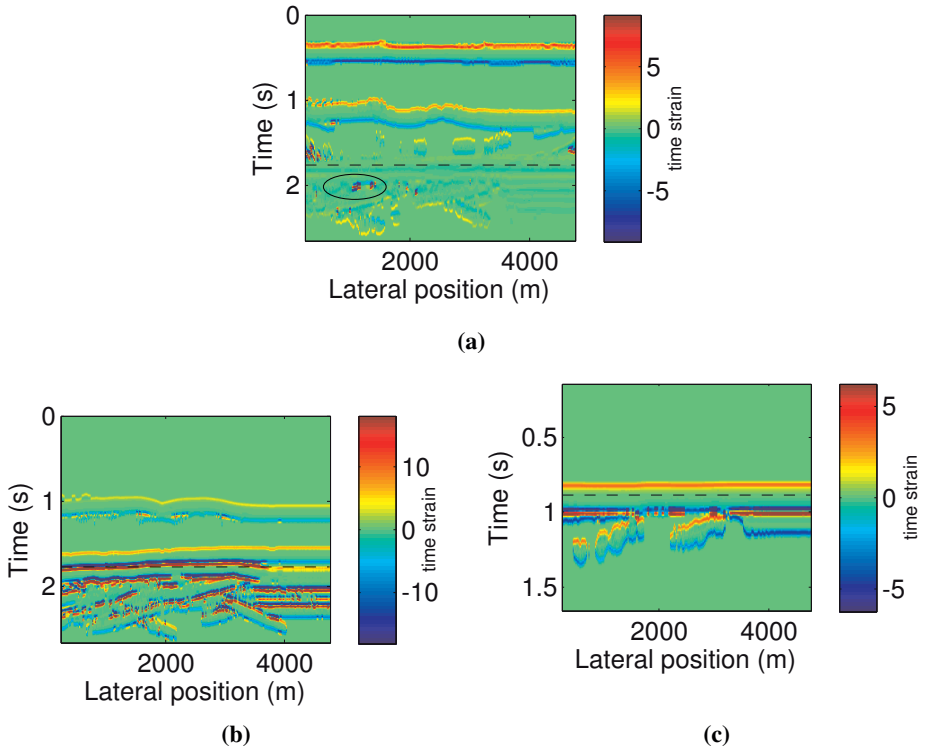

Figure 5.15: The time strain maps based on Fig. 5.14. The joined map in a) shows correctly the position of the changes in the model, while these features are lacking in the maps from the original surface data in b) and borehole data in c). The change in the reservoir is highlighted by the eclipse.

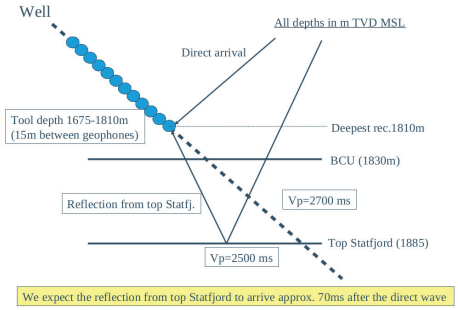

Figure 5.16: A sketch of the major horizons in relation to the acquisition well.

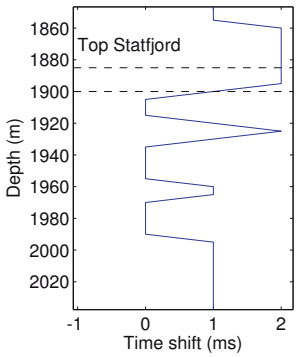

Figure 5.17: The detailed time shift from Fig. 5.13d for comparison with the field data result. The upper dashed black line denotes the depth of Top Statfjord, and the lower line denotes the depth of 1900 m. The time shift decreases from 2 ms at Top Statfjord to 1 ms at the second line. This corresponds to a time shift of -1 ms for this layer. The average time shift from the field data for the event below Top Statfjord is -0.7 ms.

should be expected.

Another comment regarding the synthetic monitor velocity model is that a velocity decrease above BCU is used, which is not likely the case for the field data. But this velocity decrease is used here to show that one can estimate the traveltime change in the underburden, without any effect from the overburden. And likewise, one can estimate the traveltime change in the overburden, without any effect from the underburden.

Fig. 5.17 shows the detailed time shift from the new response at $x = 3865$ m. For a comparison with the field data result that is targeted to the event below Top Statfjord, one should first take the difference of the time shift at Top Statfjord and the layer below. As indicated in the figure, the difference is estimated to be -1 ms, therefore, this is in reasonable agreement with the expected value and the field data observation of -0.7 ms.

5.4 Discussion

The proposed method aims at separating the reflection responses above and below a horizontal borehole without any velocity information. Based on the two numerical examples, we see that the method is good at detecting small changes ($<$1 ms) near the borehole. This sensitivity to small velocity change has similarly been observed in coda wave interferometry, this is because parts of the coda are preserved in the retrieved responses. But different from conventional coda wave interferometry, there is also a separation of the coda above and below the borehole (for this scenario), as the full waveforms are retrieved in truncated media.

For the 2D case with a horizontal borehole, the examples show that this approach is useful for time-lapse characterization of the deep part of the model, even for small velocity changes. Correct and detailed time shifts directly related to changes near the borehole are found. The process is completely data-driven in this 2D case, and no velocity information is needed. The use of borehole data, has significant benefits, especially for time-lapse studies (Bakulin et al., 2007), because the measured data in boreholes naturally account for the changes in the overburden. In case the measured direct arrival is not satisfactory, some interpolation based on the existing traveltime curve can be used without using a velocity model. Furthermore, in case the focusing function cannot be found, approximate solutions (Liu et al., 2016b) to the desired reflection responses are still sufficient for evaluating the changes close to the borehole, except that the multiples are not completely removed in that case. The added advantage of using the Marchenko scheme allows the retrieval of the reflection response using single-component data without any multiples from the other side of the borehole. Some small reflection events that are difficult to identify from the original surface or borehole data can be retrieved automatically by this method.

This method provides a different way of using the borehole data, complementing well with those that use the direct arrivals for the changes at shallower depths (Zadeh and Landrø, 2011). Regarding the amplitude and AVO inversion studies, we believe it is possible to use the relative amplitudes of the new response, provided that a wide survey aperture is available at the surface and the survey repeatability issue is manageable.

For 3D application, if there is an adequate coverage with multiple horizontal boreholes, the method can be still be described as velocity-independent. But a more realistic case would be that there is only partial coverage with horizontal boreholes. Then the direct arrivals from a single borehole would not be enough to describe the traveltime from the target plane to the surface. Local interpolation near the well should be considered, and velocity information would be needed in that case, but only for the volume between the borehole level to the surface. Therefore, for the use of existing velocity models, it would most likely be necessary for 3D application. Then in the case of an erroneous velocity model, ghost events are observed in the up-down wavefields (Thorbecke et al., 2013) when there are phase errors in direct arrivals , while the amplitude errors may be corrected (de Ridder et al., 2016).

Other concerning practical issues are the following. A wide source coverage at the surface is desirable for retrieving the correct phase and amplitude information in the new responses. Both source signal deconvolution and free surface multiple removal are assumed in the numerical examples, but should be dealt with in practice. In addition, we assume a lossless medium in modeling the data. For the latter two, the extension to include surface-related multiples in the Marchenko method is shown by Singh et al. (2017) and the Marchenko method for dissipative media is discussed in Slob et al. (2016).

Regarding non-horizontal boreholes, if the well is only slightly deviated, then one could first apply some local phase shift to adjust the borehole data to a desired level before using the method. That would require the velocity of that level only, not a complete velocity model. On the other hand, the restriction to horizontal boreholes is lifted when a good background velocity model is available. Because the full Marchenko method can provide the focusing functions and up-down wavefield at every grid point in the model, numerous possibilities for modelling, imaging, and monitoring open up (Wapenaar et al., 2014; Meles et al., 2016; van der Neut and Wapenaar, 2016).

5.5 Conclusions

We present a new approach to combine the data at the surface and in a horizontal borehole for finding the traveltime changes close to the borehole. The numerical examples show that the time shifts for the deep events are obtained correctly without any manual event picking. Both the location and the magnitude of the changes near the borehole are identified more clearly than those from the original data. For 2D, the method is completely data-driven given a good source coverage at the surface. For 3D, it is most likely that interpolation for the direct traveltime is needed. Although practical limitations related to the Marchenko method exist, we believe that this proposal of joining the surface data with the borehole data is nevertheless worth exploiting for robust subsurface monitoring.

5.6 Acknowledgements

The authors acknowledge the Norwegian Research Council and the sponsors of the ROSE consortium at NTNU for financial support, and Jan Thorbecke at TU Delft for the open source modeling package.The authors thank the associate editor and the reviewers for their comments that helped to improve the paper.

Chapter 6

Conclusion

The main objective of this doctoral work is to develop new methods for high-quality borehole imaging in the presence of velocity uncertainties.

This is achieved by, first of all, virtually moving sources and receivers to the borehole level so that the traveltime to the imaging target is shortened. In doing so, the effect of the velocity errors in the model is reduced, simply because the distance that the signal travels is equal to its travel time multiplied by the propagation velocity. A simple analogy, one person owns 100 shares of some stock, while the other person owns 100,000 shares. Then the price of that stock drops 4 kr. In this case, the first person loses 400 kr and the second person loses 400,000 kr. The first one is better off. Therefore, in a sense, the purpose of the redatuming scheme proposed in this thesis is to reduce the number of 'shares'.

The second point is that this process of reducing the number of 'shares' is completely data-driven, meaning velocity independent. This is different from conventional redatuming methods that require a velocity model. In this data-driven approach, the redatumed result is obtained, essentially, by the simple operation of summation. To be more specific, it is the summation of many cross-correlated traces.

The third point is that after redatuming, the reflection response of the medium above and below can be separated, resulting in a higher signal-to-noise ratio in the new data. The potential application of this feature includes clearer imaging near boreholes (Chapter. 3) and a more direct 4D time shift analysis near boreholes (Chapter. 5). The key in this process is the retrieval of the special focusing wavefield that is described in detail in Chapter. 3 and in Appendix. B. By using the measured borehole data, the retrieval of this focusing wavefield no longer requires any velocity model. This focusing wavefield enables the up-down wavefield reconstruction in boreholes using single-component data only. The numerical experiments suggest that similar results to those by conventional multi-component methods can be obtained without any extra field cost. Chapter. 2 shows numerical examples where the method is applied to different borehole geometries, not limited to the horizontal case.

As an overall summary, Chapter. 2 investigates the inter-source type of SI to turn drill-bit

into virtual receivers. It concludes that the estimate of the drill-bit source signal is essential for such an application. Then Chapter. 3 shows the essential velocity-free redatuming schemes for data acquired in horizontal boreholes. After redatuming, the reflection response of the medium below and above the borehole can be obtained. Then two separate images, one for above the borehole, and one for below, can be calculated by migrating these reflection responses. To image above the borehole, four alternative schemes are suggested, and one of them fully removes the internal multiples from above the borehole. To image below the borehole, two alternative schemes are suggested, and one of them fully accounts for the internal multiples from below the borehole. Given the same erroneous velocity model for migration, all of the suggested schemes result in better positioned images near the borehole, as compared to those from the original data. Chapter. 4 studies further the use of the focusing wavefield in reconstructing the up-down wavefields in horizontal, deviated, and vertical boreholes. The application of the method for 4D analysis is presented in Chapter. 5. It is observed that by using the obtained reflection responses of the medium above and below (as shown in Chapter. 3), not only can the time shift in the overburden and the underburden be separated, but also that the detailed and accurate time shift can be directly estimated because of the removal of internal multiples and the new source and receiver positions.

The numerical experiments show that this data-drivenly computed focusing wavefield exhibits great potential for imaging and modelling, but from a practical point of view challenges remain.

- To compute the focusing wavefield, the surface reflection response needed in this process should ideally has a perfect source signal deconvolution (such that its amplitude spectrum is flat) and the surface-related multiples need to be removed. The work by Singh et al. (2017) shows that it is possible to include surface multiples in the retrieval scheme of the focusing wavefield. Alternatively, the redatuming schemes that does not need the exact focusing wavefield are also suggested in Chapter. 3. The numerical results show that these schemes still gives robust imaging near borehole in the presence of velocity errors.

- The surface reflection data and the borehole data need to be regularized in such a way that the positions of the sources in both datasets coincide. This means that in practice, inline interpolation is most likely needed prior to applying the redatuming schemes.

- The theory of the focusing wavefield assumes a general lossless inhomogeneous medium with moderately curved interfaces. Therefore, for the application to the borehole data, it assumes that medium near the borehole is smooth.

Possible extension to the doctoral work is the following.

- The current schemes assume acoustic response from the borehole data. The adaptation for the use of the vertical particle velocity from borehole can be studied, as they are more common in practice.

- The redatumed data can be considered for local tomographic mapping of velocity models near boreholes. This is because the method retrieves the correct traveltime of the reflections near the boreholes, which should be suitable for tomography.
- The application of the method to field data should be tested. And issues regarding imperfect source signal deconvolution in the surface data needs to be considered, and the borehole data redatuming schemes that include free-surface related multiples maybe considered.
- Attenuation may also be taken into account, and a related study on Marchenko imaging in a dissipative acoustic medium has been recently published by Slob et al. (2016).

To end, the proposed method, in a sense, processes the information in the data in a natural way, without much intervention. To use an analogy, from the classical view in physics, a mirror reflects light in the air where the angle of incidence is equal to the angle of reflection. But from the quantum view, light is actually reflected from every part of the mirror. It is just that the light interacts constructively from the part of the mirror where the light travels with the least time, and the reflected light from the rest part of the mirror cancels out. What is in play is merely the superposition principle and simple geometry, which is the same as with this method.

Appendix A

The reflection responses

Many of the equations used in the method is derived from the reciprocity theorems. The pressure-normalized one-way reciprocity theorems (Wapenaar and Berkhout, 1989) read in the frequency domain (denoted by the above the quantities, and the spatial variables are omitted for simplicity)

$$-\int_{\partial D_0}\rho^{-1}\{p_A^+(\partial_3 p_B^-)+\hat{p}_A^-(\partial_3\hat{p}_B^+)\}d\mathbf{x}_0=\int_{\partial D_i}\rho^{-1}\{(\partial_3\hat{p}_A^+)\hat{p}_B^-+(\partial_3\hat{p}_A^-)\hat{p}_B^+\}d\mathbf{x}_i \quad \text{(A.1)}$$

and

$$-\int_{\partial D_0}\rho^{-1}\{(\hat{p}_A^+)^*(\partial_3\hat{p}_B^+)+(\hat{p}_A^-)^*(\partial_3\hat{p}_B^+)\}d\mathbf{x}_0=\int_{\partial D_i}\rho^{-1}\{(\partial_3\hat{p}_A^+)^*\hat{p}_B^++(\partial_3\hat{p}_A^-)^*\hat{p}_B^-\}d\mathbf{x}_i. \quad \text{(A.2)}$$

The first is of the convolution type and the second is of the correlation type. The underlying assumption is that it is source free in the lossless medium denoted as domain D between the depth level ∂D_0 and ∂D_i, and that the medium parameters are the same in both states.

The Green's function $G = G(\mathbf{x}|\mathbf{x}_0^{''}, t)$ is defined as the causal solution to the following scalar wave equation in an actual inhomogeneous medium with an impulsive point source of volume injection rate at $\mathbf{x}_0^{''}$,

$$\rho(\mathbf{x})\nabla\cdot(\frac{1}{\rho(\mathbf{x})}\nabla G)-\frac{1}{c(\mathbf{x})^2}\frac{\partial^2 G}{\partial t^2}=-\rho(\mathbf{x})\delta(\mathbf{x}-\mathbf{x}_0^{''})\frac{\partial\delta(t)}{\partial t}. \quad \text{(A.3)}$$

Here $c(\mathbf{x})$ and $\rho(\mathbf{x})$ are the propagation velocity and mass density of the medium and t denotes time. By using the equation of motion, we write in the frequency domain, the vertical derivative of the downgoing Green's function at ∂D_0,

$$\partial_3\hat{G}^+(\mathbf{x}|\mathbf{x}_0^{''})|_{x_3=x_{3,0}}=\frac{1}{2}j\omega\rho(\mathbf{x}_0^{''})\delta(\mathbf{x}_H-\mathbf{x}_H^{''}), \quad \text{(A.4)}$$

where the source $\mathbf{x}_0^{''}$ is *just* above ∂D_0. Similarly (without further notification), $\mathbf{x}_i^{'}$ is *just* below ∂D_i, which represents a depth level i in the subsurface. This applies throughout this appendix.

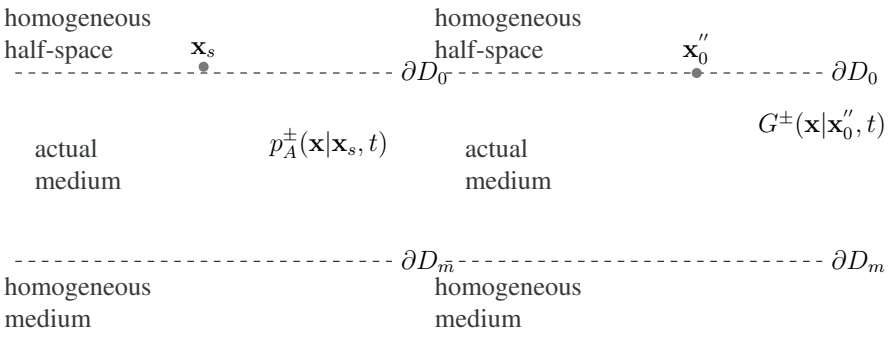

(a) State A **(b)** State B

Figure A.1: The medium configurations for introducing the definition of $\hat{\mathcal{R}}^{\cup}(\mathbf{x}_0''|\mathbf{x})$ in Eq. A.5. The domain D is identical to the actual inhomogeneous medium and bounded by an upper transparent boundary ∂D_0 and a lower boundary ∂D_m. The boundary ∂D_0 lies below a homogeneous half-space and ∂D_m lies below all inhomogeneities.

The definition of the surface reflection response $\mathcal{R}^{\cup}(\mathbf{x}_0''|\mathbf{x}_0, t)$ used in this thesis reads in the frequency domain

$$\hat{\mathcal{R}}^{\cup}(\mathbf{x}_0''|\mathbf{x}_0) = \frac{\partial_3 G^{-}(\mathbf{x}_0|\mathbf{x}_0'')|_{x_3=x_{3,0}}}{\frac{1}{2}j\omega\rho(\mathbf{x}_0)}. \tag{A.5}$$

This is obtained by using the reciprocity theorem in Eq. A.1 with the medium configurations shown in Fig. A.1, where $p_A^{\pm} = \hat{p}_A^{\pm}(\mathbf{x}|\mathbf{x}_s, t)$ and $p_B^{\pm} = G^{\pm}(\mathbf{x}|\mathbf{x}_0'', t)$.

The boundary conditions for each state is that for $\mathbf{x} \in \partial D_0$, Eq. A.4 applies, and for $\mathbf{x} \in \partial D_m$, $\partial_3 \hat{p}_A^{-}(\mathbf{x}|\mathbf{x}_s) = 0$ and $\hat{G}^{-}(\mathbf{x}|\mathbf{x}_0'') = 0$ apply. Substituting these boundary conditions into Eq. A.1 gives

$$\hat{p}_A^{-}(\mathbf{x}_0''|\mathbf{x}_s) = \int_{\partial D_0} \frac{\partial_3 \hat{G}^{-}(\mathbf{x}|\mathbf{x}_0'')}{\frac{1}{2}j\omega\rho(\mathbf{x})} \hat{p}_A^{+}(\mathbf{x}|\mathbf{x}_s) d\mathbf{x}_0. \tag{A.6}$$

Then by using the definition in Eq. A.5, Eq. A.6 reads

$$\hat{p}_A^{-}(\mathbf{x}_0''|\mathbf{x}_s) = \int_{\partial D_0} \hat{\mathcal{R}}^{\cup}(\mathbf{x}_0''|\mathbf{x}) \hat{p}_A^{+}(\mathbf{x}|\mathbf{x}_s) d\mathbf{x}_0, \tag{A.7}$$

where the upgoing pressure field $\hat{p}^{-}(\mathbf{x}_0''|\mathbf{x}_s)$ is related to the downgoing field $\hat{p}^{+}(\mathbf{x}|\mathbf{x}_s)$ via the reflection response $\hat{\mathcal{R}}^{\cup}(\mathbf{x}_0''|\mathbf{x})$.

Similarly, the scheme for imaging from above (Eq. 3.13) and the definition of the reflection response of the medium below $\hat{\mathcal{R}}^{\cup}(\mathbf{x}_i'|\mathbf{x}_i)$ can be obtained. The details are given in the Appendix B.2.1.

Appendix B

The focusing functions

B.1 The mutual relations

There are two focusing functions introduced in the previous literature on the Marchenko method, namely, $f_1^{\pm}(\mathbf{x}|\mathbf{x}_i^{'},t)$ and $f_2^{\pm}(\mathbf{x}|\mathbf{x}_0^{''},t)$, where the superscript $^{\pm}$ denotes the up- and downgoing components. They are defined in a reference medium, with an upper transparent boundary $\partial D_0 = x_{3,0} = 0$ and a lower boundary denoted as $\partial D_i = x_{3,i} = i$. The reference medium configurations are shown in Fig. B.1.

According to the reference medium configurations, the following focusing conditions can be formed and read in the frequency domain

$$\partial_3 \hat{f_1^-}(\mathbf{x}|\mathbf{x}_i^{'})|_{x_3=x_{3,i}} = 0 \tag{B.1}$$

$$\partial_3 \hat{f_1^+}(\mathbf{x}|\mathbf{x}_i^{'})|_{x_3=x_{3,i}} = -\frac{1}{2} j\omega\rho(\mathbf{x}_i^{'})\delta(\mathbf{x}_H - \mathbf{x}_H^{'}), \tag{B.2}$$

and

$$\partial_3 \hat{f_2^-}(\mathbf{x}|\mathbf{x}_0^{''})|_{x_3=x_{3,0}} = \frac{1}{2} j\omega\rho(\mathbf{x}_0^{''})\delta(\mathbf{x}_H - \mathbf{x}_H^{''}) \tag{B.3}$$

$$\partial_3 \hat{f_2^+}(\mathbf{x}|\mathbf{x}_0^{''})|_{x_3=x_{3,0}} = 0. \tag{B.4}$$

Applying the reciprocity theorems in Eq. A.1 and A.2 with these focusing conditions gives the mutual relations between the focusing functions

$$\hat{f_1^+}(\mathbf{x}_0^{''}|\mathbf{x}_i^{'}) = \hat{f_2^-}(\mathbf{x}_i^{'}|\mathbf{x}_0^{''}) \tag{B.5}$$

$$-\left\{\hat{f_1^-}(\mathbf{x}_0^{''}|\mathbf{x}_i^{'})\right\}^* = \hat{f_2^+}(\mathbf{x}_i^{'}|\mathbf{x}_0^{''}). \tag{B.6}$$

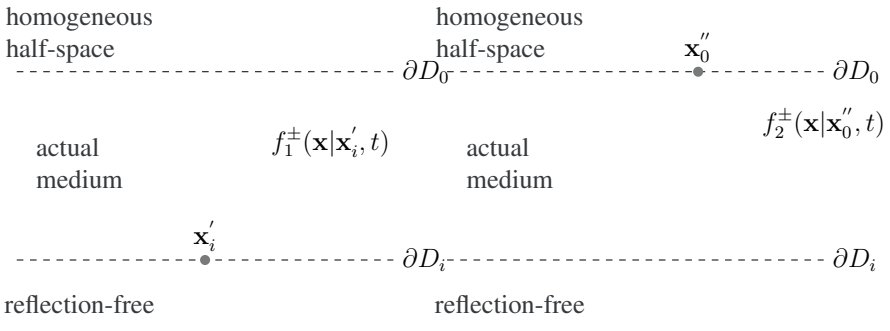

(a) State A **(b)** State B

Figure B.1: The medium configurations for deriving the mutual relation of the focusing functions. In state A, $p_A^{\pm} = f_1^{\pm}(\mathbf{x}|\mathbf{x}_i', t)$ and in state B, $p_B^{\pm} = f_2^{\pm}(\mathbf{x}|\mathbf{x}_0'', t)$.

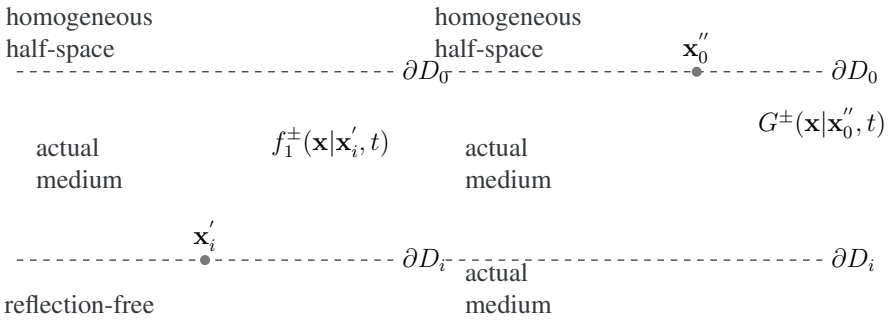

(a) State A **(b)** State B

Figure B.2: The medium configurations for deriving the relations between the one-way focusing functions and the up-and downgoing Green's functions. In state A, $p_A^{\pm} = f_1^{\pm}(\mathbf{x}|\mathbf{x}_i', t)$ and in state B, $p_B^{\pm} = G^{\pm}(\mathbf{x}|\mathbf{x}_0'', t)$.

B.2 The relation with the one-way Green's functions

Eq. 3.2 and 3.1 are obtained, once again, by applying the reciprocity theorems with the medium configurations shown in Fig. B.2b. In state A, the same focusing conditions (Eq. B.1 and B.2) are used. In state B, Eq. A.4 applies. Substituting these expressions into eq. A.1 and A.2, gives

$$\hat{G}^{-}(\mathbf{x}_i^{'}|\mathbf{x}_0^{''}) = \int_{\partial D_0} \hat{\mathcal{R}}^{\cup}(\mathbf{x}_0^{''}|\mathbf{x}_0)\hat{f_1^{+}}(\mathbf{x}_0|\mathbf{x}_i^{'})d\mathbf{x}_0 - \hat{f_1^{-}}(\mathbf{x}_0^{''}|\mathbf{x}_i^{'}) \tag{B.7}$$

$$\hat{G}^{+}(\mathbf{x}_i^{'}|\mathbf{x}_0^{''}) = -\int_{\partial D_0} \hat{\mathcal{R}}^{\cup}(\mathbf{x}_0^{''}|\mathbf{x}_0)\left\{\hat{f_1^{-}}(\mathbf{x}_0|\mathbf{x}_i^{'})\right\}^{*} d\mathbf{x}_0 + \left\{\hat{f_1^{+}}(\mathbf{x}_0^{''}|\mathbf{x}_i^{'})\right\}^{*}. \tag{B.8}$$

Then, by taking into account the causality of $G^{\pm}(\mathbf{x}_i^{'}|\mathbf{x}_0^{''},t)$ ($G^{\pm}(\mathbf{x}_i^{'}|\mathbf{x}_0^{''},t)=0$ for $t<t_d$, t_d is the direct traveltime from $\mathbf{x}_0^{''}$ to $\mathbf{x}_i^{'}$), Eq. 3.1 and 3.2 follow.

B.2.1 Imaging from above

To obtain the equation for imaging from above, the convolution type of reciprocity theorem is again used with the medium configurations shown in Fig. B.3. Therefore, the boundary on the left hand side of Eq. A.1 is changed to ∂D_i and that on the right hand side is changed to ∂D_m, which lies below all inhomogeneities.

According to the medium configurations in Fig. B.3, we have, at ∂D_i,

$$\partial_3\hat{G}^{+}(\mathbf{x}|\mathbf{x}_i^{'})|_{x_3=x_{3,i}} = \frac{1}{2}j\omega\rho(\mathbf{x}_i^{'})\delta(\mathbf{x}_H-\mathbf{x}_H^{'}). \tag{B.9}$$

in state B. And at ∂D_m, $\partial_3\hat{p}_A^{-}=0$ and $\hat{p}_B^{-}=0$. Substituting these boundary conditions into Eq. A.1 gives

$$\hat{G}^{-}(\mathbf{x}_i^{'}|\mathbf{x}_0^{''}) = \int_{\partial D_i} \frac{\partial_3\hat{G}^{-}(\mathbf{x}|\mathbf{x}_i^{'})}{\frac{1}{2}j\omega\rho(\mathbf{x}_i)}\hat{G}^{+}(\mathbf{x}_i|\mathbf{x}_0^{''})d\mathbf{x}_i. \tag{B.10}$$

By defining the reflection response from above $\mathcal{R}^{\cup}(\mathbf{x}_i^{'}|\mathbf{x}_i)$ as

$$\hat{\mathcal{R}}^{\cup}(\mathbf{x}_i^{'}|\mathbf{x}_i) = \frac{\partial_3\hat{G}^{-}(\mathbf{x}|\mathbf{x}_i^{'})|_{x_3=x_{3,i}}}{\frac{1}{2}j\omega\rho(\mathbf{x}_i)} \tag{B.11}$$

gives the frequency domain representation of Eq. 3.13..

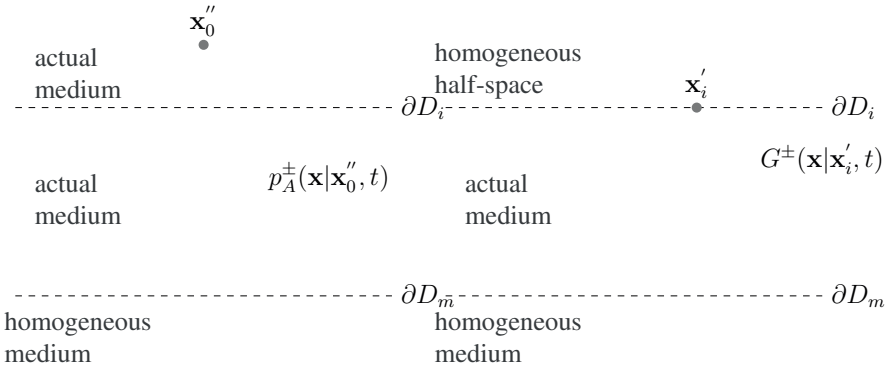

(a) State A **(b)** State B

Figure B.3: The medium configurations for deriving the equation for imaging from above, Eq. 3.13. In state A, $\hat{p}_A^{\pm} = \hat{G}^{\pm}(\mathbf{x}|\mathbf{x}_0'')\hat{s}(\mathbf{x}_0'')$, where $\hat{s}(\mathbf{x}_0'')$ denotes the source signature. In state B, $\hat{p}_B^{\pm} = \hat{G}^{\pm}(\mathbf{x}|\mathbf{x}_i')$, where there is an impulsive source at $\mathbf{x}_i'$.

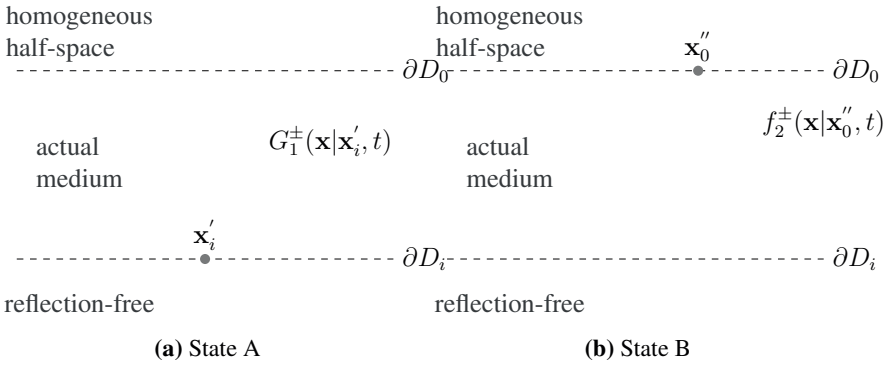

(a) State A **(b)** State B

Figure B.4: The medium configurations for deriving Eq. 3.20

B.2.2 Image from below

To derive Eq. 3.20, the medium states as shown in Fig. B.4 are used for the reciprocity theorem. For state A, we write

$$\hat{G}^{+}(\mathbf{x}_0|\mathbf{x}_i^{'}) = 0 \tag{B.12}$$

$$\partial_3 \hat{G}^{-}(\mathbf{x}_i^{'})|_{x_3=x_{3,i}} = \frac{1}{2} j\omega\rho(\mathbf{x}_i^{'})\delta(\mathbf{x}_H - \mathbf{x}_H^{'}), \tag{B.13}$$

and for state B, the focusing condition in Eq. B.4 applies. Substituting these conditions into Eq. A.1 gives

$$\hat{f_2^{+}}(\mathbf{x}_i^{'}|\mathbf{x}_0^{''}) = \int_{\partial D_i} \hat{\mathcal{R}^{\cap}}(\mathbf{x}_i^{'}|\mathbf{x}_i)\hat{f_2^{-}}(\mathbf{x}_i|\mathbf{x}_0^{''})d\mathbf{x}_i, \tag{B.14}$$

with

$$\hat{\mathcal{R}^{\cap}}(\mathbf{x}_i^{'}|\mathbf{x}_i) = \frac{\partial_3 \hat{G}^{+}(\mathbf{x}|\mathbf{x}_i^{'})|_{x_3=x_{3,i}}}{-\frac{1}{2} j\omega\rho(\mathbf{x}_i)}. \tag{B.15}$$

Then together with the mutual relations of $f_1^{\pm}$ and $f_2^{\pm}$ in Eq. B.5, B.6 and the causality of $G^{-}(\mathbf{x}_i^{'}|\mathbf{x}_0^{''}, t) = 0$ for $t < t_d(\mathbf{x}_i^{'}|\mathbf{x}_0^{''})$, the unknown $\hat{\mathcal{R}^{\cap}}(\mathbf{x}_i^{'}|\mathbf{x}_i)$ can be calculated after the focusing function $\hat{f_1^{+}}(\mathbf{x}_0|\mathbf{x}_i^{'})$ is obtained.

Appendix C

The iterative Marchenko scheme

The iterative Marchenko scheme reads

$$f^+_{1,k}(\mathbf{x}''_0|\mathbf{x}'_i,t) = f^+_{1,0}(\mathbf{x}''_0|\mathbf{x}'_i,t)+\theta(t+t_d(\mathbf{x}''_0|\mathbf{x}'_i))\int_{\partial D_0}\int_{-\infty}^{\infty}\mathcal{R}^{\cup}(\mathbf{x}''_0|\mathbf{x}'_0,t)f^-_{1,k-1}(\mathbf{x}'_0|\mathbf{x}'_i,t+t')dt'\,d\mathbf{x}'_0, \tag{C.1}$$

$$f^-_{1,k}(\mathbf{x}''_0|\mathbf{x}'_i,t) = \theta(t_d(\mathbf{x}''_0|\mathbf{x}'_i))-t)\int_{\partial D_0}\int_{-\infty}^{\infty}\mathcal{R}^{\cup}(\mathbf{x}''_0|\mathbf{x}'_0,t-t')f^+_{1,k}(\mathbf{x}'_0|\mathbf{x}'_i,t')dt'\,d\mathbf{x}'_0, \tag{C.2}$$

with

$$f^+_{1,0}(\mathbf{x}''_0|\mathbf{x}'_i,t) = G_d(\mathbf{x}'_i|\mathbf{x}''_0,-t),, \tag{C.3}$$

where $\theta(t)$ is the Heaviside function that passes the results for $t>0$.

The reason for the name of Marchenko is the following. Let $M(\mathbf{x}|\mathbf{x}''_0,-t) = -f^-_1(\mathbf{x}|\mathbf{x}''_0,t)$, then $M(\mathbf{x}|\mathbf{x}''_0,t)$ solves the 3D single-sided Marchenko equation (Wapenaar et al., 2013)

$$\begin{aligned}0 = &\int_{\partial D_0}\int_{-\infty}^{\infty}T^{inv}_d(\mathbf{x}|\mathbf{x}'_0,t')\mathcal{R}^{\cup}(\mathbf{x}'_0|\mathbf{x}''_0,t-t')dt'\,d\mathbf{x}'_0\\ &+\int_{\partial D_0}\int_{-t_d(\mathbf{x},\mathbf{x}'_0)}^{\infty}M(\mathbf{x}|\mathbf{x}'_0,t')\mathcal{R}^{\cup}(\mathbf{x}'_0|\mathbf{x}''_0,t-t')dt'\,d\mathbf{x}'_0 + M(\mathbf{x}|\mathbf{x}''_0,-t)\end{aligned} \tag{C.4}$$

for $\mathbf{x}\in D$ and $t<t_d(\mathbf{x},\mathbf{x}''_0)$, where T^{inv}_d is the inverse of the direct part of the transmission response.

Appendix D

List of publications

Journal papers

Yi Liu, Børge Arntsen, Joost van der Neut, Kees Wapenaar. 2017. Up-down wavefields recostruction in boreholes using single-component data. submitted to *Journal of Applied Geophysics*

Yi Liu, Martin Landrø, Børge Arntsen, Joost van der Neut, Kees Wapenaar. 2017. A new approach to discriminate 4D time shifts in the reservoir and overburden. *Geophysics*, Vol. 82.(6): Q67-Q78.

Joost van der Neut, Matteo Ravasi, Yi Liu, and Ivan Vasconcelos. 2017. Target-enclosed seismic imaging. *Geophysics*, Vol. 82(6): Q53-Q66.

Yi Liu, Joost van der Neut, Børge Arntsen and Kees Wapenaar. 2016. Data-driven deep local imaging near horizontal wells using both surface and borehole data. *Geophysical Journal International*, Vol. 205.(2): 758-775

Yi Liu, Deyan Draganov, Kees Wapenaar, and Børge Arntsen. 2016. Retrieving virtual reflection responses at drill-bit positions using seismic interferometry with drill-bit noise. *Geophysical Prospecting*, Vol. 64.(2): 348-360

Peer-reviewed conference proceedings

Yi Liu, Børge Arntsen, Martin Landrø, Joost van der Neut, and Kees Wapenaar. 2016. New method for discriminating 4D time shifts in the overburden ad reservoir. *SEG Technical Program Expanded Abstracts*: 5521-5526.

Yi Liu, Børge Arntsen, Joost van der Neut, Kees Wapenaar. 2016. Auto-estimation of up-down wavefields in a horizontal borehole using single component data. 78th EAGE Conference and Exhibition, Vienna, Tu-P04-06

Yi Liu , Joost van der Neut, Børge Arntsen, and Kees Wapenaar. 2015. Data-driven deep local imaging using both surface and borehole seismic data. *SEG Techical Program Expanded Abstracts*: 5554-5559.

Yi Liu, Deyan Draganov, Kees Wapenaar, and Børge Arntsen. 2015. Creating virtual receivers from drill-bit noise. 77th EAGE Conference and Exhibition, Madrid, WS15-A02

Yi Liu, Børge Arntsen, Kees Wapenaar, and Joost van der Neut. 2014. Combining inter-source seismic interferometry and source-receiver interferometry for deep local imaging. *SEG Technical Program Expanded Abstracts*: 5107-5112.

Yi Liu, Kees Wapenaar, and Børge Arntsen. 2014. Turning subsurface noise sources into virtual receivers by multi-dimensional deconvolution. 76th EAGE Conference and Exhibition, Amsterdam, Tu-P05-11.

Yi Liu, Børge Arntsen, Kees Wapenaar, and Anouar Romdhane. 2014. Inter-source seismic interferometry by multidimensional deconvolution (MDD) for borehole sources. SEG Beijing International Geophysical Conference and Exposition: 937-940.

References

Aarrestad, T. V., and Å. Kyllingstad, 1988, An experimental and theoretical study of a coupling mechanism between longitudinal and torsional drillstring vibrations at the bit: SPE Drilling Engineering, **3**, 12–18.

Amundsen, L., 1993, Wavenumber-based filtering of marine point-source data: Geophysics, **58**, 1335–1348.

———, 2001, Elimination of free-surface related multiples without need of the source wavelet: Geophysics, **66**, 327–341.

Amundsen, L., and A. Reitan, 1995, Decomposition of multicomponent sea-floor data into upgoing and downgoing P- and S-waves: Geophysics, **60**, 563–572.

Bakulin, A., and R. Calvert, 2006, The virtual source method: Theory and case study: Geophysics, **71**, SI139 – SI150.

Bakulin, A., A. Mateeva, K. Mehta, P. Jorgensen, J. Ferrandis, I. Sinha Herhold, and J. Lopez, 2007, Virtual source applications to imaging and reservoir monitoring: The Leading Edge, **26**, 732–740.

Balch, A. H., M. W. Lee, J. J. Miller, and R. T. Ryder, 1982, The use of vertical seismic profiles in seismic investigations of the Earth: Geophysics, **47**, 906–918.

Barkved, O. I., and T. Kristiansen, 2005, Seismic time-lapse effects and stress changes: Examples from a compacting reservoir: The Leading Edge, **24**, 1422 – 1248.

Barr, F. J., and J. I. Sanders, 1989, Attenuation of water-column reverbrations using pressure and velocity detectors in a water-bottom cable: SEG Technical Program Expanded Abstracts, 653–656.

Behura, J., K. Wapenaar, and R. Snieder, 2014, Autofocus imaging: Image reconstruction based on inverse scattering theory: Geophysics, **79**, A19–A26.

Broggini, F., R. Snieder, and K. Wapenaar, 2012, Focusing the wavefield inside an unknown 1D medium: Beyond seismic interferometry: Geophysics, **77**, A25 – A28.

Campillo, M., and A. Paul, 2003, Long-range correlations in the diffuse seismic coda: Science, **299**, 547–549.

Claerbout, J., 1968, Synthesis of a layered medium from its acoustic transmission response: Geophysics, **33**, 264–269.

Curtis, A., P. Gerstoft, H. Sato, R. Snieder, and K. Wapenaar, 2006, Seismic interferometry - turning noise into signal: The Leading Edge, **25**, 1082 – 1092.

Curtis, A., and D. Halliday, 2010, Source-receiver wave field interferometry: Phys. Rev. E, **81**, no. 4, 046601.

Curtis, A., H. Nicolson, D. Halliday, J. Trampert, and B. Baptie, 2009, Virtual seismome-

ters in the subsurface of the Earth from seismic interferometry: Nature Geoscience, **2**, 700 –704.

Daley, T. M., B. M. Freifeld, J. Ajo-Franklin, S. Dou, R. Pevzner, V. Shulakova, S. Kashikar, D. E. Miller, J. Goetz, J. Henninges, and S. Lueth, 2013, Field testing of fiber-optic distributed acoustic sensing (DAS) for subsurface seismic monitoring: The Leading Edge, **32**, 699–706.

Dankbaar, J. W. M., 1985, Separation of P- and S-waves: Geophysical Prospecting, **33**, 970–986.

de Ridder, S., A. Curtis, J. van der Neut, and K. Wapenaar, 2016, Marchenko wavefield redatuming, imaging conditions, and the effect of model errors: SEG Technical Program Expanded Abstracts 2016, 5155–5159.

Draganov, D., X. Campman, J. Thorbecke, A. Verdel, and K. Wapenaar, 2009, Reflection images from ambient seismic noise: Geophysics, **74**, A63 – A67.

———, 2013, Seismic exploration-scale velocities and structure from ambient seismic noise (>1 Hz): Journal of Geophysical Research: Solid Earth, **118**, 4345–4360.

Draganov, D., K. Wapenaar, W. Mulder, J. Singer, and A. Verdel, 2007, Retrieval of reflections from seismic background-noise measurements: Geophysical Research Letters, **34**, L04305.

Duncan, G., and G. Beresford, 1995, Some analyses of 2-D median f-k filters: Geophysics, **60**, 1157–1168.

Duvall, T. L., S. M. Jefferies, J. W. Harvey, and M. A. Pomerantz, 1993, Time-distance helioseismology: Nature, **362**, 430–432.

Eidsvik, J., and K. Hokstad, 2006, Positioning drill-bit and look-ahead events using seismic traveltime data: Geophysics, **71**, F79–F90.

Embree, P., J. P. Burg, and M. M. Backus, 1963, Wide-band velocity filtering - The pie slice process: Geophysics, **28**, 948–974.

Farhadiroushan, M., T. R. Parker, and S. Shatalin, 2009, Method and apparatus for optical sensing.

Fuck, R. F. i., A. Bakulin, and I. Tsvankin, 2009, Theory of traveltime shifts around compacting reservoirs: 3D solutions for heterogeneous anisotropic media: Geophysics, **74**, D25 –D36.

Galetti, E., and A. Curtis, 2012, Generalised receiver functions and seismic interferometry: Tectonophysics, **532-535**, 1 – 26.

Gerstoft, P., K. Sabra, P. Roux, W. Kuperman, and M. Fehler, 2006, Green's functions extraction and surface-wave tomography from microseisms in southern california: Geophysics, **71**, SI23–SI31.

Guilbot, J., and B. Smith, 2002, 4-D constrained depth conversion for reservoir compaction estimation: Application to Ekofisk Field: The Leading Edge, **21**, 302–308.

Guitton, A., and D. J. Verschuur, 2004, Adaptive subtraction of multiples using the L1-norm: Geophysical Prospecting, **52**, 27–38.

Haldorsen, J. B., D. E. Miller, and J. J. Walsh, 1995, Walk-away VSP using drill noise as a source: Geophysics, **60**, 978–997.

Hardage, B. A., 1985, Vertical seismic profiling, part a: Principles by bob a. hardage: Geophysical Press.

Hatchell, P., and S. Bourne, 2005, Rocks under strain: Strain-induced time-lapse time shifts are observed for depleting reservoirs: The Leading Edge, **24**, 1222–1225.

Hodgson, N., C. MacBeth, L. Duranti, J. Rickett, and K. Nihei, 2007, Inverting for reservoir pressure change using time-lapse time strain: Application to genesis field, gulf of mexico: The Leading Edge, **26**, 649–652.

Ikelle, L. T., and L. Amundsen, 2005, Introduction to petroleum seismology: Society of Exploration Geophysicists.

Kennett, P., R. Ireson, and P. Conn, 1980, Vertical seismic profiles: Their applications in exploration geophysics: Geophysical Prospecting, **28**, 676–699.

Landrø, M., P. Digranes, and L. K. Strønen, 2001, Technical article: Mapping reservoir pressure and saturation changes using seismic methods - possibilities and limitations: First Break, **19**, 671–684.

Landrø, M., O. A. Solheim, E. Hilde, B. O. Ekren, and L. K. Strønen, 1999, The Gullfaks 4D seismic study: Petroleum Geoscience, **5**, 213 – 226.

Landrø, M., and J. Stammeijer, 2004, Quantitative estimation of compaction and velocity changes using 4D impedance and traveltime changes: Geophysics, **69**, 949–957.

Liu, Y., D. Draganov, K. Wapenaar, and B. Arntsen, 2016a, Retrieving virtual reflection responses at drill-bit positions using seismic interferometry with drill-bit noise: Geophysical Prospecting, **64**, 348–360.

Liu, Y., J. van der Neut, B. Arntsen, and K. Wapenaar, 2016b, Combination of surface and borehole seismic data for robust target-oriented imaging: Geophysical Journal International, **205**, 758–775.

Lobkis, O. I., and R. L. Weaver, 2001, On the emergence of the Green's function in the correlations of a diffuse field: The Journal of the Acoustical Society of America, **110**, 3011–3017.

Madsen, K. N., S. Dümmong, D. Kritski, A.and Finfer, A. Gillies, and P. Travis, 2013, Simultaneous Multiwell VSP using Distributed Acoustic Sensing: Presented at the Extended Abstract, Second Workshop on Permanent Reservoir Monitoring, EAGE.

Maharramov, M., B. Biondi, and M. Meadows, 2015, Simultaneous TV-regularized time-lapse FWI with application to field data: SEG Technical Program Expanded Abstracts 2015, 1236–1241.

Maharramov, M., B. L. Biondi, and M. A. Meadows, 2016, Time-lapse inverse theory with applications: Geophysics, **81**, R485 – R501.

Malusa, M., F. Poletto, and F. Miranda, 2002, Prediction ahead of the bit by using drill-bit pilot signals and reverse vertical seismic profiling (RVSP): Geophysics, **67**, 1169–1176.

Marchenko, V. A., 1955, Reconstruction of the potential energy from the phases of the scattered waves: Doklady Akademii Nauk SSSR, **104**, 695–698.

Mehta, K., A. Bakulin, J. Sheiman, R. Calvert, and R. Snieder, 2007, Improving the virtual source method by wavefield separation: Geophysics, **72**, V79 – V86.

Mehta, K., J. Sheiman, R. Snieder, and R. Calvert, 2008, Strengthening the virtual-source method for time-lapse monitoring: Geophysics, **73**, S73 – S80.

Meles, G. A., K. Löer, M. Ravasi, A. Curtis, and C. A. da Costa Filho, 2015, Internal multiple prediction and removal using Marchenko autofocusing and seismic interferometry: Geophysics, **80**, A7–A11.

Meles, G. A., K. Wapenaar, and A. Curtis, 2016, Reconstructing the primary reflections in seismic data by Marchenko redatuming and convolutional interferometry: Geophysics, **81**, Q15–Q26.

Menke, W., 1989, Geophysical Data Analysis: Discrete Inverse Theory: Academic Press.

Meunier, J., and F. Huguet, 1998, Cere-la-Ronde; a laboratory for time-lapse seismic monitoring in the Paris Basin: The Leading Edge, **17**, 1388–1394.

Meunier, J., F. Huguet, and P. Meynier, 2001, Reservoir monitoring using permanent sources and vertical receiver antennae: The Cere-la-Ronde case study: The Leading Edge, **20**, 622–629.

Miller, D., J. Haldorsen, and C. Kostov, 1990, Methods for deconvolution of unknown source signatures from unknown waveform data.

Minato, S., T. Matsuoka, T. Tsuji, D. Draganov, J. Hunziker, and K. Wapenaar, 2011, Seismic interferometry using multidimensional deconvolution and crosscorrelation for crosswell seismic reflection data without borehole sources: Geophysics, **76**, SA19 – SA34.

Moon, W., A. Carswell, R. Tang, and D. C., 1986, Radon transform wavefield separation for vertical seismic profiling data: Geophysics, **51**, 940–947.

Muijs, R., K. Holliger, and J. O. A. Robertsson, 2004, Data-driven adaptive decomposition of multicomponent seabed recordings: Geophysics, **69**, 1329–1337.

Muijs, R., J. O. Robertsson, and H. K., 2007, Prestack depth migration of primary and surface-related multiple reflections: Part I - imaging: Geophysics, **72**, S59–S69.

Nakata, N., R. Snieder, T. Tsuji, K. Larner, and T. Matsuoka, 2011, Shear wave imaging from traffic noise using seismic interferometry by cross-coherence: Geophysics, **76**, SA97–SA106.

Panea, I., D. Draganov, C. A. Vidal, and V. Mocanu, 2014, Retrieval of reflections from ambient noise recorded in Mizil area, Romania: Geophysics, **79**, Q31–Q42.

Poletto, F., P. Corubolo, and P. Comelli, 2010, Drill-bit seismic interferometry with and without pilot signals: Geophysical Prospecting, **58**, 257 – 265.

Poletto, F., M. Malusa, F. Miranda, and U. Tinivella, 2004, Seismic while drilling by using dual sensors in drill strings: Geophysics, **69**, 1261–1271.

Poletto, F., and F. Miranda, 2004, Seismic While Drilling: Fundamentals of Drill-Bit Seismic for Exploration: Pergamon. 35.

Poletto, F., F. Miranda, P. Corubolo, A. Schleifer, and P. Comelli, 2014, Drill-bit seismic monitoring while drilling by downhole wired-pipe telemetry: Geophysical Prospecting, **62**, 702–718.

Poletto, F., F. Rocca, and L. Bertelli, 2000, Drill-bit signal separation for RVSP using statistical independence: Geophysics, **65**, 1654 – 1659.

Poliannikov, O., 2011, Retrieving reflections by source-receiver wavefield interferometry: Geophysics, **76**, SA1–SA8.

Poliannikov, O. V., S. Rondenay, and L. Chen, 2012, Interferometric imaging of the underside of a subducting crust: Geophysical Journal International, **189**, 681–690.

Raknes, E. B., and B. Arntsen, 2014, Time-lapse full-waveform inversion of limited-offset seismic data using a local migration regularization: Geophysics, **79**, WA117 – WA128.

Ravasi, M., and A. Vasconcelos, I.and Curtis, 2015, Elastic extended images and velocity-

sensitive objective functions using multiple reflections and transmissions: Geophysical Journal International, **202**, 943–960.

Ravasi, M., I. Vasconcelos, A. Kritski, A. Curtis, C. Filho, Alberto da Costa, and G. A. Meles, 2016, Target-oriented Marchenko imaging of a North Sea field: Geophysical Journal International, **205**, 99–104.

Rector, J., and B. Hardage, 1992, Radiation pattern and seismic waves generated by a working roller-cone drill bit: Geophysics, **57**, 1319 – 1333.

Rector, J., and B. Marion, 1991, The use of drill-bit energy as a downhole seismic source: Geophysics, **56**, 628 – 634.

Rickett, J., L. Duranti, T. Hudson, B. Regel, and N. Hodgson, 2007, 4d time strain and the seismic signature of geomechanical compaction at genesis: The Leading Edge, **26**, 644–647.

Rose, J. H., 2002, 'single-sided' autofocusing of sound in layered materials: Inverse Problems, **18**, 1923.

Røste, T., O. P. Dybvik, and O. K. SÃÿreide, 2015, Overburden 4d time shifts induced by reservoir compaction at snorre field: The Leading Edge, **34**, 1366–1374.

Røste, T., M. Landrø, and P. Hatchell, 2007, Monitoring overburden layer changes and fault movements from time-lapse seismic data on the Valhall field: Geophysical Journal International, **170**, 1100–1118.

Roux, P., K. G. Sabra, P. Gerstoft, W. A. Kuperman, and M. C. Fehler, 2005, P-waves from cross-correlation of seismic noise: Geophysical Research Letters, **32**, L19303.

Ruigrok, E., X. Campman, and K. Wapenaar, 2011, Extraction of p-wave reflections from microseisms: Comptes Rendus Geoscience, **343**, 512 – 525. (Nouveaux dÃČÂl'veloppements de lÃćâĆňâĎćimagerie et du suivi temporel ÃČÂă partir du bruit sismique New developments on imaging and monitoring with seismic noise).

Sabra, K. G., P. Gerstoft, P. Roux, W. A. Kuperman, and M. C. Fehler, 2005a, Extracting time-domain Green's function estimates from ambient seismic noise: Geophysical Research Letters, **32**, L03310.

———, 2005b, Surface wave tomography from microseisms in Southern California: Geophysical Research Letters, **32**, L14311.

Schalkwijk, K. M., C. Wapenaar, and D. J. Verschuur, 2003, Adaptive decomposition of multicomponent ocean-bottom seismic data into downgoing and upgoing P- and S-waves: Geophysics, **68**, 1091–1102.

Schuster, G., J. Yu, J. Sheng, and J. Rickett, 2004, Interferometric/daylight seismic imaging: Geophysical Journal International, **157**, 838 – 852.

Schuster, G. T., 2009, Seismic interferometry: Cambridge University Press.

Seeman, B., and L. Horowicz, 1983, Vertical seismic profiling: Separation of upgoing and downgoing acoustic waves in a stratified medium: Geophysics, **48**, 555–568.

Shapiro, N. M., and M. Campillo, 2004, Emergence of broadband Rayleigh waves from correlations of the ambient seismic noise: Geophysical Research Letters, **31**, L07614.

Shapiro, N. M., M. Campillo, L. Stehly, and M. H. Ritzwoller, 2005, High-resolution surface-wave tomography from ambient seismic noise: Science, **307**, 1615–1618.

Singh, S., R. Snieder, J. Behura, J. van Der Neut, K. Wapenaar, and E. Slob, 2015, Marchenko imaging: Imaging with primaries, internal multiples, and free-surface mul-

tiples: Geophysics, **80**, S165–S174.
Singh, S., R. Snieder, J. van der Neut, J. Thorbecke, E. Slob, and K. Wapenaar, 2017, Accounting for free-surface multiples in Marchenko imaging: Geophysics, **82**, R19–R30.
Slob, E., C. Wapenaar, and J. Thorbecke, 2016, Marchenko equations for acoustic Green's function retrieval and imaging in dissipative media: SEG Technical Program Expanded Abstracts 2016, 5160–5165.
Slob, E., K. Wapenaar, F. Broggini, and R. Snieder, 2014, Seismic reflector imaging using internal multiples with Marchenko-type equations: Geophysics, **79**, S63–S76.
Snieder, R., 2004, Extracting the Green's function from the correlation of coda waves: A derivation based on stationary phase: Physical Review E, **69**, no. 4, 046610.
Snieder, R., M. Miyazawa, E. Slob, I. Vasconcelos, and K. Wapenaar, 2009, A comparison of strategies for seismic interferometry: Surveys in Geophysics, **30**, 503 – 523.
Snieder, R., K. Wapenaar, and K. Larner, 2006, Spurious multiples in seismic interferometry of primaries: Geophysics, **71**, SI111 – SI124.
Stewart, R. R., 1985, Median filtering: Review and a new F/K analogue design: Journal of Canadian Society of Exploration Geophysicists, **21**, 54–63.
Thorbecke, J., and D. Draganov, 2011, Finite-difference modeling experiments for seismic interferometry: Geophysics, **76**, H1–H18.
Thorbecke, J., J. van der Neut, and K. Wapenaar, 2013, Green's function retrieval with Marchenko equations: a sensitivity analysis: SEG Technical Program Expanded Abstracts 2013, 3888–3893.
Thorbecke, J., K. Wapenaar, and G. Swinnen, 2004, Design of one-way wavefield extrapolation operators, using smooth functions in WLSQ optimization: Geophysics, **69**, 1037–1045.
Tonegawa, T., and K. Nishida, 2010, Inter-source body wave propagations derived from seismic interferometry: Geophysical Journal International, **183**, 861–868.
Treitel, S., J. L. Shanks, and C. W. Frazier, 1967, Some aspects of fan filtering: Geophysics, **32**, 789–798.
Ursin, B., 1983, Review of elastic and electromagnetic wave propagation in horizontally layered media: Geophysics, **48**, 1063–1081.
van der Neut, J., D. Alexandrov, and A. Bakulin, 2015a, Shallow virtual source redatuming by multi-dimensional deconvolution: Geophysical Prospecting, **63**, 4–18.
van der Neut, J., J. Thorbecke, K. Mehta, E. Slob, and K. Wapenaar, 2011, Controlled-source interferometric redatuming by crosscorrelation and multidimensional deconvolution in elastic media: Geophysics, **76**, SA63 – SA76.
van der Neut, J., and K. Wapenaar, 2015, Point-spread functions for interferometric imaging: Geophysical Prospecting, **63**, 1033–1049.
———, 2016, Adaptive overburden elimination with the multidimensional marchenko equation: Geophysics, **81**, T265–T284.
van der Neut, J., K. Wapenaar, J. Thorbecke, and E. Slob, 2015b, Practical challenges in adaptive Marchenko imaging: 85th Annual Meeting, SEG, Expanded Abstracts.
Vasconcelos, I., and R. Snieder, 2008a, Interferometry by deconvolution: Part 1 - Theory for acoustic waves and numerical examples: Geophysics, **73**, S115 – S128.

———, 2008b, Interferometry by deconvolution: Part 2 - Theory for elastic waves and application to drill-bit seismic imaging: Geophysics, **73**, S129 – S141.

Verschuur, D. J., A. J. Berkhout, and C. P. A. Wapenaar, 1992, Adaptive surface-related multiple elimination: Geophysics, **57**, 1166–1177.

Wapenaar, C., and A. J. Berkhout, 1989, Elastic wavefield extrapolation: Redatuming of single- and multicomponent seismic data: Elsevier, Amsterdam.

Wapenaar, C. P. A., 1993, Kirchhoff-helmholtz downward extrapolation in a layered medium with curved interfaces: Geophysical Journal International, **115**, 445–455.

Wapenaar, C. P. A., P. Herrmann, D. J. Verschuur, and A. J. Berkhout, 1990, Decomposition of multicomponent seismic data into primary P- and S-wave responses: Geophysical Prospecting, **38**, 633–662.

Wapenaar, K., 2004, Retrieving the elastodynamic Green's function of an arbitrary inhomogeneous medium by cross correlation: Physical Review Letters, **93**, 254301.

Wapenaar, K., F. Broggini, E. Slob, and R. Snieder, 2013, Three-dimensional single-sided Marchenko inverse scattering, data-driven focusing, Green's function retrieval, and their mutual relations: Physical Review Letters, **110**, 084301.

Wapenaar, K., and J. Fokkema, 2006, Green's function representations for seismic interferometry: Geophysics, **71**, SI33 – SI46.

Wapenaar, K., J. Thorbecke, J. van der Neut, F. Broggini, E. Slob, and R. Snieder, 2014, Marchenko imaging: Geophysics, **79**, WA39–WA57.

Wapenaar, K., and J. van der Neut, 2010, A representation for Green's function retrieval by multidimensional deconvolution: The Journal of the Acoustical Society of America, **128**, EL366–EL371.

Wapenaar, K., J. van der Neut, E. Ruigrok, D. Draganov, J. Hunziker, E. Slob, J. Thorbecke, and R. Snieder, 2011, Seismic interferometry by crosscorrelation and by multidimensional deconvolution: a systematic comparison: Geophysical Journal International, **185**, 1335 – 1364.

Wapenaar, K., J. van der Neut, and E. Slob, 2016, Unified double- and single-sided homogeneous Green's function representation: Proceedings of the Royal Society A, **472**, 20160162.

Whitcombe, D. N., P. Paramo, N. Philip, A. Toomey, T. Redshaw, and S. Linn, 2010, The correlated leakage method - its application to better quantify timing shifts on 4D data: Presented at the 72nd EAGE Conference and Exhibition 2010.

Willis, M., R. Lu, X. Campman, M. Nafi Toks´o z, Y. Zhang, and M. Hoop, 2006, A novel application of time-reversed acoustics: salt-dome flank imaging using walkaway VSP surveys: Geophysics, **71**, A7 – A11.

Xu, Z., C. Juhlin, O. Gudmundsson, F. Zhang, C. Yang, A. Kashubin, and S. L´u th, 2012, Reconstruction of subsurface structure from ambient seismic noise: an example from ketzin, germany: Geophysical Journal International, **189**, 1085–1102.

Yang, Y., M. H. Ritzwoller, A. L. Levshin, and N. M. Shapiro, 2007, Ambient noise Rayleigh wave tomography across europe: Geophysical Journal International, **168**, 259–274.

Zadeh, M. H., and M. Landrø, 2011, Monitoring a shallow subsurface gas flow by time lapse refraction analysis: Geophysics, **76**, O35–O43.

Zhan, Z., S. Ni, D. V. Helmberger, and R. W. Clayton, 2010, Retrieval of Moho-reflected shear wave arrivals from ambient seismic noise: Geophysical Journal International, **182**, 408–420.